Applications and integration of optical frequency combs

Thesis by
Boqiang Shen

In Partial Fulfillment of the Requirements for the
Degree of
Doctor of Philosophy

CALIFORNIA INSTITUTE OF TECHNOLOGY
Pasadena, California

2021
Defended May 20th, 2021

Boqiang Shen
ORCID: 0000-0003-0697-508X

ACKNOWLEDGEMENTS

The time I spent at Caltech during my Ph.D. studies was exciting and rewarding. It is a pleasure to have the opportunities to research with so many talented and friendly people. Without their help and support, this thesis would not have been possible.

First and foremost, my sincere appreciation goes to my advisor, Prof. Kerry Vahala, for his continuous encouragement, support, and guidance on research and life over the past six years. More than a scientist and a pioneer in our field, Prof. Vahala is undoubtedly the best mentor that I have ever seen. He has given us a lot of patience and freedom to try our research interests with enormous valuable instructions. The best decision I have ever made was choosing him as my advisor.

I would like to express my gratitude to Prof. Oskar Painter, Prof. Alireza Marandi, Dr. Stephaine Leifer, and Prof. Andrei Faraon for their service as my graduate committee and insightful input on my thesis. I am deeply thankful to Stephanie for being so kind and warmhearted. We had a lot of conversations about the research and life, which made me feel like she was my elder sister. I would also like to thank Prof. John Bowers, Prof. Qiang Lin, Prof. Tobias Kippenberg, and Dr. Scott Diddams for their support during my Ph.D. studies.

I also gratefully acknowledge my colleagues. I would like to offer my special thanks to Dr. Dong Yoon Oh, Dr. Seung Hoon Lee, Dr. Yu-Hung Lai, Dr. Xinbai Li, Dr. Ki Youl Yang, Dr. Qi-Fan Yang, and Dr. Chengying Bao for sharing their helpful advice and ideas as well as productive collaborations. I was greatly enlightened by them. I also acknowledge Dr. Xu Yi and Dr. Myoung-Gyun Suh for their support. I also want to thank Heming Wang, Lue Wu, Zhiquan Yuan, Maodong Gao, Qing-Xin Ji, and Bohan Li. I learned so much from them and enjoyed the conversations and interactions with them. I likewise thank Dr. Mahmood Bagheri and Dr. Gautam Vasisht from JPL, Prof. Rebecca Oppenheimer from AMNH, Dr. Junqiu Liu from EPFL, Dr. Lin Chang, Warren Jin and Chao Xiang from UCSB, and Dr. Yang He and Jingwei Lin from Rochester as well as the staff at Palomar Observatory for fruitful collaborations and exciting moments.

I appreciate the company of my roommate and good friend Yu-An Chen during my Ph.D. journey. We shared the food and space, played the game, and pursued our dream together. My Ph.D. life wouldn't have been enjoyable without meeting him and other friends at Caltech: Baoyi Chen, Yunxuan Li, and Hsiao-Yi Chen.

Last but not least, I thank my parents for their continuous support and love. They let me explore the outside world without any pressure.

ABSTRACT

Optical frequency combs have a wide range of applications in science and technology, including but not limited to timekeeping, optical frequency synthesis, spectroscopy, searching for exoplanets, ranging, and microwave generation. The integration of microresonator with other photonic components enables the high-volume production of wafer-scale optical frequency combs, soliton microcombs. However, it faces two considerable obstacles: optical isolation, which is challenging to integrate on-chip at acceptable performance levels, and power-hungry electronic control circuits, which are required for the generation and stabilization of soliton microcombs. In this thesis, we describe the design and early commissioning of the laser frequency comb for astronomical calibration using electro-optic modulation. We also focus on the realization of a novel and compact chip-scale optical frequency comb, soliton microcomb, including the progress made towards the visible soliton microcomb generation and the demonstration of low power operation of a soliton microcomb along contours of constant power in the phase space. We introduce a soliton spectrometer using dual-locked counter-propagating soliton microcombs to provide high-resolution frequency measurement. Finally, we look into the integration of lasers and high-Q microresonators. The self-injection locking process has been shown to create a new turnkey soliton operating point that eliminates difficult-to-integrate optical isolation as well as complex startup and feedback loops. Moreover, this technique also simplifies the access to high-efficiency dark soliton states without special dispersion engineering of microresonators.

PUBLISHED CONTENT AND CONTRIBUTIONS

[1] Chengying Bao, Boqiang Shen, Myoung-Gyun Suh, Heming Wang, Kemal Şafak, Anan Dai, Andrey B Matsko, Franz X Kärtner, and Kerry Vahala. Oscillatory motion of a counterpropagating Kerr soliton dimer. *Phys. Rev. A*, 103(1):L011501, 2021.
B. S. participated in the experiment and the writing of the manuscript.

[2] Chengying Bao, Myoung-Gyun Suh, Boqiang Shen, Kemal Şafak, Anan Dai, Heming Wang, Lue Wu, Zhiquan Yuan, Qi-Fan Yang, Andrey B Matsko, et al. Quantum diffusion of microcavity solitons. *Nat. Phys.*, 2021.
B. S. participated in the experiment and the writing of the manuscript.

[3] Chengying Bao*, Zhiquan Yuan*, Heming Wang, Lue Wu, Boqiang Shen, Keeyoon Sung, Stephanie Leifer, Qiang Lin, and Kerry Vahala. Interleaved difference-frequency generation for microcomb spectral densification in the mid-infrared. *Optica*, 7(4):309–315, 2020.
B. S. participated in the experiment and the writing of the manuscript.

[4] Lin Chang*, Weiqiang Xie*, Haowen Shu*, Qi-Fan Yang, Boqiang Shen, Andreas Boes, Jon D Peters, Warren Jin, Chao Xiang, Songtao Liu, et al. Ultra-efficient frequency comb generation in AlGaAs-on-insulator microresonators. *Nat. Commun.*, 11(1331), 2020.
B. S. participated in the writing of the manuscript.

[5] Yang He*, Qi-Fan Yang*, Jingwei Ling, Rui Luo, Hanxiao Liang, Mingxiao Li, Boqiang Shen, Heming Wang, Kerry Vahala, and Qiang Lin. Self-starting bi-chromatic $LiNbO_3$ soliton microcomb. *Optica*, 6(9):1138–1144, 2019.
B. S. participated in the $LiNbO_3$ soliton microcomb generation and prepared the data.

[6] Warren Jin*, Qi-Fan Yang*, Lin Chang*, Boqiang Shen*, Heming Wang*, Mark A Leal, Lue Wu, Maodong Gao, Avi Feshali, Mario Paniccia, et al. Hertz-linewidth semiconductor lasers using CMOS-ready ultra-high-Q microresonators. *Nat. Photon.*, 2021.
B. S. conducted the photonic alignment and the linewidth measurement, analyzed the data, and participated in the writing of the manuscript.

[7] Yu-Hung Lai*, Myoung-Gyun Suh*, Yu-Kun Lu, Boqiang Shen, Qi-Fan Yang, Heming Wang, Jiang Li, Seung Hoon Lee, Ki Youl Yang, and Kerry Vahala. Earth rotation measured by a chip-scale ring laser gyroscope. *Nature Photonics*, 14(6):345–349, 2020.
B. S. participated in the experiment and the writing of the manuscript.

[8] Seung Hoon Lee*, Dong Yoon Oh*, Qi-Fan Yang*, Boqiang Shen*, Heming Wang*, Ki Youl Yang, Yu-Hung Lai, Xu Yi, Xinbai Li, and Kerry Vahala.

Towards visible soliton microcomb generation. *Nat. Commun.*, 8(1295), 2017.
B. S. participated in the experiment of soliton microcomb generation at 780 nm and prepared the data.

[9] Xinbai Li*, Boqiang Shen*, Heming Wang*, Ki Youl Yang*, Xu Yi, Qi-Fan Yang, Zhiping Zhou, and Kerry Vahala. Universal isocontours for dissipative kerr solitons. *Opt. Lett.*, 43(11):2567–2570, 2018.
B. S. participated in the experiment and the numerical simulation, prepared the data, and participated in the writing of the manuscript.

[10] Zachary L Newman, Vincent Maurice, Tara Drake, Jordan R Stone, Travis C Briles, Daryl T Spencer, Connor Fredrick, Qing Li, Daron Westly, Bojan R Ilic, et al. Architecture for the photonic integration of an optical atomic clock. *Optica*, 6(5):680–685, 2019.
B. S. participated in the experiment and demonstrated the 10GHz soliton microcombs.

[11] Boqiang Shen*, Lin Chang*, Junqiu Liu*, Heming Wang*, Qi-Fan Yang*, Chao Xiang, Rui Ning Wang, Jijun He, Tianyi Liu, Weiqiang Xie, et al. Integrated turnkey soliton microcombs. *Nature*, 582(7812):365–369, 2020.
B. S. conceived the project, packaged the chip, conducted the experiment, prepared the data, and managed the draft of the manuscript.

[12] Heming Wang, Yu-Kun Lu, Lue Wu, Dong Yoon Oh, Boqiang Shen, Seung Hoon Lee, and Kerry Vahala. Dirac solitons in optical microresonators. *Light Sci. Appl.*, 9(205), 2020.
B. S. prepared the data and participated in the writing of the manuscript.

[13] Lue Wu*, Heming Wang*, Qifan Yang, Qing-Xin Ji, Boqiang Shen, Chengying Bao, Maodong Gao, and Kerry Vahala. Greater than one billion Q factor for on-chip microresonators. *Opt. Lett.*, 45(18):5129–5131, 2020.
B. S. participated in the experiment and prepared the data.

[14] Ki Youl Yang*, Dong Yoon Oh*, Seung Hoon Lee*, Qi-Fan Yang, Xu Yi, Boqiang Shen, Heming Wang, and Kerry Vahala. Bridging ultrahigh-Q devices and photonic circuits. *Nat. Photon.*, 12(5):297–302, 2018.
B. S. participated in the experiment and the simulation, prepared the data, and participated in the writing of the manuscript.

[15] Qi-Fan Yang*, Qing-Xin Ji*, Lue Wu*, Boqiang Shen, Heming Wang, Chengying Bao, Zhiquan Yuan, and Kerry Vahala. Dispersive-wave induced noise limits in miniature soliton microwave sources. *Nat. Commun.*, 12(1442), 2021.
B. S. participated in the experiment and the numerical simulation, and prepared the data.

[16] Qi-Fan Yang*, Boqiang Shen*, Heming Wang*, Minh Tran, Zhewei Zhang, Ki Youl Yang, Lue Wu, Chengying Bao, John Bowers, Amnon Yariv, et al.

Vernier spectrometer using counterpropagating soliton microcombs. *Science*, 363(6430):965–968, 2019.

B. S. conducted the experiment of counterpropagating soliton microcomb generation and the measurements of laser frequencies, prepared the data, and participated in the writing of the manuscript.

*These authors contributed equally to this work.

TABLE OF CONTENTS

LIST OF ILLUSTRATIONS

Number *Page*

Chapter 1

INTRODUCTION

1.1 Optical frequency combs

The optical frequency comb [1, 2] is a collection of phase-locked, coherent laser lines featuring equally spaced frequencies. These frequencies are given by the expression:

$$f_n = n f_r + f_0 \tag{1.1}$$

where, f_r is the repetition rate of the comb, which is the frequency difference between two adjacent comb lines, whereas f_0 is an offset frequency that is common to all the lines.

Optical frequency combs have a wide range of applications in science and technology, including but not limited to, time keeping [3, 4], optical frequency synthesis [5–9], spectroscopy [8, 10–14], ranging [15–18], astronomical calibration [19–25], and microwave generation [26–31].

There are a few methods for optical frequency comb generation. An easy approach to the formation of an optical frequency comb employs a few cascaded electro-optical (EO) modulators driven by a microwave signal to impose a series of sidebands on a continuous-wave laser. Due to the recent advances in integrated lithium niobate waveguides, the EO comb uses off-the-shelf components from the telecommunication industry and therefore has great reliability.

Another approach to optical frequency combs generation has attracted great interest due to its advantages of a small footprint, low power consumption, and integration capability. It offers the possibility of miniature comb systems integrated on a semiconductor chip. They are often called microcombs which rely on the Kerr nonlinearity that is enhanced by the optical power build-up in high-Q microresonators or ring-like resonators. Benefited from modern fabrication techniques, the ultra-low propagation loss inside the microresonators results in the quality (Q) factors ranging from 10^6 up to nearly 10^{11}. The milliwatt levels input power can be enhanced to as high as kilowatts in such high-Q resonators, and the Kerr nonlinearity spontaneously generates two sidebands through parametric oscillation [32, 33] and more cascaded sidebands through four-wave mixing process [32]. It was shown to lead to a frequency comb in 2007 [34]. Developments related to solitons in optical fiber

cavities [35, 36] combined with a better understanding of combs in microresonators eventually led to operational modes where solitons could be generated [37–41]. In the time domain, a soliton is a nonlinear pulse that propagates inside a fiber cavity or a microresonator. The pulse maintains its shape by balancing the anomalous dispersion with its Kerr nonlinearity. The external pump compensates for the propagating loss, and the pulse can go around the cavity indefinitely. When coupled out from the cavity, pulses from different round trips form a periodic pulse train and become a frequency comb called a soliton microcomb. Soliton microcombs have been demonstrated in many materials such as magnesium fluoride [37], diamond [42], silicon nitride [39, 40, 43–45], silica [38, 46], aluminum nitride [47], and recently, lithium niobate [48], and III-V semiconductors [49]. By modern lithographic control technique, the geometric dispersion engineering also enables the operation of octave-spanning combs of THz-repetition rate [44, 45] and towards visible band combs [50, 51].

1.2 Thesis outline

In this thesis, we focus on the applications of the optical frequency combs, including usage of the electro-optic combs on the search of exoplanets (Chapter 3) and the impact of the soliton microcombs on spectroscopic applications (Chapter 6). We also demonstrated soliton microcombs towards visible band (Chapter 4) and low power operation of microcomb along the iso-contours for dissipative Kerr soliton systems (Chapter 5). At last, we look into the possibility of fully integrated chip-based soliton microcombs. The self-injection locking process has been shown to create a new turnkey operating point that eliminates complex startup and feedback loops (Chapter 7). Moreover, this technique simplifies access to dark soliton states as well (Chapter 8).

The thesis is organized as follows:

Chapter 2 introduces the background of the electro-optic frequency comb. The reliable and easy-to-operate electro-optic comb is a powerful wavelength calibration tool for precision radial velocity (PRV) measurement used in chapter 3.

Chapter 3 describes the design and early commissioning of the laser frequency comb (LFC) for astronomy. Detailed setups of the electric-optic frequency comb and the spectral flattener are discussed. The user interfaces further facilitate the data acquisition during the Radial Velocity (RV) observation on the sky in search of exoplanets.

Chapter 4 focuses on the progress made towards the visible soliton microcomb generation. A simple method of engineering the dispersion of the cavity is used to broaden the window of available pump wavelengths for bright soliton generation. 20 GHz soliton microcombs are generated using the pump at 1 μm and 778 nm. The shortest wavelength soliton-to-date is demonstrated covering the 755-790 nm band.

Chapter 5 investigates contours of constant power and constant pulse width for dissipative Kerr solitons. Measurements were shown to be in good agreement with the Lugiato-Lefever equation numerical model augmented by Raman interactions, as well as the prediction of closed-form expressions with Raman interaction. Stable soliton operation for pump powers as low as 10.8 mW was also demonstrated in the course of this work.

Chapter 6 introduces soliton spectrometer using dual-locked counter-propagating soliton microcombs to provide high-resolution frequency measurements of rapid continuously and step tuned lasers as well as complex multi-line spectra. In combination with a tunable laser, the spectrometer also enables precise measurement of absorption spectra including random spectral access (as opposed to only continuous spectral scanning).

Chapter 7 demonstrates an integrated electronics-rate soliton microcomb in a butterfly package. The unisolated laser-microresonator system creates a new turnkey soliton operating point, which eliminates the optical isolator, as well as the electronic control circuit. Given these compelling features combined with its compact footprint, the application of this method represents a milestone of integration and high-volume production of optical frequency combs. Due to the simplification of the soliton microcomb system, this approach could be applied in other integrated high-Q microresonator platforms to attain soliton microcombs across a wide range of applications.

Chapter 8 presents a new regime of Kerr comb operation in normal dispersion microresonators supported by ultra-low-loss silicon nitride waveguides, fabricated in a high-volume complementary metal-oxide-semiconductor (CMOS) foundry. By self-injection locking a conventional semiconductor distributed-feedback (DFB) laser to these ultra-high-Q microresonators, we reduce noise by five orders of magnitude, yielding a previously unattainable frequency level for integrated lasers. Within the same configuration, the dark soliton microcomb both operates turnkey and attains coherent comb operation under conditions of normal dispersion without any special dispersion engineering.

Chapter 2

ELECTRO-OPTIC FREQUENCY COMBS

2.1 Introduction

In this chapter, we will first introduce a versatile type of optical frequency comb: electro-optics (EO) frequency comb [52–56]. It employs a few cascaded EO modulators driven by a single microwave signal to create a grid of sidebands on a continuous-wave laser. This results in a spectrally flat optical frequency comb that can be further compressed into a shorter pulse by additional nonlinear spectral broadening. Compared to the conventional mode-lock laser comb and microresonator-based frequency comb, the EO frequency comb features a simple structure, deterministic nature, and thus great reliability. The EO frequency comb described in this chapter will be used in the field for wavelength calibration in search of the exoplanets.

2.2 Schematic of the electro-optic frequency comb

The schematic layout for a typical electro-optic frequency comb is illustrated in Fig. 2.1. The continuous-wave (CW) laser is coupled into cascaded lithium niobate ($LiNbO_3$) phase modulators (PMs), and then an amplitude modulator (AM), also known as an intensity modulator (IM). The optical field after the modulators can be described as:

$$E(t) = AE_0 e^{-i2\pi f_0 t} \times e^{i\sum_k \beta_{\mathrm{PM},k} \sin(2\pi f_m t + \varphi_k)} \times [e^{i\varphi_{\mathrm{DC}}} + e^{i\beta_{\mathrm{AM}} \sin(2\pi f_m t + \varphi_{\mathrm{AM}})}] \quad (2.1)$$

where A is the attenuation factor to account for the insertion loss of modulators. $\beta_{\mathrm{PM},k}$, φ_k are the modulation depth and relative phase of the k-th phase modulator. β_{AM}, φ_{AM}, φ_{DC} are the modulation depth, relative phase, and the direct current (DC) bias phase of the amplitude modulator.

We can expand the phase modulation term using the Jacobi–Anger identity:

$$e^{i\beta \sin\varphi} = \sum_{n=-\infty}^{\infty} J_n(\beta) e^{in\varphi} \quad (2.2)$$

where J_n is the n-th order Bessel function of the first kind. Therefore, the field after phase modulation can be seen as a collection of laser lines with equally spaced

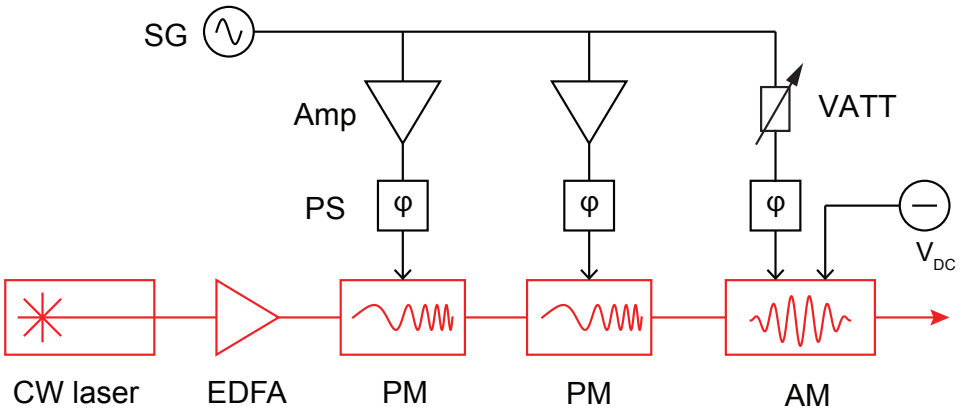

Figure 2.1: **Schematic of a typical electro-optic frequency comb.** SG: analog radio-frequency signal generator. Amp: electrical amplifier. PS: electrical phase shifter. VATT: variable microwave attenuator. V_{DC}: direct-current voltage source. CW laser: continuous-wave (CW) laser. EDFA: erbium-doped fiber amplifier. PM: phase modulator. AM: amplitude modulator.

sidebands at the modulation frequency f_m ($f_n = f_0 + nf_m$) and the number of comb lines is roughly twice the modulation depth $\beta_{\mathrm{PM},k}$ according to the numerical simulation.

The pump laser frequency f_0 can be stabilized to a molecular or atomic reference, e.g. $f_0 = f_{atom}$, to provide an anchor for the optical frequency. The phase/amplitude modulators are driven by an amplified radio-frequency (RF) signal. The RF modulation frequency f_m can be tuned from MHz to tens of GHz and can be synchronized with a compact Rb clock which is GPS-disciplined to provide sub-Hertz accuracy.

To maximize the number of sidebands, the phase of PMs should be synchronized via RF phase shifters ($\varphi_k = 0$, for any k) and therefore the number of comb lines are determined by the sum of independent PMs, which is approximately $\sum_k 2\beta_{\mathrm{PM},k}$.

By setting the modulation phase φ_{AM} to 0, the modulation depth β_{AM} to π, and the bias phase φ_{DC} to 0 or π, a linear chirp of modulation sidebands can be achieved by time gating of the intensity modulator [57]. The intensity modulator also improves the flatness of the EO comb [58] because some of the comb lines generated solely by PMs can have lower intensities due to the zeros of Bessel functions. In the experiment, the modulation phase can be tuned by phase shifter: the optical spectrum of EO comb will be symmetric with respect to the pump laser line when $\varphi_{\mathrm{AM}} = 0$ or $\varphi_{\mathrm{AM}} = \pi$. By measuring the average optical output power before and after the

modulation, the bias phase φ_{DC} and modulation depth β_{AM} can also be set by the bias voltage and the variable microwave attenuator, respectively.

2.3 Dispersion compensation and pulse shaping

Any dispersive components can be used to compensate for the linear chirp of modulation sidebands. Usually, line-by-line waveshaping is convenient for compensating arbitrary dispersion from electro-optic combs with different configurations, such as repetition rate, pump laser frequency, and fiber loop length. Single-mode fibers or dispersion compensation Bragg grating can also be used if the resulted linear chirp of EO comb lines is fixed. After dispersion compensation, the phase of electro-optic comb teeth will be flattened and the comb will form a temporal pulse, which can be verified by autocorrelation measurement. In Fig.2.2, the autocorrelation of an EO comb pulse with around 1.6 ps temporal width is measured.

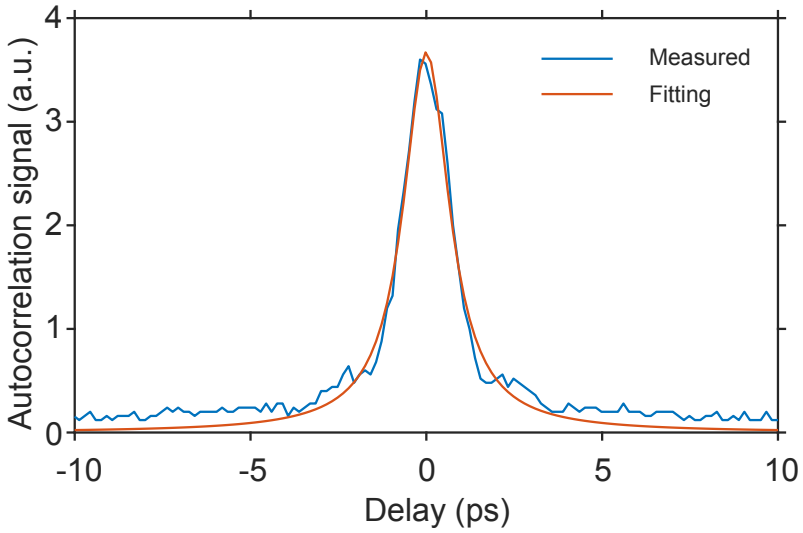

Figure 2.2: **Autocorrelation measurement of the typical electric-optic (EO) comb pulse after dispersion compensation.** The red line is the linewidth fit to the autocorrelation measurement data (blue) yielding pulse width about 1.6 ps. Two commercial phase modulators were used for EO modulation.

If we amplify the pulse first by the optical amplifier and then send it through a highly nonlinear fiber (HNLF) or a nonlinear waveguide with specially designed dispersion, the self-phase modulation of optical pulses will continue to narrow down its temporal pulse width. In the frequency domain, the new comb lines will

be created via the four-wave mixing process. After further line-by-line attenuation, the relatively broad and flat electro-optic comb is a powerful wavelength calibration tool for precision radial velocity (RV) measurement which we will discuss in the next chapter.

Chapter 3

SEARCHING FOR EXOPLANETS USING AN ELECTRO-OPTIC FREQUENCY COMB IN THE PALOMAR RADIAL VELOCITY INSTRUMENT (PARVI)

3.1 Introduction

[1]The periodic Doppler shifts in the stellar spectrum of the host star can be measured to infer the presence of an orbiting exoplanet. Planet detection via the Doppler shifts or Precision Radial Velocity (PRV) technique resulted in the first detection in 1995 of a planet orbiting a mature solar star, 51 Pegasi [59], and was recognized with the 2019 Nobel Prize in Physics. Since that initial discovery, over 800 planets have been found using this technique.

The measurement relies on a highly stable and precisely calibrated spectrometer. Almost all of the calibrations are provided by some combination of arc lamps, etalons, I_2 gas cells, or laser frequency combs. These instruments have detected planets with a broad range of masses and orbital separations with a floor of PRV precision around 1 m s^{-1}, although a new suite of instruments, including ESPRESSO [60], EXPRES [61], and NEID [62] promises to break this barrier. A recent National Academy study has described the need to make Extreme Precision Radial Velocity observations (EPRV) to measure the Doppler reflex motion of an Earth-mass planet in a one-year orbit around a solar-type star, 9 cm s^{-1}.

The laser frequency comb (LFC) generated by electro-optic modulation (EOM) offers an extremely stable wavelength calibration at the few cm s^{-1} RV level [63]. In this chapter, we describe the design and early commissioning of the LFC with great potential at infrared wavelengths. Compared to commercial visible band Menlo astrocombs, as most of the stars in our galaxy are M-dwarf stars which are smaller and cooler and primarily emit light in the near-infrared, NIR astrocombs produce larger RV signals. And they also provide RV measurement capability in the spectral range where there are less stellar jitters than the signals in the visible band.

The implementation of the spectrometer, which is precisely calibrated by the LFC,

[1]Work presented in this chapter remains a work in progress. The LFC system is assembled, installed, and tested at Palomar Observatory by Boqiang Shen and Stephanie Leifer. The flattener was first assembled by a team at CalStateLA, and was then reconfigured by Mahmood Bagheri, Stephanie Leifer, and Boqiang Shen. Boqiang Shen is the copyright owner of the LFC control software.

together with the advanced Adaptive Optics (AO) system for the 5 m Hale Telescope on Palomar Mountain is called the Palomar Radial Velocity Instrument (PARVI).

3.2 Laser frequency comb design and setup

The laser frequency comb design in PARVI is similar to the design described in Metcalf et al. [22], Obrzud et al. [64], and Yi et al. [20]. The proof of concept has been demonstrated at the NASA Infrared Telescope Facility (IRTF) and the W. M. Keck observatory 10 m telescope. Three EOM combs are operating at observatories for PRV spectrograph wavelength calibration besides this, including the one at the Hobby Eberly Telescope's Habitable Planet Finder (HPF) [65], and the one in Subaru Observatory's Infrared Doppler Instrument (IRD) [21].

The detailed experimental setup of the PARVI comb is provided in Fig. 3.1. The pump laser is stabilized to an HCN absorption feature at 1559.914 nm. Three cascaded phase modulators and one amplitude modulator are driven by a single 10 GHz ultra-low noise phase noise microwave generator which is locked to a GPS-referenced rubidium clock. We recycle and amplify the RF power from the external termination ports of the first two PMs and synchronize all the modulators via phase shifters. Variable microwave attenuators are used to optimize the input RF power of the RF amplifier and the modulation depth of the amplitude modulator. The remaining microwave power of the third PM is sent to a frequency counter for monitoring and diagnosis purpose. The amplified pump light goes through these modulators, becomes a 10 nm wide seed comb, and is then intensity stabilized to the optimal operating point by a servo box that provides the DC bias and compensates for the charging and drifting in the sytem. The seed comb is then sent through a Waveshaper (Finisar model 1000A) to remove the linear chirp, amplified by the high-power optical amplifier (Pritel), and broadened by a specially designed HNLF spliced by NIST. The nonlinear fiber package consists of three segments: 5 m of normal dispersion HNLF, 60 cm of single-mode fiber, and 2 m of anomalous dispersion HNLF. The high-intensity pump lines of the broadened comb are attenuated down by a bandpass filter. After the dynamic spectral flattener, the broadened comb lines are capped at a certain intensity level and formed a flat-top spectral envelope. The flat and broad comb is then combined with the pump line and injected into the PARVI spectrograph for wavelength calibration.

The laser frequency comb assembly is comprised entirely of polarization-maintaining (PM) parts except for the single-mode fiber segment in the HNLF package. The

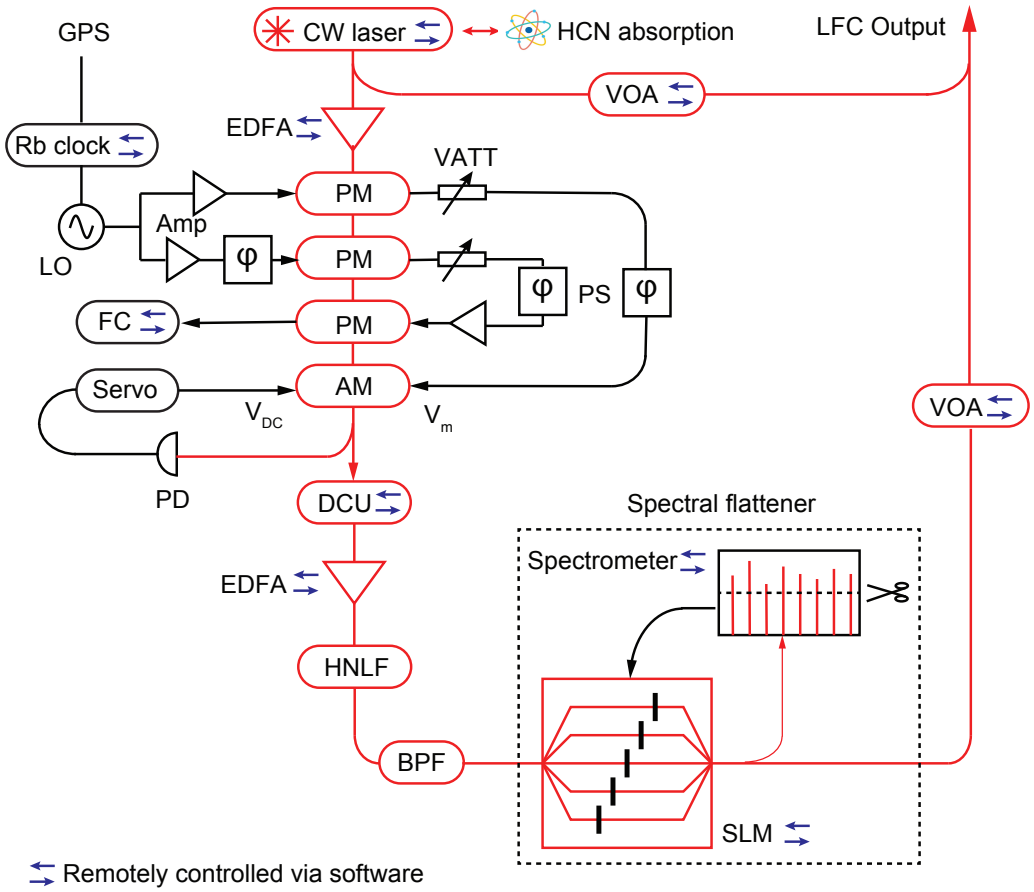

Figure 3.1: **Detailed setup of the laser frequency comb for PARVI.** Bidirectional arrow marks the unit that is being remotely operated or monitored. Rb clock: rubidium clock. LO: low phase noise microwave local oscillator. Amp: microwave amplifier. FC: frequency counter. PS: microwave phase shifter. EDFA: erbium-doped fiber amplifier. VATT: variable microwave attenuator. VOA: variable optical attenuator. CW laser: line-referenced continuous-wave laser. PM: phase modulator. AM: amplitude modulator. PD: photodetector. V_{DC}: direct-current voltage port. V_m: microwave modulation port. DCU: dispersion compensation unit. HNLF: highly nonlinear fiber. BPF: bandpass filter. SLM: spatial light modulator.

comb generator assembly, together with the control rack-mount computer, is contained in a temperature-controlled steel instrument rack. The temperature can be well controlled within 0.1 °C by the thermal control system, while the facility environmental temperature can vary between -5 °C to 25 °C seasonally. The frequency stability of the LFC is dominated by the reference laser stability, which has been characterized by Gabe Ycas at NIST and reported in Yi et al. [20].

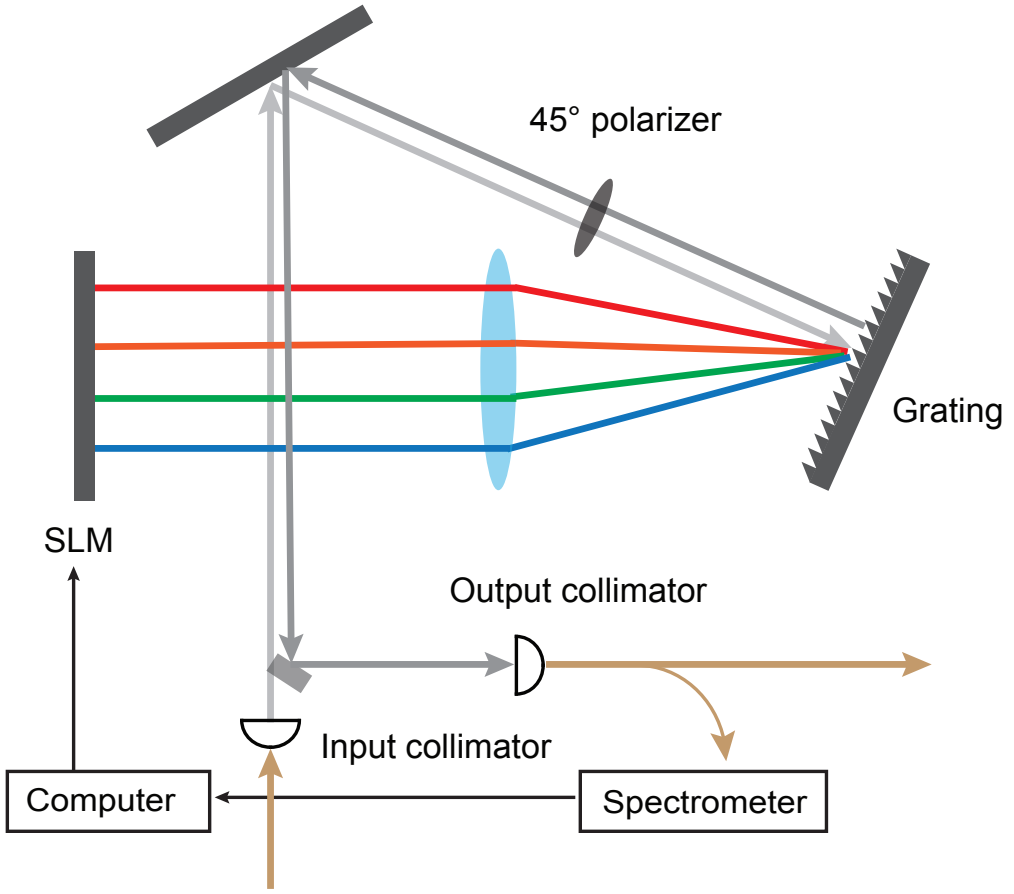

Figure 3.2: **Detailed setup of the spectral flattener.** The spectral transmission is controlled by adjusting the voltage on the liquid crystal display (LCD) pixels of the SLM, altering the polarization reflected by the grating. SLM: spatial light modulator

3.3 Spectral flattener design and setup

The spectral flattener design is similar to the design described by Probst et al. [66]. It is primarily a free-space setup and housed in a thermally controlled enclosure on the optical bench next to the comb instrument rack. The key part of the flattener is a reflective spatial light modulator (SLM) from Meadowlark Optics. The broadened optical frequency comb after the HNLF package is sent into free space by a fiber optic collimator and passed through a 45°polarizer. The polarized light hits the grating where it gets spectrally dispersed and then is projected onto the SLM via the lens. 1920×1152 liquid crystal pixels on the SLM have been grouped into 480 channels which covers the entire wavelength range that is of our interest, with a resolution of 1.6 nm per channel. Each channel can apply voltages independently

to piece-wise adjust the phase difference between the electric field components on two optical axes of the liquid crystal pixels and thus change the polarization of the return light. The light is then recombined at the grating and passed the polarizer again, resulting in wavelength-dependent attenuation levels. The attenuated light is then collected by a fiber collimator and part of the signal is sent to a spectrometer for feedback.

Before using the flattener, two calibration steps are required for proper performance: The voltage response of SLM was calibrated by measuring the transmission when equal voltages are applied on the SLM pixels. The relation between the channel number and the corresponding wavelength is calibrated by setting the SLM as a bandpass filter on each channel.

Based on the difference between the current comb intensity readouts on the spectrometer and the desired intensity level, the control software calculates the voltage increments or decrements on each channel to achieve the corresponding attenuation. The steady-state is reached after a few iterations and a flat-top spectrum can be obtained. Note that, in our design, only one polarizer is used. The attenuation level at each channel is dynamic via the feedback loop instead of a static configuration.

By truncating the spectrum at around 20dB below its maximum, the LFC provides uniform illumination on the PARVI spectrometer, see Fig. 3.3.

3.4 PARVI LFC operation and interfaces

The entire laser frequency comb system can be remotely monitored and controlled using a National Instruments (NI) LabView graphical user interface (GUI), see Fig. 3.4.

There are two buttons on the GUI to switch the comb operating mode between "on", "idle", and "off". When the comb is not being used for observations, the high-power EDFA that amplifies the seed comb is turned off. The LFC usually switches between "on" and "idle" mode, where the mini comb is running continuously. The full system, including the power supplies of microwave amplifiers and oscillator, EDFA, and pump laser, can also be turned off in orders when a complete shutdown is required.

The GUI also displays the attenuation controls for both the comb and pump overlay. The amount of attenuation applied to the comb spectrum that is injected into the PARVI spectrograph can be controlled by the user to match the intensity of the target star under observation. The 1559.914 pump line can also be superimposed

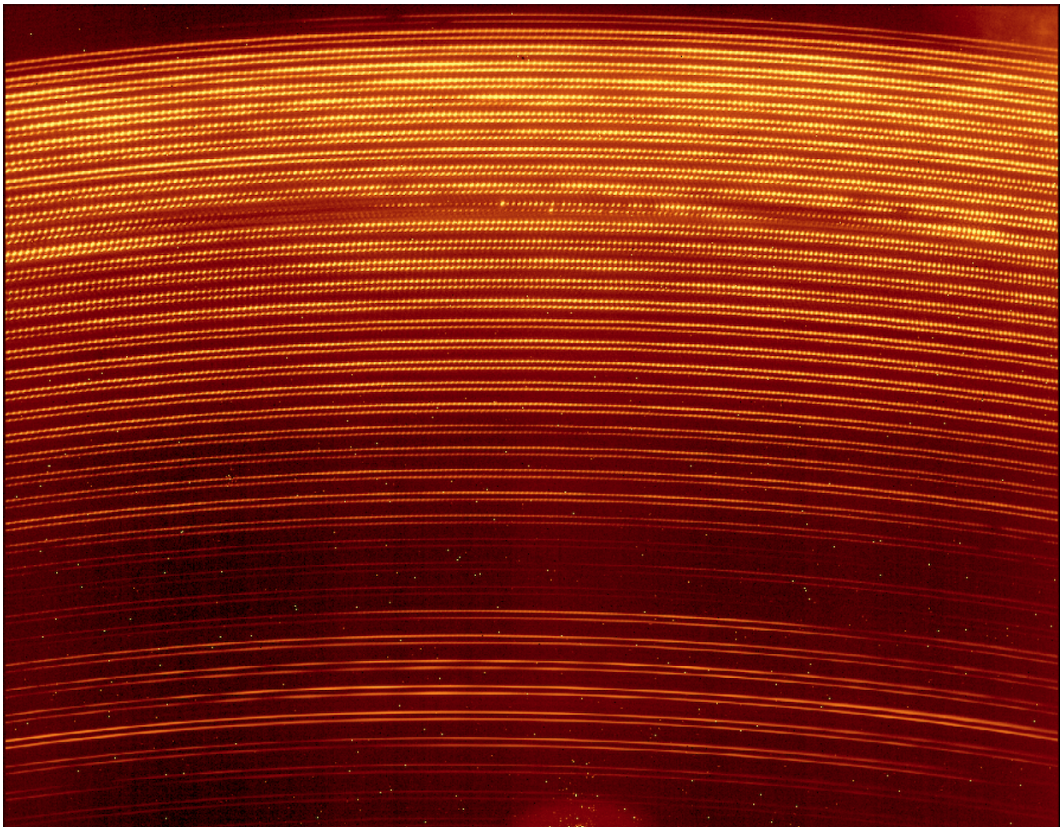

Figure 3.3: **False color image of the laser frequency comb on the PARVI spectrometer.** The broad and flat comb lines cover a range from 1350 nm to 1750nm, with a continuum dispersive wave peaked at 1250nm. Two input fiber channels of the spectrometer are illuminated by the LFC.

on the spectrum with an independent attenuation control and serves as a wavelength marker and indicate the location of the line-referenced pump frequency on the PARVI spectrograph. The spectrum data from the spectrometer in the dynamic spectral flattener is displayed at the center of the GUI. It also provides an option for dynamic flattening which adjusts the voltages applied to each channel on the SLM at a frequency set by the user. The routines of the look-up table (LUT) generation and wavelength-to-pixel calibration for SLM are also built into the interface. It also displays the status of whether the rubidium clock is locked to a GPS signal at the observatory, whether the laser is locked to the gas cell, and the measured repetition rate of the frequency comb by the frequency counter. Temperature is monitored and reported in three locations within the comb instrument rack as well as in the spectral flattener enclosure. In addition, the dispersion compensation of Waveshaper and EDFA pump current settings can also be set in the advanced setting section.

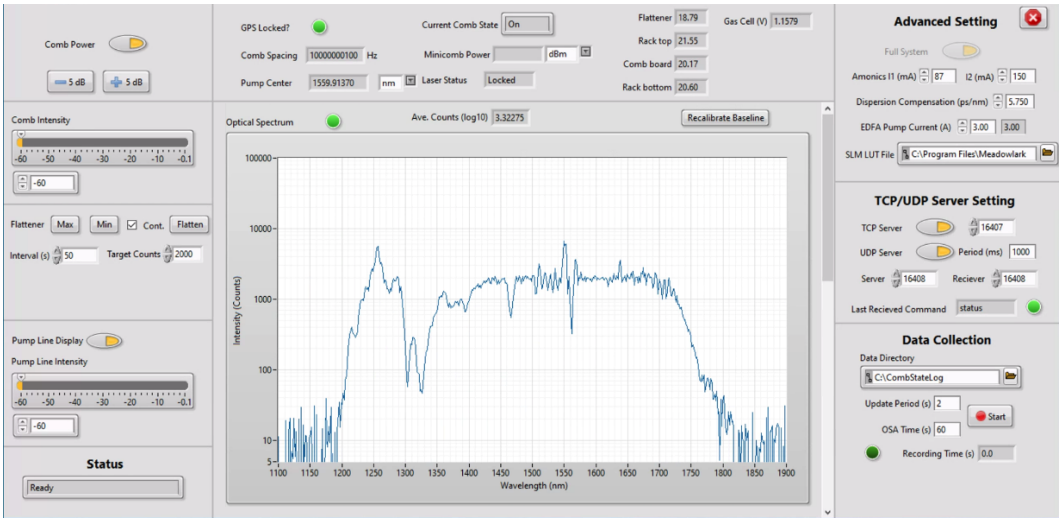

Figure 3.4: **Screenshot of the graphic user interface of the laser frequency comb.**

Moreover, the GUI features the User Datagram Protocol (UDP) server which continuously broadcasts all the status information of the LFC with timestamps in JavaScript Object Notation (JSON) strings on the local network, and the Internet protocol suite (TCP/IP) server which listens and accepts the commands from clients to change the LFC state without logging into the computer. Therefore, the LFC system could be integrated into the PARVI data acquisition pipeline.

3.5 Summary

The Palomar Radial Velocity Instrument (PARVI) remains a work in progress, its final integration and testing are postponed due to the COVID-related closure of Palomar Observatory where the instrument is located.

Future upgrades of the laser frequency comb will incorporate a filter cavity to further reduce the phase noise of comb lines away from the pump and the use of a self-referenced pump laser to reference the offset frequency. The current HNLF is also going to be replaced by a PM HNLF package or a packaged nonlinear waveguide with a better spectral broadening design. With the LFC fully operational, we will provide a calibration source with improved frequency stability. The LFC works with a compact, diffraction-limited, single-mode fiber-fed spectrometer for a wide range of exoplanet searching and other projects requiring extreme absolute frequency stability.

A PARVI-like instrument operating across near-IR and into the visible, from 350 nm to 2400 nm, could revolutionize EPRV observations of exoplanets on a space

platform where small weight and volume are critical. The generation of a visible band optical frequency comb and the integration of an optical frequency comb is on demand. In the following chapters, we will focus on another type of optical frequency combs called soliton microcombs, which are based on the nonlinearity inside ultra-high-Q microresonators.

Chapter 4

TOWARDS VISIBLE SOLITON FREQUENCY COMBS

[1]Frequency combs have applications that extend from the ultra-violet into the mid-infrared bands. Microcombs, a miniature and often semiconductor-chip-based device, can potentially access most of these applications, but are currently more limited in spectral reach. Here, we demonstrate mode-locked silica microcombs with emission near the edge of the visible spectrum. By using both geometrical and mode-hybridization dispersion control, devices are engineered for soliton generation while also maintaining optical Q factors as high as 80 million. Electronics-bandwidth-compatible (20 GHz) soliton mode locking is achieved with low pumping powers (parametric oscillation threshold powers as low as 5.4 mW). These are the shortest wavelength soliton microcombs demonstrated to date and could be used in miniature optical clocks. The results should also extend to visible and potentially ultra-violet bands.

4.1 Introduction

Soliton mode locking [37–40, 43] in frequency microcombs [67] provides a pathway to miniaturize many conventional comb applications. It has also opened investigations into new nonlinear physics associated with dissipative Kerr solitons [37] and Stokes solitons [68]. In contrast to early microcombs [67], soliton microcombs eliminate instabilities, provide stable (low-phase-noise) mode locking, and feature a highly reproducible spectral envelope. Many applications of these devices are being studied, including chip-based optical frequency synthesis [9], secondary time standards [4], and dual-comb spectroscopy [11, 12]. Also, a range of operating wavelengths is opening up by use of several low-optical-loss dielectric materials for resonator fabrication. In the near-infrared (IR), microcombs based on magnesium fluoride [37], silica [38, 46], and silicon nitride [39, 40, 43–45] are being studied for frequency metrology and frequency synthesis. In the mid-IR spectral region, silicon nitride [69], crystalline [70], and silicon-based [71] Kerr microcombs as well as quantum-cascade microcombs [72] are being studied for application to molecular fingerprinting.

[1]Work presented in this chapter has been published in [50] "Towards visible soliton microcomb generation", *Nature Communications* 8, 1295 (2017). The 780nm soliton microcomb was demonstrated by Dongyoon Oh and Boqiang Shen.

At shorter wavelengths below 1 μm, microcomb technology would benefit optical atomic clock technology [73], particularly efforts to miniaturize these clocks. For example, microcomb optical clocks based on the D 1 transition (795 nm) and the two-photon clock transition (798 nm) in rubidium have been proposed [4]. Also, a microcomb clock using two-point locking to rubidium D 1 and D 2 lines has been demonstrated by frequency doubling from the near-IR. More generally, microcomb sources in the visible and ultra-violet bands could provide a miniature alternative to larger mode-locked systems such as titanium sapphire lasers in cases where high power is not required. It is also possible that these shorter wavelength systems could be applied in optical coherence tomography systems [74, 75]. Efforts directed towards short wavelength microcomb operation include 1 μm microcombs in silicon nitride microresonators [76] as well as harmonically-generated combs. The latter have successfully converted near-IR comb light to shorter wavelength bands and even into the visible band [77, 78] within the same resonator used to create the initial comb of near-IR frequencies. Also, crystalline resonators [79] and silica microbubble resonators [80] have been dispersion-engineered for comb generation in the 700 nm band. Finally, diamond-based microcombs afford the possibility of broad wavelength coverage [42]. However, none of the short wavelength microcomb systems have so far been able to generate stable mode-locked microcombs as required in all comb applications.

A key impediment to mode-locked microcomb operation at short wavelengths is material dispersion associated with the various dielectric materials used for microresonator fabrication. At shorter wavelengths, these materials feature large normal dispersion that dramatically increases into the visible and ultra-violet bands. While dark soliton pulses can be generated in a regime of normal dispersion [81], bright solitons require anomalous dispersion. Dispersion engineering by proper design of the resonator geometry [79, 80, 82] offers a possible way to offset the normal dispersion. Typically, by compressing the waveguide dimension of a resonator, geometrical dispersion will ultimately compensate a large normal material dispersion component to produce overall anomalous dispersion. For example, in silica, strong confinement in bubble resonators [80] and straight waveguides [83] has been used to push the anomalous dispersion transition wavelength from the near-IR into the visible band. Phase matching to ultra-violet dispersive waves has also been demonstrated using this technique [83]. However, to compensate the rising material dispersion, this compression must increase as the operational wavelength is decreased, and as a side effect, highly-confined waveguides tend to suffer increased

optical losses. This happens because mode overlap with the dielectric waveguide interface is greater with reduced waveguide cross section. Consequently, the residual fabrication-induced roughness of that interface degrades the resonator Q factor and increases pumping power (e.g., comb threshold power varies inverse quadratically with Q factor [32]).

Minimizing material dispersion provides one way to ease the impact of these constraints. In this sense, silica offers an excellent material for short wavelength operation, because it has the lowest dispersion among all on-chip integrable materials. For example, at 778 nm, silica has a group velocity dispersion (GVD) equal to 38 $ps^2\ km^{-1}$, which is over 5 times smaller than the GVD of silicon nitride at this wavelength ($> 200\ ps^2\ km^{-1}$)[84]. Other integrable materials that are also transparent in the visible, such as diamond [42] and aluminium nitride [85], have dispersion that is similar to or higher than silicon nitride. Silica also features a spectrally-broad low-optical-loss window so that optical Q factors can be high at short wavelengths. Here we demonstrate soliton microcombs with pump wavelengths of 1064 nm and 778 nm. These are the shortest soliton microcomb wavelengths demonstrated to date. By engineering geometrical dispersion and by employing mode hybridization, a net anomalous dispersion is achieved at these wavelengths while also maintaining high optical Q factors (80 million at 778 nm, 90 million at 1064 nm). The devices have large (millimetre-scale) diameters and produce single soliton pulse streams at rates that are both detectable and processable by low-cost electronic circuits. Besides illustrating the flexibility of silica for soliton microcomb generation across a range of short wavelengths, these results are relevant to potential secondary time standards based on transitions in rubidium [4]. Using dispersive-wave engineering in silica, it might also be possible to extend the emission of these combs into the ultra-violet as recently demonstrated in compact silica waveguides [83].

4.2 Silica resonator geometry and dispersion design

The silica resonator used in this work is shown schematically in Fig.4.1a. A fundamental mode profile is overlaid onto the cross-sectional rendering. The resonator design is a variation on the wedge resonator [86], and its geometry can be fully characterized by its resonator diameter, silica thickness (t), and wedge angle (θ) (see Fig. 4.1a). The diameter of all resonators in this work (and the assumed diameter in all simulations) is 3.2 mm, which corresponds to a free spectral range (FSR) of approximately 20 GHz, and the resonator thickness is controlled to obtain net anomalous dispersion at the design wavelengths, as described in detail below.

Further details on fabrication are given elsewhere [86]. As an aside, we note that a waveguide-integrated version of this design is also possible [87]. Adaptation of that device using the methods described here would enable full integration with other photonic elements on the silicon chip.

Fig. 4.1(**b**) illustrates how the geometrical dispersion induced by varying resonator thickness t offsets the material dispersion. Regions of anomalous and normal dispersion are shown for the TM1 mode family of a resonator having a wedge angle of 40°. The plots show that thinner resonators enable shorter wavelength solitons. Accordingly, three device types (I, II, and III shown as the colored dots in Fig. 4.1(**b**)) are selected for soliton frequency comb operation at three different pump wavelengths. At a pump wavelength of 1550 nm, the anomalous dispersion window is wide because bulk silica possesses anomalous dispersion at wavelengths above 1270 nm. For this type I device, a 7.9-μm thickness was used. Devices of type II and III have thicknesses near 3.4 μm and 1.5 μm for operation with pump wavelengths of 1064 nm and 778 nm, respectively. Beyond geometrical control of dispersion, the type III design also uses mode hybridization to substantially boost the anomalous dispersion. This hybridization occurs within a relatively narrow wavelength band which tunes with t (darker green region in Fig. 4.1(**b**)), and is discussed in detail below. Measured Q factors for the three device types are plotted in the upper panel of Fig. 4.1(**c**). Maximum Q factors at thicknesses which also produce anomalous dispersion were: 280 million (Type I, 1550 nm), 90 million (Type II, 1064 nm), and 80 million (Type III, 778 nm).

Using these three designs, soliton frequency combs were successfully generated with low threshold pump power. Shown in Fig. 4.1(**d**) is a photograph of a type III device under conditions where it is generating solitons. Fig. 4.1(**e**) shows optical spectra of the soliton microcombs generated for each device type. A slight Raman-induced soliton self-frequency-shift is observable in the type I and type II devices [38, 88–90]. The pulse width of the type III device is longer and has a relatively smaller Raman shift, which is consistent with theory [90]. The presence of a dispersive wave in this spectrum also somewhat offsets the smaller Raman shift [43]. Scanning electron microscope (SEM) images appear as insets in Fig. 4.1(**e**) and provide cross-sectional views of the three device types. It is worthwhile to note that microcomb threshold power, expressed as $P_{\mathrm{th}} \sim A_{\mathrm{eff}}/\lambda_{\mathrm{P}} Q^2$ (λ_{P} is pump wavelength and A_{eff} is effective mode area) remains within a close range of powers for all devices (lower panel of Fig. 4.1c). This can be understood to result from

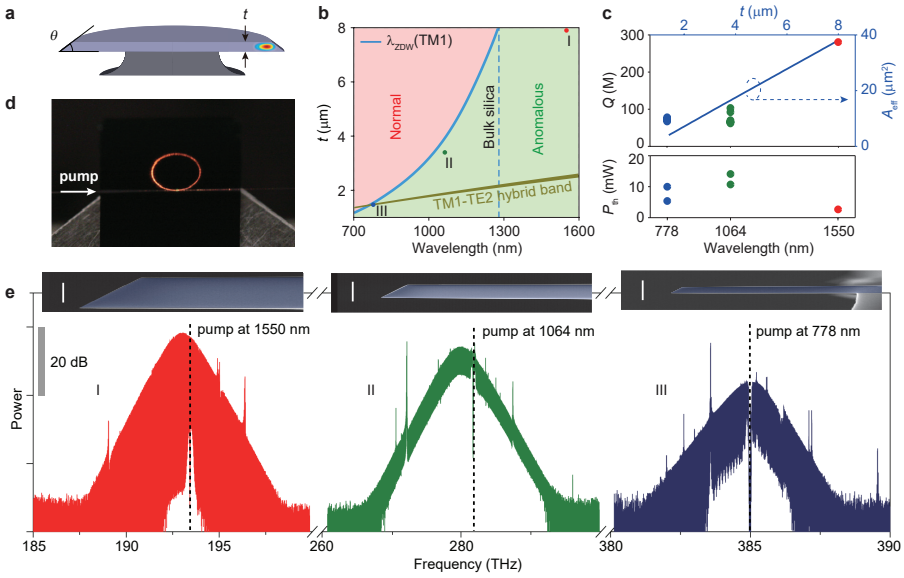

Figure 4.1: **Soliton frequency comb generation in dispersion-engineered silica resonators.** (**a**) A rendering of a silica resonator with the calculated TM1 mode profile superimposed. (**b**) Regions of normal and anomalous dispersion are shown versus silica resonator thickness (t) and pump wavelength. The zero dispersion wavelength (λ_{ZDW}) for the TM1 mode appears as a blue curve. The dark green band shows the 10-dB bandwidth of anomalous dispersion created by TM1-TE2 mode hybridization. The plot is made for a 3.2-mm-diameter silica resonator with a 40° wedge angle. Three different device types I, II, and III (corresponding to t = 7.9 μm, 3.4 μm and 1.5 μm) are indicated for soliton generation at 1550 nm, 1064 nm and 778 nm. (**c**) Measured Q factors and parametric oscillation threshold powers versus thickness and pump wavelength for the three device types. Powers are measured in the tapered fiber coupler under critical coupling. Effective mode area (A_{eff}) of the TM1 mode family is also plotted as a function of wavelength and thickness. (**d**) A photograph of a silica resonator (Type III device pumped at 778 nm) while generating a soliton stream. The pump light is coupled via a tapered fiber from the left side of the resonator. The red light along the circumference of the resonator and at the right side of the taper is believed to result from short wavelength components of the soliton comb. (**e**) Soliton frequency comb spectra measured from the devices. The red, green and blue soliton spectra correspond to device types I, II, and III designed for pump wavelengths 1550 nm, 1064 nm and 778 nm, respectively. Pump frequency location is indicated by a dashed vertical line. The soliton pulse repetition rate of all devices is about 20 GHz. Differences in signal-to-noise ratio (SNR) of the spectra originate from the resolution of the optical spectrum analyser (OSA). In particular, the 778 nm comb spectrum was measured using the second-order diffracted spectrum of the OSA, while other comb spectra were measured as first-order diffracted spectra. Insets: cross-sectional scanning electron microscope (SEM) images of the fabricated resonators. White scale bar is 5 μm.

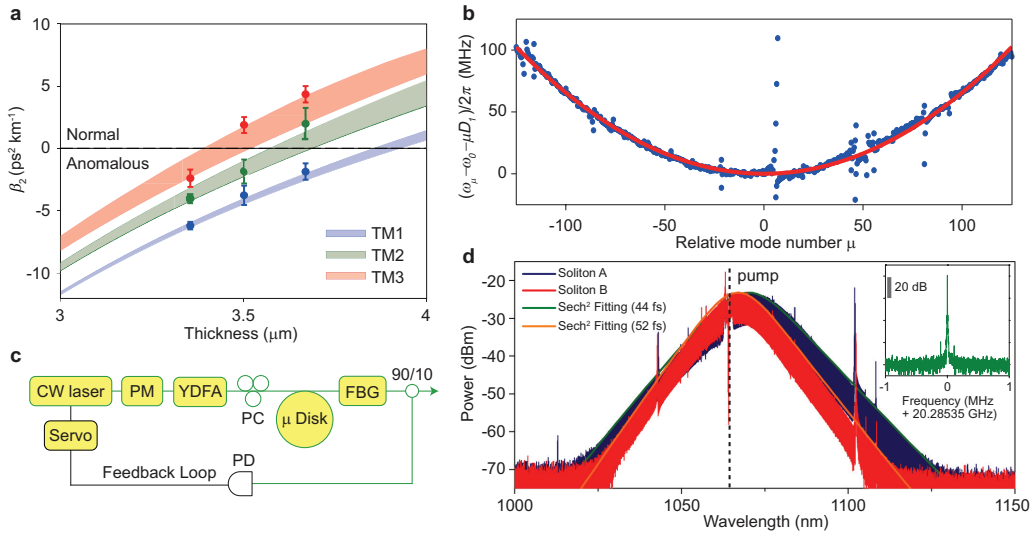

Figure 4.2: **Microresonator dispersion engineering and soliton generation at 1064 nm.** (**a**) Simulated group velocity dispersion (GVD) of TM mode families versus resonator thickness. The angle of the wedge ranges from 30° to 40° in the colored regions. Measured data points are indicated and agree well with the simulation. The error bars depict standard deviations obtained from measurement of 8 samples having the same thickness. (**b**) Measured relative mode frequencies (blue points) plotted versus relative mode number of a soliton-forming TM1 mode family in a 3.4 μm thick resonator. The red curve is a parabolic fit yielding $D_2/2\pi = 3.3$ kHz. (**c**) Experimental setup for soliton generation. A continuous-wave (CW) fiber laser is modulated by an electro-optic phase modulator (PM) before coupling to a ytterbium-doped fiber amplifier (YDFA). The pump light is then coupled to the resonator using a tapered fiber. Part of the comb power is used to servo-control the pump laser frequency. FBG: fiber Bragg grating. PD: photodetector. PC: polarization controller. (**d**) Optical spectra of solitons at 1064 nm generated from the mode family shown in **b**. The two soliton spectra correspond to different power levels with the blue spectrum being a higher power and wider bandwidth soliton. The dashed vertical line shows the location of the pump frequency. The solid curves are sech^2 fittings. Inset: typical detected electrical beatnote showing soliton repetition rate. The weak sidebands are induced by the feedback loop used to stabilize the soliton. The resolution bandwidth is 1 kHz.

a partial compensation of reduced Q factor in the shorter wavelength devices by reduced optical mode area (see plot in Fig. 4.1(**c**)). For example, from 1550 nm to 778 nm the mode area is reduced by roughly a factor of 9, and this helps to offset a 3-times decrease in Q factor. The resulting P_{th} increase (5.4 mW at 778 nm versus approximately 2.5 mW at 1550 nm) is therefore caused primarily by the decrease in pump wavelength λ_{P}. In the following sections, additional details on the device design, dispersion, and experimental techniques used to generate these solitons are presented.

4.3 Soliton microcombs generation using pump at 1064 nm

Dispersion simulations for TM modes near 1064 nm are presented in Fig. 4.2(**a**) and show that TM modes with anomalous dispersion occur in silica resonators having oxide thicknesses less than 3.7 μm. Aside from the thickness control, a secondary method to manipulate dispersion is by changing the wedge angle (see Fig. 4.2(**a**)). Both thickness and wedge angle are well controlled in the fabrication process [82]. Precise thickness control is possible because this layer is formed through calibrated oxidation of the silicon wafer. Wedge angles between 30 and 40 degrees were chosen in order to maximize the Q factors [86]. The resonator dispersion is characterized by measuring mode frequencies using a scanning external-cavity diode laser (ECDL) whose frequency is calibrated using a Mach-Zehnder interferometer. As described elsewhere [37, 38], the mode frequencies, ω_μ, are Taylor expanded as $\omega_\mu = \omega_0 + \mu D_1 + \mu^2 D_2/2 + \mu^3 D_3/6$, where ω_0 denotes the pumped mode frequency, $D_1/2\pi$ is the FSR, and D_2 is proportional to the GVD, β_2 ($D_2 = -cD_1^2\beta_2/n_0$ where c and n_0 are the speed of light and material refractive index). D_3 is a third-order expansion term that is sometimes necessary to adequately fit the spectra (see discussion of 778 nm soliton below). The measured frequency spectrum of the TM1 mode family in a 3.4 μm thick resonator is plotted in Fig. 4.2b. The plot gives the frequency as relative frequency (i.e., $\omega_\mu - \omega_0 - \mu D_1$) to make clear the second-order dispersion contribution. The frequencies are measured using a radio-frequency calibrated Mach-Zehnder interferometer having a FSR of approximately 40 MHz. Also shown is a fitted parabola (red curve) revealing $D_2/2\pi = 3.3$ kHz (positive parabolic curvature indicates anomalous dispersion). Some avoided mode crossings are observed in the spectrum. The dispersion measured in resonators of different thicknesses, marked as solid dots in Fig. 4.2a, is in good agreement with numerical simulations.

The experimental setup for generation of 1064 nm pumped solitons is shown in Fig.

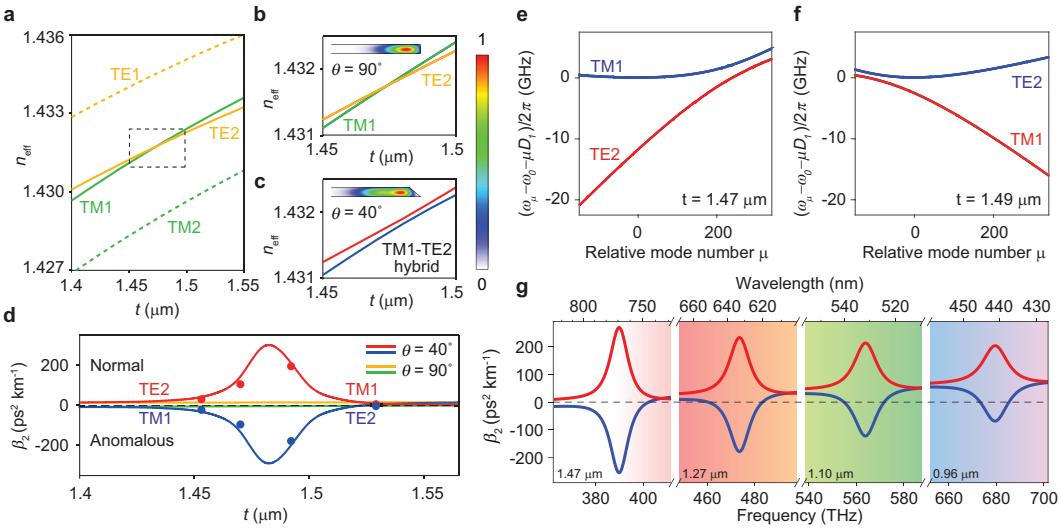

Figure 4.3: **Dispersion engineering and soliton generation at 778 nm.** (**a**) Calculated effective indices n_{eff} for TE1, TE2, TM1, and TM2 modes at 778 nm plotted versus thickness for a silica resonator with reflection symmetry (i.e., θ = 90°). The TM1 and TE2 modes cross each other without hybridization. (**b**) Zoom-in of the dashed box in panel **a**. (**c**) As in (**b**) but for a resonator with θ = 40°. An avoided crossing of TM1 and TE2 occurs due to mode hybridization. Insets of **b** and **c** show simulated mode profiles (normalized electric field) in resonators with θ = 90° and θ = 40°, respectively. The color bar is shown to the right. (**d**) Calculated group velocity dispersion (GVD) of the two modes. For the θ = 40° case, hybridization causes a transition in the dispersion around the thickness 1.48 μm. The points are the measured dispersion values. (**e**) (**f**) Measured relative mode frequencies of the TM1 and TE2 mode families versus relative mode number μ for devices with t = 1.47 μm and t = 1.49 μm. (**g**) Calculated total second-order dispersion versus frequency (below) and wavelength (above) at four different oxide thicknesses (number in lower left of each panel). Red and blue curves correspond to the two hybridized mode families. Anomalous dispersion is negative and shifts progressively to bluer wavelengths as thickness decreases. Background color gives the approximate corresponding color spectrum.

4.2c. The microresonator is pumped by a continuous wave (CW) laser amplified by a ytterbium-doped fiber amplifier (YDFA). The pump light and comb power are coupled to and from the resonator by a tapered fiber. Typical pumping power is around 100 mW. Solitons are generated while scanning the laser from higher frequencies to lower frequencies across the pump mode [37, 38, 43]. The pump light is modulated by an electro-optic PM to overcome the thermal transient during soliton generation [38, 43, 91]. A servo control referenced to the soliton power is employed to capture and stabilize the solitons [91]. Shown in Fig. 4.2d are the

optical spectra of solitons pumped at 1064 nm. These solitons are generated using the mode family whose dispersion is characterized in Fig. 4.2b. Due to the relatively low dispersion (small D_2), these solitons have a short temporal pulse width. Using the hyperbolic-secant-squared fitting method [38] (see orange and green curves in Fig. 4.2d), a soliton pulse width of 52 fs is estimated for the red spectrum. By increasing the soliton power (blue spectrum), the soliton can be further compressed to 44 fs, which corresponds to a duty cycle of 0.09% at the 20 GHz repetition rate. Finally, the inset in Fig. 4.2d shows the electrical spectrum of the photo-detected soliton pulse stream. Besides confirming the repetition frequency, the spectrum is very stable with excellent signal-to-noise ratio (SNR) greater than 70 dB at 1 kHz resolution bandwidth.

4.4 Soliton microcombs generation using pump at 778 nm

As the operational wavelength shifts further towards the visible band, normal material dispersion increases. To generate solitons at 778 nm, an additional dispersion engineering method, TM1-TE2 mode hybridization, is therefore added to supplement the geometrical dispersion control. The green band region in Fig. 4.1b gives the oxide thicknesses and wavelengths where this hybridization is prominent. Polarization mode hybridization is a form of mode coupling induced dispersion control. The coupling of the TM1 and TE2 modes creates two hybrid mode families, one of which features strong anomalous dispersion. This hybridization is caused when a degeneracy in the TM1 and TE2 effective indices is lifted by a broken reflection symmetry of the resonator [92]. The wavelength at which the degeneracy occurs is controlled by the oxide thickness and determines the soliton operation wavelength. Finite element method (FEM) simulation in Fig. 4.3a shows that at 778 nm, the TM1 and TE2 modes are expected to have the same effective index at the oxide thickness 1.48 μm when the resonator features a reflection symmetry through a plane that is both parallel to the resonator surface and that lies at the centre of the resonator. Such a symmetry exists when the resonator has vertical sidewalls or equivalently a wedge angle $\theta = 90^\circ$ (note: the wet-etch process used to fabricate the wedge resonators does not support a vertical side wall). A zoom-in of the effective index crossing is provided in Fig. 4.3b. In this reflection symmetric case, the two modes cross in the effective-index plot without hybridization. However, in the case of $\theta = 40^\circ$ (Fig. 4.3c), the symmetry is broken and the effective index degeneracy is lifted. The resulting avoided crossing causes a sudden transition in the GVD as shown in Fig. 4.3d, and one of the hybrid modes experiences enhanced anomalous dispersion.

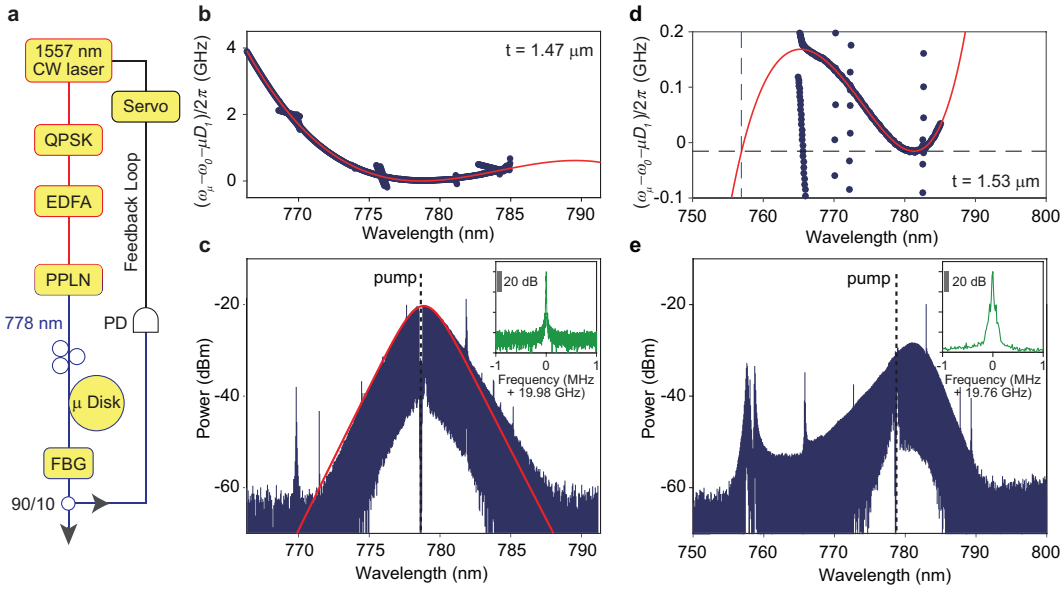

Figure 4.4: **Soliton generation at 778 nm.** (**a**) Experimental setup for soliton generation. A 1557 nm tunable laser is sent to a quadrature phase-shift keying modulator (QPSK) to utilize frequency-kicking and is then amplified by an erbium-doped fiber amplifier (EDFA). Then, a periodically-poled lithium niobate (PPLN) waveguide frequency-doubles the 1557 nm input into 778 nm output. The 778 nm pump light is coupled to the resonator for soliton generation. A servo loop is used to maintain pump locking. (**b**) Measured relative mode frequencies of the TM1 mode family versus wavelength for devices with t = 1.47 μm. A number of crossing mode families are visible. The red curve is a numerical fit using $D_2/2\pi$ = 49.8 kHz and $D_3/2\pi$ = 340 Hz. (**c**) Optical spectrum of a 778 nm soliton generated using the device measured in **b** with pump line indicated by the dashed vertical line. The red curve is a spectral fitting which reveals a pulse width of 145 fs. Most of the spurs in the spectrum correspond to the mode crossings visible in **b**. Inset shows the electrical spectrum of the detected soliton pulse stream. The resolution bandwidth is 1 kHz. (**d**) Measured relative mode frequencies of the TE2 mode family versus wavelength for devices with t = 1.53 μm. The red curve is a fit with $D_2/2\pi$ = 4.70 kHz and $D_3/2\pi$ = −51.6 Hz. (**e**) Optical spectrum of a soliton generated using the device measured in **d** with pump line indicated as the dashed vertical line. A dispersive wave is visible near 758 nm. Inset shows the electrical spectrum of the detected soliton pulse stream. The resolution bandwidth is 1 kHz.

To verify this effect, resonators having four different thicknesses (θ = 40°) were fabricated and their dispersion was characterized using the same method as for the 1064 nm soliton device. The measured second-order dispersion values are plotted as solid circles in Fig. 4.3d and agree with the calculated values given by the solid curves. Fig. 4.3e and Fig. 4.3f show the measured relative mode frequencies versus mode number of the two modes for devices with t = 1.47 μm and t = 1.49 μm. As

before, upward curvature in the data indicates anomalous dispersion. The dominant polarization component of the hybrid mode is also indicated on both mode-family branches. The polarization mode hybridization produces a strong anomalous dispersion component that can compensate normal material dispersion over the entire band. Moreover, the tuning of this component occurs over a range of larger oxide thicknesses for which it would be impossible to compensate material dispersion using geometrical control alone. To project the application of this hybridization method to yet shorter soliton wavelengths, Fig. 4.3g summarizes calculations of second order dispersion at a series of oxide thicknesses. At a thickness close to 1 micron, it should be possible to generate solitons at the blue end of the visible spectrum. Moreover, wedge resonators having these oxide film thicknesses have been fabricated during the course of this work. They are mechanically stable with respect to stress-induced buckling [93] at silicon undercut values that are sufficient for high-Q operation.

For soliton generation, the microresonator is pumped at 778 nm by frequency-doubling a continuous wave (CW) ECDL operating at 1557 nm (see Fig. 4.4a). The 1557 nm laser is modulated by a quadrature phase-shift keying (QPSK) modulator for frequency-kicking, and then amplified by an erbium-doped fiber amplifier (EDFA). The amplified light is sent into a periodically-poled lithium niobate (PPLN) device for second-harmonic generation. The frequency-doubled output pump power at 778 nm is coupled to the microresonator using a tapered fiber. The pump power is typically about 135 mW. The soliton capture and locking method was again used to stabilize the solitons [91]. A zoom-in of the TM1 mode spectrum for t = 1.47 μm with a fit that includes third-order dispersion (red curve) is shown in Fig. 4.4b. The impact of higher order dispersion on dissipative soliton formation has been studied [37, 94]. In the present case, the dispersion curve is well suited for soliton formation. The optical spectrum of a 778 nm pumped soliton formed on this mode family is shown in Fig. 4.4c. It features a temporal pulse width of 145 fs as derived from a sech^2 fit (red curve). The electrical spectrum of the photo-detected soliton stream is provided in the inset in Fig. 4.4c and exhibits high stability.

Fig. 4.4d gives the measured mode spectrum and fitting under conditions of slightly thicker oxide (t = 1.53 μm). In this case, the polarization of the hybrid mode more strongly resembles the TE2 mode family. The overall magnitude of second-order dispersion is also much lower than for the more strongly hybridized soliton in Fig. 4.4b and Fig. 4.4c. The corresponding measured soliton spectrum is shown in

Fig. 4.4e and features a dispersive wave near 758 nm. The location of the wave is predicted from the fitting in Fig. 4.4d (see dashed vertical and horizontal lines). The dispersive wave exists in a spectral region of overall normal dispersion, thereby illustrating that dispersion engineering can provide a way to further extend the soliton spectrum towards the visible band. As an aside, the plot in Fig. 4.4d has incorporated a correction to the FSR (D_1) so that the soliton line is given as the horizontal dashed black line. This correction results from the soliton red spectral shift relative to the pump that is apparent in Fig. 4.4e. This shift results from a combination of the Raman self shift [89, 90] and some additional dispersive wave recoil [43]. Finally, the detected beat note of the soliton and dispersive wave is shown as the inset in Fig. 4.4e. It is overall somewhat broader than the beatnote of the other solitons, but is nonetheless quite stable.

4.5 Discussion

We have demonstrated soliton microcombs at 778 nm and 1064 nm using on-chip high-Q silica resonators. Material-limited normal dispersion, which is dominant at these wavelengths, was compensated by using geometrical dispersion through control of the resonator thickness and wedge angle. At the shortest wavelength, 778 nm, mode hybridization was also utilized to achieve anomalous dispersion while maintaining high optical Q. These results are the shortest wavelength soliton microcombs demonstrated to date. Moreover, the hybridization method can be readily extended so as to produce solitons over the entire visible band. The generated solitons have pulse repetition rates of 20 GHz at both wavelengths. Such detectable and electronics-compatible repetition rate soliton microcombs at short wavelengths have direct applications in the development of miniature optical clocks [4] and potentially optical coherence tomography [74, 75]. Also, any application requiring low-power near-visible mode-locked laser sources will benefit. The same dispersion control methods used here should be transferable to silica ridge resonator designs that contain silicon nitride waveguides for on-chip coupling to other photonic devices [87]. Dispersive wave generation at 758 nm was also demonstrated. It could be possible to design devices that use solitons formed at either 778 nm or 1064 nm for dispersive-wave generation into the visible and potentially into the ultra-violet as has been recently demonstrated using straight silica waveguides [83].

Chapter 5

LOW POWER OPERATION OF SOLITON MICROCOMBS ALONG ISO-CONTOURS

[1]Dissipative Kerr solitons can be generated within an existence region defined on a space of normalized pumping power versus cavity-pump detuning frequency. The contours of constant soliton power and constant pulse width in this region are studied through measurement and simulation. Such iso-contours impart structure to the existence region and improve understanding of soliton locking and stabilization methods. As part of the study, dimensionless, closed-form expressions for soliton power and pulse width are developed (including Raman contributions). They provide iso-contours in close agreement with those from the full simulation, and, as universal expressions, can simplify the estimation of soliton properties across a wide range of systems.

Temporal optical solitons resulting from the balance of dispersion with the Kerr nonlinearity have long been studied in optical fiber systems [96, 97]. In addition to their many remarkable properties, these nonlinear waves are important in mode locking [98], continuum generation [99], and were once considered as a means to send information over great distances [100, 101]. Recently, a new type of dissipative temporal soliton [102] was observed in optical fiber resonators [36]. These coherently driven cavity solitons (CSs) were previously considered a theoretical possibility [35], and related soliton phenomena including breather solitons and Raman interactions have also been reported in this system [103–105]. While leveraging the Kerr effect to balance dispersion, this soliton also regenerates using Kerr-induced parametric amplification [32]. Their recent demonstration in microcavity systems [37–40, 43, 44, 71] has made possible highly stable frequency microcombs [34, 67]. Referred to as dissipative Kerr solitons (DKs) in the microcavity system, soliton phenomena including the Raman self-shift [89, 90, 106], optical Cherenkov radiation [43, 106–109], multi-soliton systems [110–112], and the co-generation of new types of solitons [68] have been reported. Moreover, the compact soliton microcomb devices are being studied for systems-on-a-chip applications such

[1]Work presented in this chapter has been published in [95] "Universal iso-contours for dissipative Kerr solitons", *Optics Letters* 43 11, 2567-2570 (2018). Boqiang Shen conducted the experiment, did the numerical simulation, prepared the data, and participated in the writing of the manuscript.

as dual-comb spectroscopy [11], precision distance measurement [16, 17], optical communications [113], and optical frequency synthesis [9].

5.1 Dissipative Kerr soliton phase diagram and iso-power contours

Regions of stability and existence are well known in driven soliton systems [114]. These properties of DKs and CSs have been studied using the Lugiato-Lefever (LL) equation [35, 115] in a space of normalized pumping power and cavity-pump frequency detuning [37, 116–118]. In analogy with thermodynamic phase diagrams, this soliton existence diagram also contains other regions of existence including those for breather solitons as well as more complex dynamical phenomena [119–121]. Fig. 5.1 is a typical diagram showing only the stable soliton region. In thermodynamic phase diagrams, another useful construct is the iso-contour for processes performed with a state variable held constant (e.g., isochors and isotherms). These contours not only provide a way to understand processes within the framework of the phase diagram, but impart structure to the phase diagram that improves intuition of thermodynamical processes. In this work, contours of constant soliton power and constant pulse width are measured and compared with theory. Closed-form expressions for normalized power and pulsewidth are also developed including the Raman process.

The normalized LL equation is shown below as Eq. 5.1 [37]. The slowly-varying field envelope ψ is defined such that $|\psi|^2 = (2g/\kappa)N$ where N is photon number, κ is the cavity mode power damping rate, and $g = \hbar\omega_c^2 c n_2/(n^2 V_0)$ is the Kerr coefficient with material refractive index n, Kerr nonlinear index n_2, optical mode volume V_0, cavity resonant frequency ω_c, Planck's constant $\hbar$, and speed of light c. $\tau = \kappa t/2$ and $\theta \equiv \phi\sqrt{\kappa/2D_2}$ are the normalized time and cavity polar coordinate (ϕ) where D_2 is the second-order dispersion parameter [37, 38]. $f^2 \equiv P/P_{\text{th}}$ is the ratio of the input pump power and parametric threshold power [32, 38] and $\zeta \equiv (\omega_c - \omega_p)(2/\kappa)$ is the normalized frequency detuning between cavity resonant frequency ω_c, and pump frequency ω_p. $\gamma \equiv D_1\tau_R\sqrt{\kappa/2D_2}$ is the normalized Raman coefficient where τ_R is the material Raman constant [90] and $D_1/2\pi$ is the cavity free-spectral-range [37, 38].

$$\frac{\partial\psi}{\partial\tau} = j\frac{1}{2}\frac{\partial^2\psi}{\partial\theta^2} + j|\psi|^2\psi - (1 + j\zeta)\psi + j\gamma\frac{\partial|\psi|^2}{\partial\theta}\psi + f. \tag{5.1}$$

Iso-power contours found by solving Eq. 5.1 are shown in Fig. 5.1 as red contours. The analysis is performed for a high-Q silica resonator and parameters used in the calculation are provided below and in the Fig. 5.1 caption. Numerical simulation is

based on propagating the LL equation from an initial soliton seed until steady-state is achieved [90].

The following simplified analytical solution is also used to study soliton behavior [37]: $\psi = A + B\ \mathrm{sech}(\theta/\tau_\theta)e^{\iota\phi_0}$, where A is the soliton background field, B is the amplitude, ϕ_0 is the soliton phase, and $\tau_\theta \equiv \tau_\mathrm{s}/\tau_0$ is the normalized soliton pulse width (τ_s is the physical pulse width and $\tau_0 \equiv \sqrt{2D_2/(\kappa D_1^2)}$). By Fourier transform, the soliton spectrum in optical frequency ν varies as $\mathrm{sech}(\nu/\nu_\mathrm{s})$ where $\nu_\mathrm{s}\tau_\mathrm{s} = \pi^{-2}$. Approximate expressions giving the Raman-free dependence of amplitude and pulse width on detuning and pump power have been developed [37, 118]. By including high-order corrections and Raman corrections, the following improved expressions result as well in an expression for soliton average power,

$$B(\zeta, f, \gamma) \approx \sqrt{2\zeta}\left(1 + \frac{5}{8}\sqrt{\frac{\pi^2 f^2 - 8\zeta}{2\zeta^3}}\right)\left(1 - \frac{64}{225}\gamma^2\zeta^3\right) \tag{5.2}$$

$$\tau_\theta(\zeta, f, \gamma) \approx \frac{1}{\sqrt{2\zeta}}\left(1 - \frac{1}{4}\sqrt{\frac{\pi^2 f^2 - 8\zeta}{2\zeta^3}}\right)\left(1 + \frac{64}{225}\gamma^2\zeta^3\right) \tag{5.3}$$

$$p(\zeta, f, \gamma) \approx \sqrt{2\zeta}\left(1 + \sqrt{\frac{\pi^2 f^2 - 8\zeta}{2\zeta^3}}\right)\left(1 - \frac{64}{225}\gamma^2\zeta^3\right) \tag{5.4}$$

where $p \equiv P_\mathrm{sol}/P_0$ is the normalized time-averaged soliton power P_sol and $P_0 \equiv (\kappa_E\hbar\omega_\mathrm{c}/\pi g)\sqrt{\kappa D_2/2}$ with κ_E the optical loss rate from waveguide-resonator coupling [38]. As an aside, the requirement of the square root to be real in these expressions ($\zeta < \pi^2 f^2/8$) gives the approximate upper bound of detuning for soliton existence in the phase diagram [37, 94, 114]. Dotted lines in Fig. 5.1 are the iso-power contours using Eq. 5.4 (equivalently $p(\zeta, f, \gamma) =$ Constant for $\gamma = 2.1 \times 10^{-3}$), and they are in excellent agreement with the simulation contours. Raman contributions become especially important at larger detuning values where the soliton spectrum increases in width [89, 90]. To illustrate this point, the dashed curves in Fig. 5.1 result by using Eq. 5.4 except with $\gamma = 0$.

5.2 Measurement system and low power operation

The experimental setup is shown in Fig. 5.2a. The resonator was an ultra-high-Q silica wedge resonator having a diameter of approximately 3 mm (free spectral range $D_1/2\pi = 21.9$ GHz). Further details on its fabrication are presented elsewhere [86].

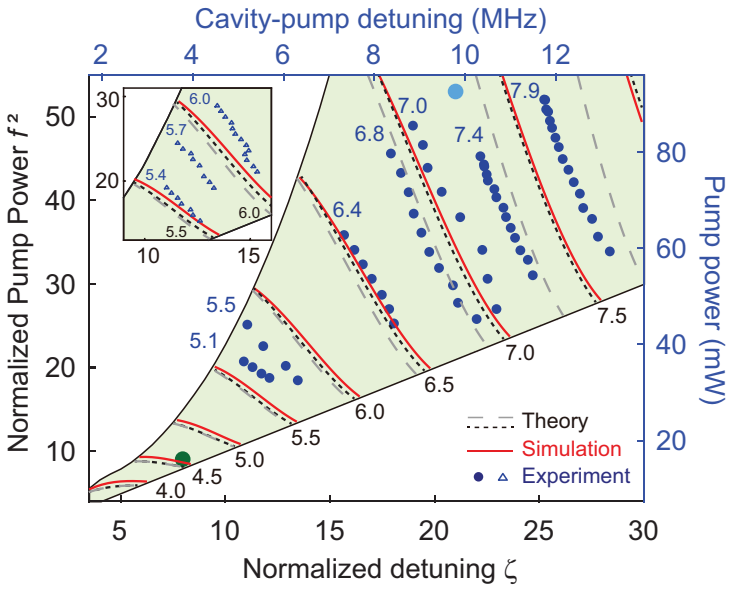

Figure 5.1: **Dissipative Kerr soliton phase diagram and iso-power contours.** The phase diagram features normalized pump power f^2 along the vertical axis and normalized detuning ζ along the horizontal axis. The green region contains stable soliton states. Black dotted lines (gray dashed lines) are iso-power contours using Eq. 5.4 with Raman term (w/o Raman). p is incremented from 4.0 to 8.0 in steps of 0.5. Red lines are simulated iso-power contours using Eq. 5.1. Blue dots give the measured soliton iso-power contours at the following soliton powers: 93, 99.5, 117.5, 125, 129, 136, 145 μW (left to right), which correspond to p values of 5.1, 5.5, 6.4, 6.8, 7.0, 7.4, and 7.9. For these measurements, Q = 197 million ($\kappa/2\pi$ = 0.98 MHz), κ_E/κ = 0.26, and $\gamma = 2.1 \times 10^{-3}$. Inset shows the measured iso-power contours using another similar device, with soliton powers of 299, 320, and 335 μW (left to right), which correspond to p values of 5.4, 5.7, and 6.0. For these measurements, Q = 115 million ($\kappa/2\pi$ = 1.69 MHz), κ_E/κ = 0.39, and $\gamma = 2.8 \times 10^{-3}$. Large green and blue data points correspond to spectra in Fig. 5.2

The measurement used the TE_1 mode family pumped at 1550 nm and the second-order dispersion was measured to be $D_2/2\pi$ = 12.1 kHz at 1550 nm by a method reported elsewhere [38]. The mode area was calculated to be A_{eff} = 40 μm^2 and the silica Raman constant τ_R = 2.4 fs was also used [90], which is valid when the soliton spectral width is below 13 THz [122]. Finally, the resonator used in this measurement featured minimal avoided mode crossings and dispersive waves. Their presence would interfere with the ideal power dependence predicted by the LL equation. To measure pump detuning, weak phase-modulation of the pump light and detection of converted amplitude modulation sidebands was performed [118, 123]. In this method, pump light reflected by the fiber Bragg grating (FBG) contains the

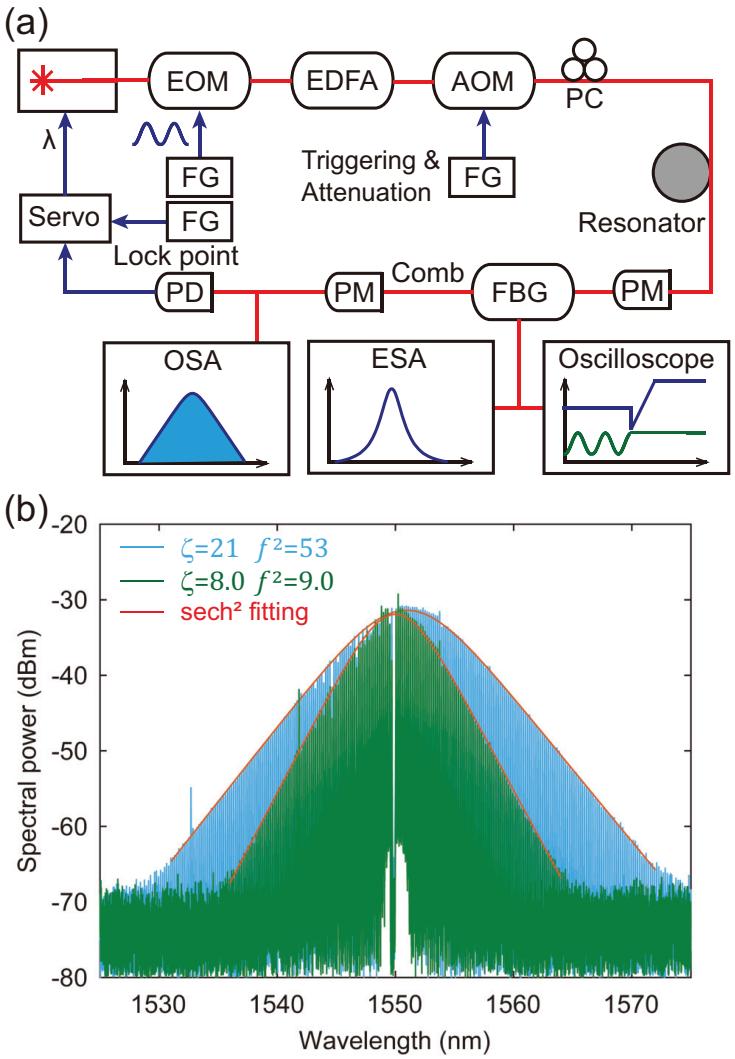

Figure 5.2: **Measurement system and low power operation.** (**a**) Measurement setup. EOM: electro-optical phase modulator. PC: polarization controller. PM: In-line power meter. PD: Photodetector. FG: function generator. (**b**) Soliton spectra at normalized detuning and pumping power ($\zeta = 21$, $f^2 = 53$) (blue) and ($\zeta = 8.0$, $f^2 = 9.0$) (green). The corresponding phase diagram locations are marked in Fig. 5.1. Red curve: squared hyperbolic-secant fitting.

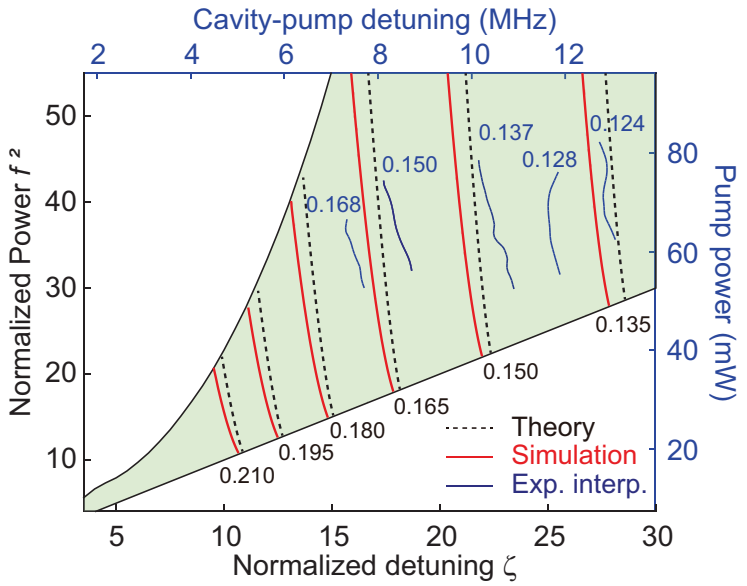

Figure 5.3: **Iso-contours of soliton pulse width.** The device is unchanged from Fig. 5.1 main panel. Red solid lines (black dotted lines) are simulated (Eq. 5.3 theory) iso-contours of normalized pulse width τ_θ ranging from 0.21 to 0.135 (equidistant steps of 0.015). Blue solid lines are the linear interpolation from measurement of iso-contours at 190, 170, 155, 145, 140 fs, which correspond to τ_θ: 0.168, 0.150, 0.137, 0.128, 0.124.

modulation information and is analyzed by an electrical spectrum analyzer (ESA) to retrieve the detuning frequency. The soliton spectrum transmitted past the FBG is sent to a detector and optical spectrum analyzer (OSA) for analysis. To determine soliton power, the FBG filtered line was manually reinserted.

5.3 Iso-contours of soliton pulse width

Triggering and locking of single soliton states used the soliton average power to servo control the pump laser frequency [91]. Because this soliton locking method maintains a constant soliton power, it provides a convenient way to map out the iso-power contours. Specifically, as opposed to varying (ζ, f^2) in the phase diagram and monitoring soliton power, the iso-power measurement proceeded by varying only the pumping power with the soliton locked at constant output power. The servo control then compensates for these variations by adjusting the pumping frequency. The corresponding detuning was then recorded as described above. Pump power was varied using a combination of an acousto-optical modulator (AOM) and Erbium-doped fiber amplifier (EDFA). Upon completion of an iso-power contour, the soliton power setpoint was adjusted and the measurement repeated. The measured iso-power

data points are shown in the main panel of Fig. 5.1. Each measurement proceeded until it was no longer possible to reliably lock the soliton state. There is overall good agreement between measurement and theory. Errors are largest at lowest detuning values, however, even here they are relatively small (~10%). The ability to measure the contours over such large ranges and their good agreement with theory and simulations showcases the system's robustness and quality. As an additional test, a second loading condition was also measured. The inset to Fig. 5.1 shows this data, which is in reasonable agreement with simulation and Eq. 5.4. Measured soliton powers have experienced an ~1.2 dB insertion loss between the resonator and the detector. It is also noted that breather solitons could be stably locked near the upper boundary in Fig. 5.1. However, the region was small, making measurement of iso-power contours difficult. As a result, breathers were not studied in this work.

Stable generation of solitons at small detuning is of practical importance for low pumping power operation of the soliton system. To this end, the green data point (ζ=8.0, f^2=9.0) in Fig. 5.1 shows both the lowest detuning and the lowest power soliton state observed in this study. The corresponding unnormalized quantities are 4.2 MHz and 10.8 mW. This is, to the authors' knowledge, the lowest operating power reported for any soliton microcomb platform. Making this result equally important is that the repetition rate is detectable (21.9 GHz) requiring large mode volume and hence higher pumping power levels as compared to, for example, THz-rate microcombs. Corresponding soliton spectra are presented in Fig. 5.2(**b**). The result was achieved by both the use of a high-quality-factor resonator sample as well as the improved understanding gained through these measurements of the stability regional boundaries [91]. For comparison, a soliton spectrum produced at (ζ=21, f^2=53) is also shown in Fig. 5.2(**b**). These values are plotted as the light blue data point in Fig. 5.1 and correspond to unnormalized quantities 11.3 MHz and 63.5 mW. The cavity loading condition for these two spectra is: loaded Q = 182 million and $\kappa_E/\kappa = 0.44$.

In parallel with the iso-power data point collection, the soliton pulse width was also measured by fitting of the optical spectral envelope [38]. Then the data set (ζ, f^2, τ_θ) was linearly interpolated to determine iso-contours of pulse width (blue contours in Fig. 5.3). It was not possible to interpolate iso-pulse-width contours at lower detuning values where there are fewer iso-power data points. For comparison, simulated pulse width (red) and the analytical expression, Eq. 5.3 (dotted black) are plotted. The interpolated pulse width iso-contours are less accurate than the directly

measured power contours but nonetheless show reasonable agreement between the data and theory. Overall, the pulse width contours are more weakly dependent upon normalized pumping power (i.e., more vertical) as compared to the soliton power contours.

5.4 Summary

Contours of constant power and constant pulse width have been measured for dissipative Kerr solitons. Measurements were found to be in good agreement with the LL equation numerical model augmented by Raman interactions. There was also good agreement with the predictions of closed-form expressions that include the Raman interaction. Compared with the the large-detuning approximation which predicts that soliton power depends only upon resonator-pump detuning (i.e., vertical iso-power contours), it is found that soliton power depends both upon pumping power and detuning. The resulting tilt of iso-power contours at low detuning suggests that soliton locking by servo control of pumping power could potentially be an option for low-detuning ranges just as servo control of pump frequency is used at larger detuning ranges. Stable soliton operation for pump powers as low as 10.8 mW was also demonstrated in the course of this work. These measurements provide structure to the phase diagram picture of soliton existence. The universal nature of the closed-form expressions should make them suitable for use in other CS and DK soliton platforms. Future work could consider incorporating higher order dispersion into the analysis to include, for example, the impact of phenomena such as dispersive waves.

Chapter 6

VERNIER SPECTROMETER USING DUAL-LOCKED COUNTERPROPAGATING SOLITON MICROCOMBS

[1] Frequency-agile lasers are ubiquitous in sensing, spectroscopy, and optical communications [124–126], and measurement of their optical frequency for tuning and control is traditionally performed by grating and interferometer-based spectrometers, but more recently these measurements can make use of optical frequency combs [1]. Frequency combs provide a remarkably stable measurement grid against which optical signal frequencies can be determined subject to the ambiguity introduced by the equally spaced comb teeth. The ambiguity is resolved for continuously frequency swept signals by counting comb teeth [127] relative to a known comb tooth, and this method has enabled measurement of remarkably high chirp rates [128]. However, many signal sources will experience intentional or unintentional frequency jumps. Here, the ambiguity can be resolved using a second frequency comb that has a different comb tooth spacing so as to provide a frequency Vernier scale for comparison with the first comb [129–131]. This Vernier concept is also used in dual comb spectroscopy [10, 11], but in measuring active signals, the method can be enhanced to more directly (and hence quickly) identify signal frequencies through a signal correlation technique [131]. Moreover, continuous as opposed to discretely sampled frequencies are measured in the active approach. The power of the Vernier-based method relies upon mapping of optical comb frequencies into a radio-frequency grid of frequencies, the precision of which is set by the relative line-by-line frequency stability of the two frequency combs. This stability can be guaranteed by self-referencing each comb using a common high-stability radio-frequency source or through optical locking of each comb to reference lasers whose relative stability is ensured by mutual locking to a common optical cavity.

In this chapter, we show that a single microresonator provides rapid and broad-band measurement of optical frequencies with a relative frequency precision comparable to conventional dual frequency comb systems. Dual-locked counter-propagating (CP) solitons having slightly different repetition rates are used to implement a

[1] Work presented in this chapter has been published in [14] "Vernier spectrometer using counterpropagating soliton microcombs", *Science* 363, 965-968 (2019). Boqiang Shen conducted the experiment, prepared the data, and participated in the writing of the manuscript.

Vernier spectrometer. Laser tuning rates as high as 10 THz/s, broadly step-tuned lasers, multi-line laser spectra, and also molecular absorption lines are characterized using the device. Besides providing a considerable technical simplification through the dual-locked solitons and enhanced capability for measurement of arbitrarily tuned sources, our results reveal possibilities for chip-scale spectrometers that exceed the performance of table-top grating and interferometer-based devices.

6.1 Concept of Vernier spectrometer

We demonstrate a broad-band, high-resolution Vernier microresonator soliton spectrometer (MSS) using a single miniature comb device that generates two mutually-phase-locked combs. The principle of operation relies upon an optical phase locking effect observed in the generation of counter-propagating solitons within high-Q whispering gallery resonators [110]. Soliton generation in microresonators is being studied for miniaturization to the chip-scale of complete comb systems and these soliton microcombs have now been demonstrated in a wide range of microresonator systems [41]. It has been shown that counter-propagating solitons can have distinct, controllable repetition rates and that their underlying comb spectra can be readily phase locked at two spectral points [110]. This mutual double-locking creates line-by-line relative frequency stability for the underlying microcomb spectra that is more characteristic of fully self-referenced dual comb systems. The resulting Vernier of comb frequencies in the optical domain maps to an exceptionally stable radio frequency grid for implementation of the spectrometer.

Phase-locked CP solitons

The spectral relationship of the doubled-locked cw and ccw solitons reveals the inherent optical frequency Vernier (Figure 6.1(**a**)). A single laser source is modulated (Figure 6.1(**b**)) to produce the two mutually-coherent pump lines at order $\mu = N$ with frequency separation $\Delta\nu$ (MHz range). The distinct pump frequencies cause the soliton repetition rates to differ by Δf_r as a result of the Raman self-frequency-shift [88–90, 110, 132]. As detailed elsewhere, the cw and ccw combs will experience frequency locking (induced by optical backscattering) at order $\mu = 0$ for certain pumping frequencies [110]. This locking requires that $\Delta\nu = N\Delta f_r$. Also, because the two pump frequencies are derived from radio-frequency modulation of a single laser source, they have a high relative frequency stability ($\Delta\nu$ is very stable) and are effectively locked at order $\mu = N$. This double locking sets up a stable Vernier in the respective soliton comb frequencies. The counter-propagating solitons are

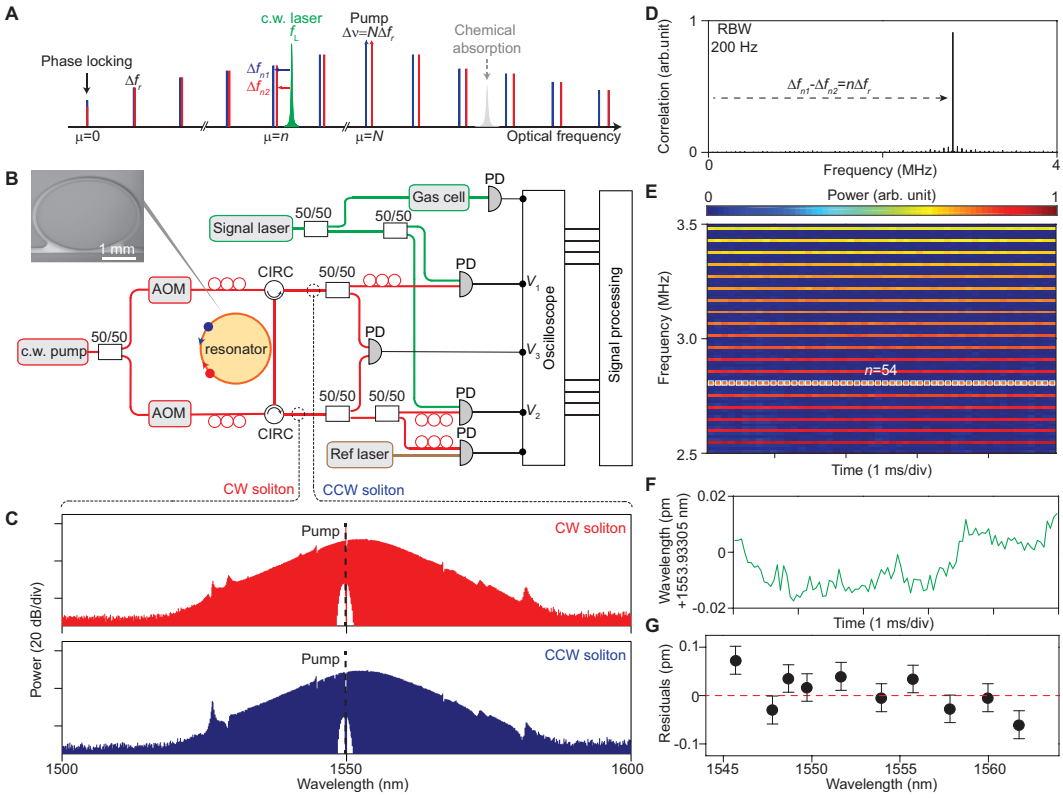

Figure 6.1: **Spectrometer concept, experimental setup and static measurement.** (**a**) Counter propagating soliton frequency combs (red and blue) feature repetition rates that differ by Δf_r, phase-locking at the comb tooth with index $\mu = 0$ and effective locking at $\mu = N$ thereby setting up the Vernier spectrometer. Tunable laser and chemical absorption lines (grey) can be measured with high precision. (**b**) Experimental setup. AOM: acousto-optic modulator; CIRC: circulator; PD: photodetector. Small red circles are polarization controllers. Inset: scanning electron microscope image of a silica resonator. (**c**) Optical spectra of counter-propagating solitons. Pumps are filtered and denoted by dashed lines. (**d**) Typical measured spectrum of V_1V_2 used to determine order n. For this spectrum: $\Delta f_{n1} - \Delta f_{n2}$ = 2.8052 MHz and Δf_r = 52 kHz giving n = 54. (**e**) The spectrograph of the dual soliton interferogram (pseudo color). Line spacing gives Δf_r = 52 kHz. White squares correspond to the index n = 54 in panel **c**. (**f**) Measured wavelength of an external cavity diode laser operated in steady state. (**g**) Residual deviations between ECDL laser frequency measurement as given by the MSS and a wavemeter. Error bars give the systematic uncertainty as limited by the reference laser in panel **b**.

generated in a high-Q silica microresonator with 3 mm diameter (22 GHz soliton repetition rate) [86]. Details on the soliton generation process can be found elsewhere [38, 91, 110]. Typical optical spectra of cw and ccw solitons span the telecommunication C-band (Figure 6.1(**c**)).

Operation principle

The spectrometer operates as follows. A test laser frequency f_L is measured using either of the following expressions: $f_L = nf_{r1,2} + \Delta f_{n1,2} + f_0$ where n is the comb order nearest to the laser frequency, $f_{r1,2}$ are the comb repetition rates, $\Delta f_{n1,2}$ are the heterodyne beat frequencies of the test laser with the two frequency comb teeth at order $\mu = n$, and f_0 is the frequency at $\mu = 0$. $f_{r1,2}$ and $\Delta f_{n1,2}$ are measured by co-detection of the combs and the test laser to produce the electrical signals $V_{1,2}$ in Fig. 6.1(**b**). Fast Fourier transform (FFT) of V_1V_2 gives the spectral line at $n\Delta f_r$ (Fig. 6.1(**d**)) using the correlation method [131] and, in turn, the order n. The correlation method can be understood as a calculation of the frequency difference $\Delta f_{n2} - \Delta f_{n1} = n\Delta f_r$ by formation of V_1V_2 followed by fast Fourier transform (FFT). The FFT spectrum of V_1V_2 gives the spectral line at $n\Delta f_r$ (Fig. 6.1(**d**)). To determine n, it requires $\Delta f_r = f_{r2} - f_{r1}$ which is measured by heterodyne of the solitons to produce electrical signal V_3. Figure 6.1(**e**) is a narrow frequency span of the FFT of V_3 and shows how the optical frequency Vernier is mapped into a stable radio-frequency grid with line spacing Δf_r. The order corresponding to the FFT of the V_1V_2 signal (Fig. 6.1(**d**) spectrum) is also indicated. These steps are performed automatically to provide a real time measurement of f_L relative to f_0. f_0 is determined by applying this procedure to the reference laser frequency f_{ref} (stabilized using an internal molecular reference). All of these data inputs are automatically processed in real time to measure f_L.

6.2 Measurement of a static laser

As a preliminary test, the frequency of an external-cavity-diode-laser is measured and compared against a wavemeter. Figures 6.1(**d**) and (**e**) ($n = 54$) are from this measurement. The real-time measured wavelength of the laser (Figure 6.1(**f**)) fluctuates within ±0.02 pm over a 5 ms time interval. The measurement was repeated from 1545 to 1560 nm with residual deviations less than 0.1 pm versus the wavemeter measurement (Figure 6.1(**g**)). These deviations are believed to be limited by the wavemeter resolution (±0.1 pm). The systematic uncertainty of absolute wavelength in the current setup is set by the reference laser to around ±4 MHz (±0.03 pm).

6.3 Measurement of dynamic lasers

The large, microwave-rate free-spectral range of the MSS enables tracking of lasers undergoing fast-chirping or discontinuous broadband tuning. Although correlation is performed with a time interval $T_W = 1/\Delta f_r$, the instantaneous frequency of

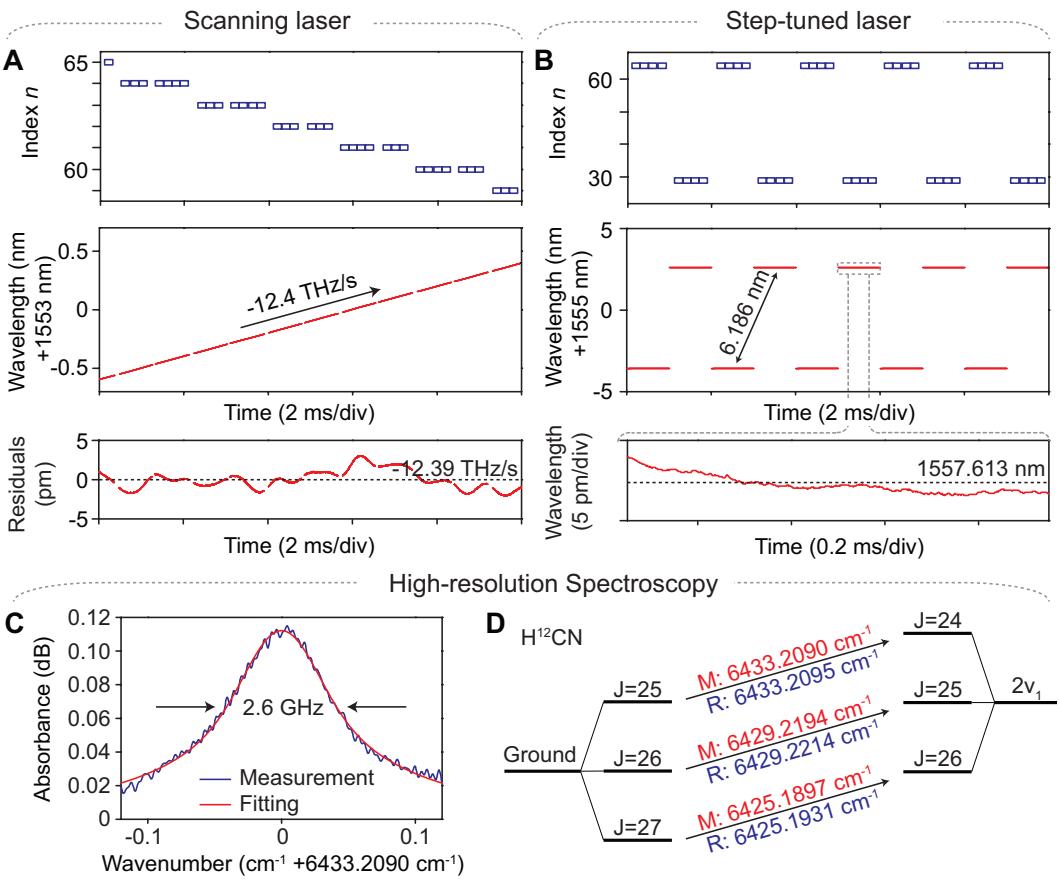

Figure 6.2: **Laser tuning and spectroscopy measurements.** (**a**) Measurement of a rapidly tuning laser showing index n (upper), instantaneous frequency (middle), and higher resolution plot of wavelength relative to average linear rate (lower), all plotted versus time. (**b**) Measurement of a broadband step-tuned laser as for laser in panel A. Lower panel is a zoom-in to illustrate resolution of the measurement. (**c**) Spectroscopy of $H^{12}C^{14}N$ gas. A vibronic level of $H^{12}C^{14}N$ gas at 5 Torr is resolved using the laser in panel A. (**d**) Energy level diagram showing transitions between ground state and $2\nu_1$ levels. The measured (reference) transition wavenumbers are noted in red (blue).

the laser relative to the combs can be acquired at a much faster rate set by the desired time-bandwidth-limited resolution. To avoid aliasing of the correlation measurement (i.e., to determine n uniquely), the amount of frequency-chirping should not exceed the repetition rate f_r within the measurement window T_W, which imposes a maximum resolvable chirping-rate of $f_r \times \Delta f_r$. This theoretical limit is 1 PHz/s for the MSS and represents a boost of 100× compared with previous Vernier spectrometers [131].

Measurement of rapid continuous-tuning of an external cavity diode laser is shown

in Figure 6.3(**a**). The correlation measurement evolves as the laser is tuned over multiple FSRs of the comb and thereby determines the index n as a function of time (Figure 6.3(**a**) upper panel). Measurement of the linear frequency chirp (-12.4 THz/s) as well as the frequency versus time at high resolution (by subtracting the average linear frequency ramp) are shown in the Figure 6.3(**a**) middle and lower panels, respectively. The discontinuities in the measurement are caused by electrical frequency dividers used to reduce the detected signal frequency for processing by a low-bandwidth oscilloscope. The dividers can be eliminated by using a faster oscilloscope. In Figure 6.3(**b**), measurement of broadband step tuning (mode hopping) of an integrated-ring-resonator tunable III-V/Silicon laser diode [133] is presented. Fast step tuning between 1551.427 nm and 1557.613 nm every 1 ms with the corresponding index n stepping between $n = 64$ and $n = 29$ is observed. The lower panel in Figure 6.3(**b**) gives a higher resolution zoom-in of one of the step regions. The data points in these measurements are acquired over 1μs so the resolution is approximately 1 MHz.

6.4 High-resolution spectroscopy

This combination of speed and precision is also useful for spectroscopic measurements of gas-phase chemicals using tunable, single-frequency lasers. To demonstrate, an absorption line of $H^{12}C^{14}N$ at 5 Torr is obtained by a scanning laser calibrated using the MSS (Figure 6.3(**c**)). The linewidth is around 2.6 GHz and the absorbance is as weak as 0.12 dB. Separate measurements on vibronic transitions between the ground state and $2\nu_1$ states were performed. The corresponding transition wavenumbers obtained by pseudo-Voigt fitting are in excellent agreement with the HITRAN database (Figure 6.3(**d**)) [134].

6.5 Measurement of multi-line spectra

To illustrate a measurement of more complex multi-line spectra, a fiber mode-locked laser (FMLL) is characterized (Figure 6.3(**a**)). The FMLL full spectrum (Figure 6.3(**b**)) was first bandpass filtered to prevent detector saturation. Also, the frequency extraction procedure is modified to enable unique identification of many frequencies. The reconstructed FMLL spectrum measured using the MSS is plotted in Figure 6.3(**c**). In an additional study of the FMLL, the MSS is used to measure 6 closely-spaced-in-frequency groups of lines located at various spectral locations spanning 2500 free-spectral-ranges of the mode-locked laser (Figure 6.3(**d**)). A linear fitting defined as $f_m = f_o + m f_{\text{rep}}$ is plotted for comparison by using the photodetector-

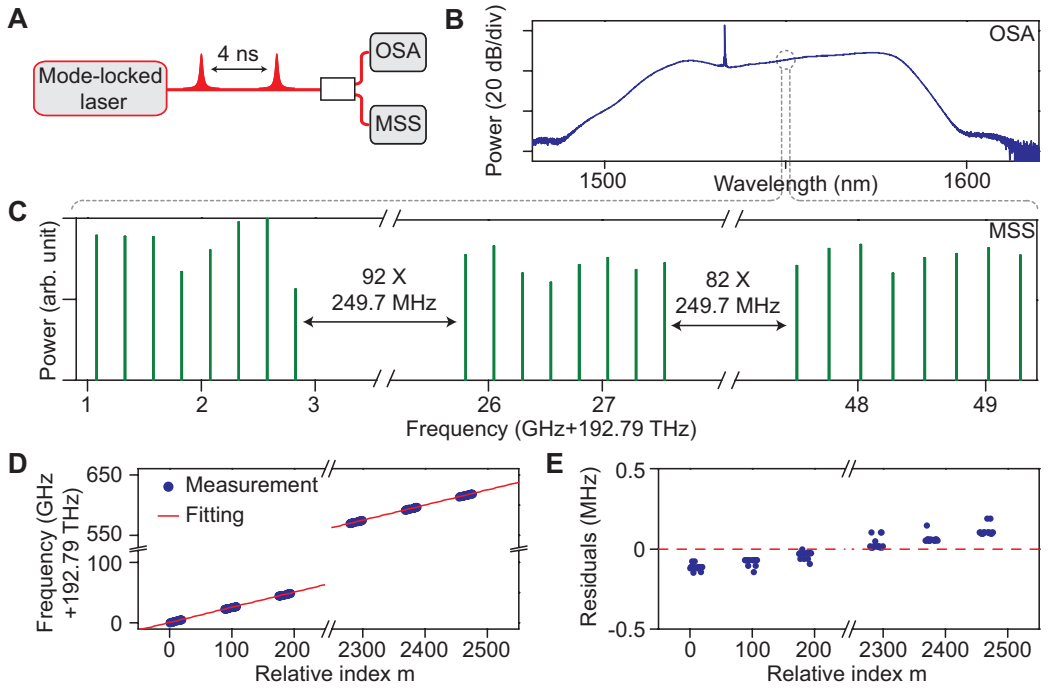

Figure 6.3: **Measurement of a fiber mode-locked laser.** (**a**) Pulse trains generated from a fiber mode-locked laser (FMLL) are sent into an optical spectral analyzer (OSA) and the MSS. (**b**) Optical spectrum of the FMLL measured by the OSA. (**c**) Optical spectrum of the FMLL measured using the MSS over a 60-GHz frequency range (indicated by dashed line). (**d**) Measured (blue) and fitted (red) FMLL mode frequencies versus index. The slope of the fitted line is set to 249.7 MHz, the measured FMLL repetition rate. (**e**) Residual MSS deviation between measurement and fitted value.

measured FMLL repetition rate $f_{\text{rep}} = 249.7$ MHz, where m and f_o represent the relative mode index and fitted offset frequency at $m = 0$, respectively. The residual deviation between the measurement and linear fitting is shown in Figure 6.3(**e**) and gives good agreement. The slight tilt observed in Figure 6.3(**e**) is believed to result from drifting of soliton repetition rates which were not monitored real-time. Also, variance of residuals within each group comes from the 300 kHz linewidth of each FMLL line. Drifting of the reference laser and FMLL carrier-envelope offset also contribute to the observed residuals across different measurements.

6.6 Signal processing

In this section, the algorithms used to extract the absolute frequencies of lasers are presented.

Single frequency laser

Through heterodyne of the test laser with the nearest comb teeth, the phase ψ of the test laser is related to the electrical signals $V_{1,2}$ by

$$V_{1,2} \propto \cos(\psi - 2\pi\nu_{n1,2}t), \tag{6.1}$$

where $\nu_{n1,2}$ represent the frequencies of nearest comb teeth and have order n. We also have $\nu_{n2} - \nu_{n1} = n\Delta f_r$ as a result of the CP soliton locking. A Hilbert transform is used to extract the time-dependent phase $\psi - 2\pi\nu_{n1,2}t$ from $V_{1,2}$ which thereby gives the heterodyne frequencies via

$$\Delta f_{n1,2} = \dot{\psi}/2\pi - \nu_{n1,2}. \tag{6.2}$$

Each data point of $\Delta f_{n1,2}$ is obtained by linear fitting of the phase over a specified time interval that sets the frequency resolution. Similarly, the heterodyne frequency between the reference laser and the soliton comb can be retrieved to determine the frequency f_0 (see discussion in main text).

The Fourier transform of the product V_1V_2 is given by

$$\begin{aligned}\widetilde{V_1V_2}(f) &\propto \int_0^{T_W} \frac{e^{i(\psi-2\pi\nu_{n1}t)} + e^{-i(\psi-2\pi\nu_{n1}t)}}{2} \frac{e^{i(\psi-2\pi\nu_{n2}t)} + e^{-i(\psi-2\pi\nu_{n2}t)}}{2} e^{-2\pi i f t}\mathrm{d}t \\ &\propto \delta(|f| - n\Delta f_r),\end{aligned} \tag{6.3}$$

where sum frequency terms in the integral are assumed to be filtered out and are therefore discarded. To accurately extract the above spectral signal, the acquisition time window T_W should be an integer multiple of $1/\Delta f_r$, which is also related to the pump frequency offset $\Delta\nu$ by $T_W = N_W N/\Delta\nu$ where N is the pump order and N_W is an integer. Moreover, the number of sampled points, which equals the product of oscilloscope sampling rate f_{samp} and T_W, should also be an integer (i.e., $f_{\mathrm{samp}}N_W N/\Delta\nu$ is an integer). Here, f_{samp} is usually set to 2.5 or 5 GHz/s and it is found that simple adjustment of $\Delta\nu$ is sufficient to satisfy this condition. As a result, it is not necessary to synchronize the oscilloscope to external sources. It is noted that this method is simpler than the asynchronous detection used in previous work [131].

On account of the limited bandwidth of the oscilloscope used in the work, it was necessary to apply electrical frequency division to the detected signals for processing by the oscilloscope. When frequency dividers are used (division ratio $r = 8$), the

divided electrical signals (indicated by superscript d) yield

$$V^{\mathrm{d}}_{1,2} \propto \cos((\psi - 2\pi\nu_{n1,2}t)/r). \tag{6.4}$$

As a result, the divided frequencies also satisfy $\Delta f^{\mathrm{d}}_{n1,2} = \Delta f_{n1,2}/r$ and the correlation between the divided signals scales proportionally by

$$\Delta f^{\mathrm{d}}_{n1} - \Delta f^{\mathrm{d}}_{n2} = n\Delta f_r/r. \tag{6.5}$$

Therefore the required resolution bandwidth to resolve the ambiguity n from the measured correlation is $\Delta f_r/r$ which increases the minimal acquisition time to $T^{\mathrm{d}}_W = rT_W$.

Multi-line spectra

The algorithm used here to extract a large number of frequencies simultaneously using the MSS is different from the previous single-frequency measurements. Rather than multiplying the signals V_1 and V_2 followed by Fast Fourier Transform (FFT) in order to determine the microcomb order, we directly FFT the signals V_1 and V_2 followed by filtering and then frequency correlation. This avoids the generation of ambiguities. To explain the approach, first consider an implementation similar to that reported in the main text. There, a fiber mode-locked laser (FMLL) comb with free-spectral-range (FSR) of about 250 MHz was optically filtered to create a narrower frequency range of FMLL laser lines extending over only a few microcomb teeth. The signals V_1 and V_2 upon FFT therefore produce a large set of frequencies representing the individual beats of each FMLL laser line (index m) with microcomb modes (index n). Figure 6.3(**a**) gives a narrow frequency span of a typical FFT generated this way for both the V_1 and V_2 signals. A zoom-in of one pair of V_1 and V_2 signals is provided in Figure 6.4(**b**) and a remarkably precise frequency separation between the beats (in view of the spectral breadth of each beat) can be determined by correlating the upper (blue) and lower (red) spectrum (see Figure 6.4(**c**)). This precision results from the underlying high relative frequency stability of the cw and ccw microcomb frequencies. As described in the main text, this frequency separation is a multiple of Δf_r and plot of the correlation versus the frequency separation (in units of Δf_r) is provided in Figure 6.4(**c**) where the peak of the correlation gives the index $n = 63$ for this pair of beat frequencies. Proceeding this way for each pair of peaks in Figure 6.4(**a**) allows determination of n from which the frequency of the corresponding FMLL line can be determined. It is interesting to note that in Figure 6.4(**a**), there are two sets of peaks that give n=63, 64, and 65.

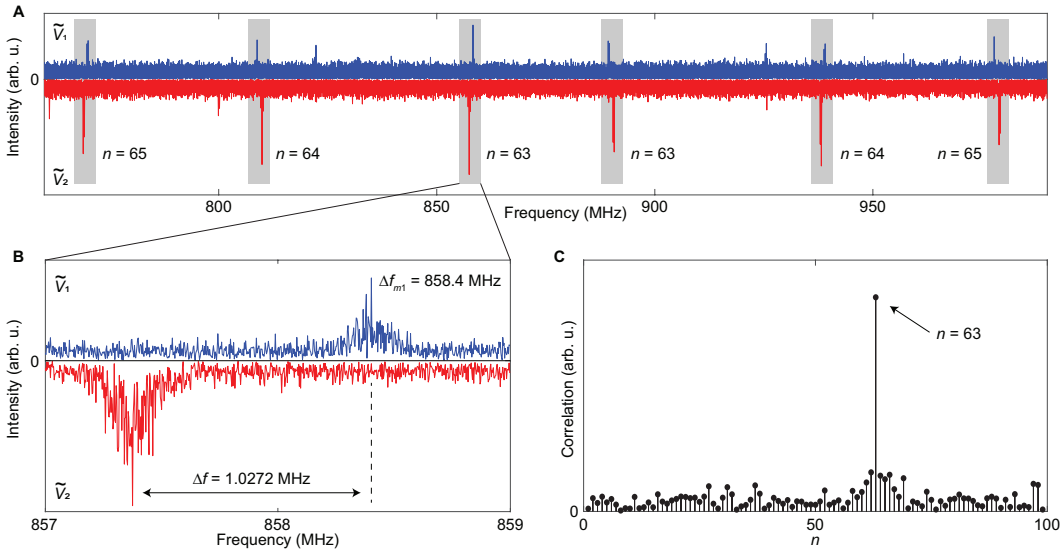

Figure 6.4: **Multi-frequency measurements.** (**a**) A section of $\tilde{V}_{1,2}$. Pairs of beatnotes coming from the same laser are highlighted and the derived n value is marked next to each pair of beatnotes. (**b**) Zoom-in on the highlighted region near 858 MHz in (**a**). Two beatnotes are separated by 1.0272 MHz. (**c**) Cross-correlation of $\tilde{V}_1$ and $\tilde{V}_2$ is calculated for each n and the maximum can be found at $n = 63$.

These correspond to FMLL lines that are higher and lower in frequency relative to the microcomb modes with indices n=63, 64, and 65. The relative alignment of the blue and red peaks which switches sign for these sets of beat frequencies allows determination of which FMLL line is lower and higher in frequency relative to the microcomb teeth.

To provide more rigor to this explanation, the electrical signals consist of multiple beat components given by,

$$V_{1,2} = \sum_m V_{m1,2}, \quad V_{m1,2} \propto \cos(\psi_m - 2\pi\nu_{\mu(m)1,2}t), \tag{6.6}$$

where ψ_m and $\nu_{\mu(m)1,2}$ represent the phase of the m-th FMLL mode and the frequencies of the microcomb order nearest to this FMLL mode, respectively, and where $\mu(m)$ denotes the comb order nearest the m-th FMLL mode. As described in the main text the frequencies $\nu_{\mu(m)1,2}$ are related to the repetition rate difference by $\nu_{\mu(m)2} - \nu_{\mu(m)1} = \mu(m)\Delta f_r$. The FFT of $V_{1,2}$ is denoted by $\tilde{V}_{1,2}$ and the correlation given in Figure 6.4(**c**) (and used to determine the comb order n of each spectral

component) is given by

$$\begin{aligned}
&\int_{\Delta f_{m1}-\kappa/2}^{\Delta f_{m1}+\kappa/2} \tilde{V}_1(f)\tilde{V}_2^*(f+n\Delta f_r)\mathrm{d}f \\
&\approx \int_{-\infty}^{\infty} \mathrm{d}f \int V_{m1}(t)e^{2\pi i f t}\mathrm{d}t \int V_{m2}(t')e^{-2\pi i(f+n\Delta f_r)t'}\mathrm{d}t' \\
&= \int V_{m1}(t)V_{m2}(t)e^{-2\pi i n\Delta f_r t}\mathrm{d}t \\
&\propto \int \frac{e^{i(\psi_m-2\pi\nu_{\mu 1}t)}+e^{-i(\psi_m-2\pi\nu_{\mu 1}t)}}{2}\frac{e^{i(\psi_m-2\pi\nu_{\mu 2}t)}+e^{-i(\psi_m-2\pi\nu_{\mu 2}t)}}{2}e^{-2\pi i n\Delta f_r t}\mathrm{d}t \\
&\propto \delta(\mu(m)-n),
\end{aligned} \tag{6.7}$$

where Δf_{m1} denotes the peak frequency of the beatnote, and κ is a predetermined range of integration to cover the linewidth of the beatnote (here $\kappa = 2$ MHz), and where sum frequency terms in the integral have been discarded. Therefore for each spectral component m, its associated microcomb order number $\mu(m)$ can be determined by varying n in the above correlation until it reaches maximum (see Figure 4.4(**c**)). The n value with the maximum correlation will be assigned to the peak as the tooth number $\mu(m)$ and then the absolute frequency can be recovered.

The limit of this process to accommodate more FMLL frequencies is much higher than that given by the filter bandwidth studied in this work. It is instead set by the spectral density of FMLL-microcomb beat lines that can be reasonably resolved within the microcomb FSR spectral span.

6.7 Conclusion

Our soliton spectrometer uses dual-locked counter-propagating soliton microcombs to provide high resolution frequency measurement of rapid continuously and step tuned lasers as well as complex multi-line spectra. In combination with a tunable laser, the spectrometer also enables precise measurement of absorption spectra, including random spectral access (as opposed to only continuous spectral scanning). Further optimization of this system could include generation of solitons from distinct mode families, thereby allowing tens-of-MHz repetition rate offset to be possible [135]. If such solitons can be dual-locked, the increased acquisition speed would enable measurement of chirping-rates much higher than PHz/s. Operation beyond the telecommunications band would also clearly be useful and could use internal [43] or on-chip spectral broadeners [136], and methods for generation of soliton microcombs into the visible band are possible [50]. Besides the performance enhancement realized with the soliton microcombs, the use of dual-locked counter-

propagating solitons provides a considerable technical simplification by eliminating the need for a second mutually phase-locked comb. Finally, chip integrable versions of the current device employing silicon nitride waveguides are possible [87]. These and other recently demonstrated compact and low-power soliton systems [137, 138] point towards the possibility of compact microresonator soliton spectrometers.

Chapter 7

INTEGRATED TURNKEY SOLITON MICROCOMBS

[1] Optical frequency combs have a wide range of applications in science and technology. An important development for miniature and integrated comb systems is the formation of dissipative Kerr solitons in coherently pumped high-quality-factor optical microresonators. Such soliton microcombs [41] have been applied to spectroscopy, the search for exoplanets [23, 24], optical frequency synthesis [140], time keeping [4] and other areas [41]. In addition, the recent integration of microresonators with lasers has revealed the viability of fully chip-based soliton microcombs. However, the operation of microcombs requires complex startup and feedback protocols that necessitate difficult-to-integrate optical and electrical components, and microcombs operating at rates that are compatible with electronic circuits—as is required in nearly all comb systems—have not yet been integrated with pump lasers because of their high power requirements. Here we experimentally demonstrate and theoretically describe a turnkey operation regime for soliton microcombs co-integrated with a pump laser. We show the appearance of an operating point at which solitons are immediately generated by turning the pump laser on, thereby eliminating the need for photonic and electronic control circuitry. These features are combined with high-quality-factor Si_3N_4 resonators to provide microcombs with repetition frequencies as low as 15 gigahertz that are fully integrated into an industry standard (butterfly) package, thereby offering compelling advantages for high-volume production.

7.1 Introduction

The integration of microcomb systems faces two considerable obstacles. First, complex tuning schemes and feedback loops are required for generation and stabilization of solitons [37, 39, 91]. These not only introduce redundant and power-hungry electronic components [137, 141], but also require optical isolation, a function that has so far been challenging to integrate at acceptable performance levels. Second, repetition frequencies that are both detectable and readily processed by integrated

[1]Work presented in this chapter has been published in [139] "Integrated turnkey soliton microcombs", *Nature* 582, 365-369 (2020). Boqiang Shen conceived the experiment, packaged the chip and performed the measurements. Boqiang Shen also analyzed the data and participated in the writing of the manuscript.

electronic circuits, such as complementary metal–oxide–semiconductor (CMOS) circuits, are essential for comb self-referencing, the key process that underlies many comb applications [1]. And while ultra-high-Q silica resonators [38, 87] and Damascene Si_3N_4 resonators [138] can attain these rates, their integration with pumps has not been possible. Here, we show that the nonlinear dynamics of an unisolated laser-microcomb system creates a new operating point from which the pump laser is simply turned-on to initiate the soliton mode-locking process. Theory and experimental demonstration of the existence and substantial benefits of this new turnkey operating point are demonstrated. Moreover, the resulting microcomb system features Q factor performance that enables electronic-circuit rate operation using an integrated pump.

7.2 Concept of turnkey soliton microcomb

In the experiment, integrated soliton microcombs whose fabrication and repetition rate (40 GHz down to 15 GHz) are compatible with CMOS circuits [142] are butt-coupled to a commercial distributed-feedback (DFB) laser via inverse tapers (Fig. 7.1(**a**)). The microresonators are fabricated using the photonic Damascene reflow process [138, 143] and feature Q factors exceeding 16 million (Fig. 7.1(**b**)), resulting in a low milliwatt-level parametric oscillation threshold, despite the larger required mode volumes of the GHz-rate microcombs. This enables chip-to-chip pumping of microcombs for the first time at these challenging repetition rates. Up to 30 mW of optical power is launched into the microresonator. Feedback from the resonator suppresses frequency noise by around 30 dB compared with that of a free-running DFB laser (Fig. 7.1(**c**)) so that the laser noise performance surpasses state-of-the-art monolithically integrated lasers [144] and table-top external-cavity-diode-lasers (ECDL). Given its compact footprint and the absence of control electronics, the pump-laser/microcomb chipset was mounted into a butterfly package (Fig. 7.1(**d**)) to facilitate measurements and also enable portability. This level of integration and packaging combined with turnkey operation makes this a completely functional device suitable for use in any system-level demonstration.

7.3 New turnkey operating point

In conventional pumping of microcombs, the laser is optically-isolated from the downstream optical path so as to prevent feedback-induced interference (Fig. 7.2(**a**)). And on account of strong high-Q-induced resonant build-up and the Kerr nonlinearity, the intracavity power as a function of pump-cavity detuning features bista-

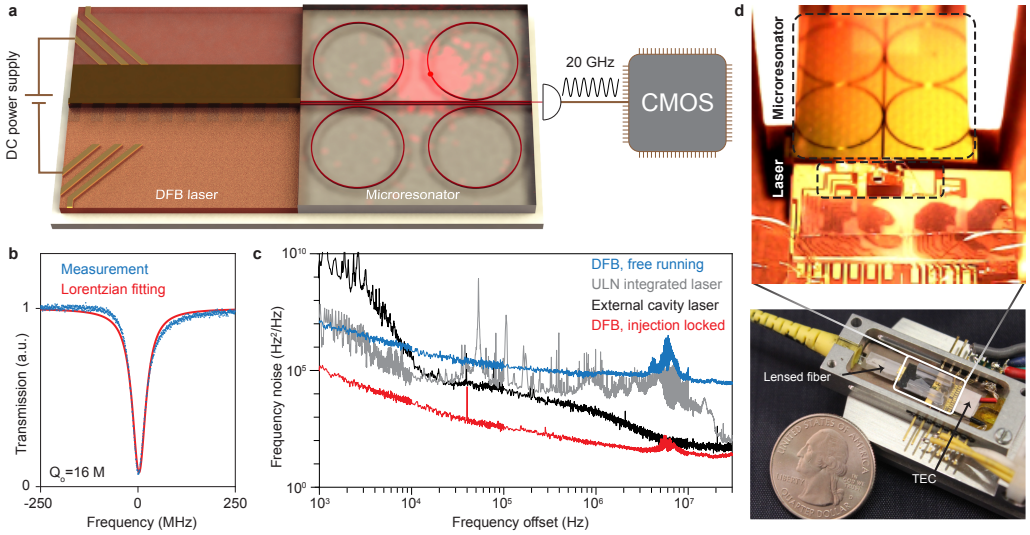

Figure 7.1: **Integrated soliton microcomb chip.** (**a**) Rendering of the soliton microcomb chip that is driven by a DC power source and produces soliton pulse signals at electronic-circuit rates. Four microcombs are integrated on one chip, but only one is used in these measurements. (**b**) Transmission signal when scanning the laser across a cavity resonance (blue). Lorentzian fitting (red) reveals 16 million intrinsic Q factor. (**c**) Frequency noise spectral densities (SDs) of the DFB laser when it is free running (blue) and feedback-locked to a high-Q Si_3N_4 microresonator (red). For comparison, the frequency noise SDs of ultra-low-noise integrated laser on silicon (grey) and a table-top external cavity diode laser (black) are also plotted. (**d**) Images of a pump/microcomb in a compact butterfly package.

bility. The resulting dynamics can be described using a phase diagram comprising continuous-wave (c.w.), modulation instability (MI) combs and soliton regimes that are accessed as the pump frequency is tuned across a cavity resonance. A typical plot (Fig. 7.2(**b**)) is made versus $\delta\omega$, the difference of cavity resonance and pump laser frequency (i.e., $\delta\omega > 0$ indicates red detuning of the pump frequency relative to the cavity frequency) [37]. The tuning through the MI regime functions to seed the formation of soliton pulses. On account of the thermal hysteresis [145] and the abrupt intracavity power discontinuity upon transition to the soliton regime (Fig. 7.2(**c**)), delicate tuning waveforms [37, 39] or active capturing techniques [91] are essential to compensate thermal transients, except in cases of materials featuring effectively negative thermo-optic response [48].

Now consider removing the optical isolation as shown in Fig. 7.2(**d**) so that backscatter feedback occurs from pumping a resonator mode. In prior work semiconductor laser locking to the resonator mode as well as laser line narrowing have been shown

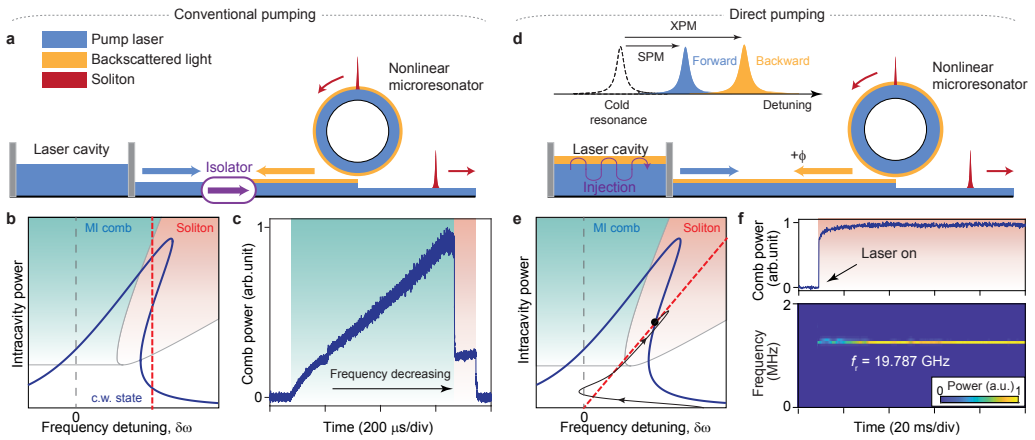

Figure 7.2: **The turnkey operating point.** (**a**) Conventional soliton microcomb operation using a tunable c.w. laser. An optical isolator blocks the back-scattered light from the microresonator. (**b**) Phase diagram, hysteresis curve, and dynamics of the microresonator pumped as shown in (**a**). The blue curve is the intracavity power as a function of cavity-pump frequency detuning. Laser tuning (dashed red line) accesses multiple equilibria. (**c**) Measured evolution of comb power pumped by an isolated, frequency-scanned ECDL. The step in the trace is a characteristic feature of soliton formation. (**d**) Turnkey soliton microcomb generation. Non-isolated operation allows back-scattered light to be injected into the pump laser cavity. Resonances are red-shifted due to self-phase modulation (SPM) and cross-phase modulation (XPM). (**e**) Phase diagram, hysteresis curve, and dynamics of pump/microresonator system. A modified laser tuning curve (dashed red line) intersects the intracavity power curve (blue) to establish a new operating point from which solitons form. The feedback phase ϕ is set to 0 in the plot. Simulated evolution upon turning-on of the laser at a red detuning outside the soliton regime but within the locking bandwidth is plotted (solid black curve). (**f**) Measured comb power (upper panel) and detected soliton repetition rate signal (lower panel) with laser turn-on indicated at 10 ms.

to result from backscattering of the intracavity optical field [146]. These attributes as well as mode selection when using a broadband pump have also been profitably applied to operate microcomb systems without isolation [137, 141, 147, 148]. However, these prior studies of feedback effects have considered the resonator to be linear so that the detuning between the feedback-locked laser and the cavity resonance is determined solely by the phase ϕ accumulated in the feedback path [149]. In contrast, here the nonlinear behavior of the microresonator is included and is shown to have a dramatic effect on the system operating point. The nonlinear behavior causes the resonances to be red-shifted by intensity-dependent self- and cross-phase modulation. As a result, the relationship between frequency detuning and intracavity

power of the pump mode P_0 can be shown (see section 7.5) to be approximately given by,

$$\frac{\delta\omega}{\kappa/2} = \tan\frac{\phi}{2} + \frac{3}{2}\frac{P_0}{P_{\text{th}}} \tag{7.1}$$

where κ is the power decay rate of the resonance and P_{th} is the parametric oscillation threshold for intracavity power. This dependence of detuning on intracavity power gives rise to a single operating point at the intersection of Eq. (7.1) and the hysteresis as shown in Fig. 7.2(**e**). Control of the feedback phase shifts the x-intercept of Eq. (7.1) and thereby adjusts the operating point.

In the section 7.5 it is shown that the system converges to this operating point once the laser frequency is within a locking bandwidth (estimated to be 5 GHz in the present case). As verified both numerically (Fig. 7.2(**e**)) and experimentally (Fig. 7.2(**f**)), this behavior enables soliton mode-locking by simple power-on of the pump laser (i.e., no triggering or complex tuning schemes). A simulated trajectory is shown in Fig. 7.2e wherein a laser is initially started to the red of the high-Q cavity resonant frequency and well outside its linewidth. The system is attracted towards the resonance through a process that at first resembles injection locking of the III-V laser. However, as the laser frequency moves towards the resonant frequency, the resonator power rises and the Kerr nonlinearity induces evolution towards the operating point. The system transiently exceeds the threshold for parametric oscillation and, as shown in section 7.5, Turing rolls form that ultimately evolve into the solitons as the system achieves steady state. An experimental trace of the comb power shows that a steady soliton power plateau is reached immediately after turn-on of the laser. And the stable soliton emission is further confirmed by monitoring the real-time evolution of the soliton repetition rate signal (Fig. 7.2(**f**)). Numerical simulation of this startup process is provided in section 7.5. The turnkey operation demonstrated here is automatic, such that the entire soliton initiation and stabilization is described and realized by the physical dynamics of laser self-injection locking in combination with the nonlinear resonator response. Consistent with this point, the system is observed to be highly robust with respect to temperature and environmental disturbances. Indeed, soliton generation without any external feedback control was possible for several hours in the laboratory.

7.4 Demonstration of turnkey soliton generation

Figure 7.3 shows the optical spectra of a single-soliton state with 40 GHz repetition rate and multi-soliton states with 20 GHz and 15 GHz repetition rates. The deviation

from the theoretical sech^2 spectral envelope is believed to result from a combination of mode crossing induced dispersion and the dispersion of the waveguide-resonator coupling strength. The pump laser at 1556 nm is attenuated at the output by a fiber-Bragg-grating notch filter in these spectra. The coherent nature of these soliton microcombs is confirmed by photodetection of the soliton pulse streams, and reveals high-contrast, single-tone electrical signals at the indicated repetition rates. Numerical simulations have confirmed the tendency of turnkey soliton states consisting of multiple solitons, which is a direct consequence of the high intracavity power and its associated MI gain dynamics (see section 7.5 for details). However, single-soliton operation is accessible for a certain combination of pump power and feedback phase.

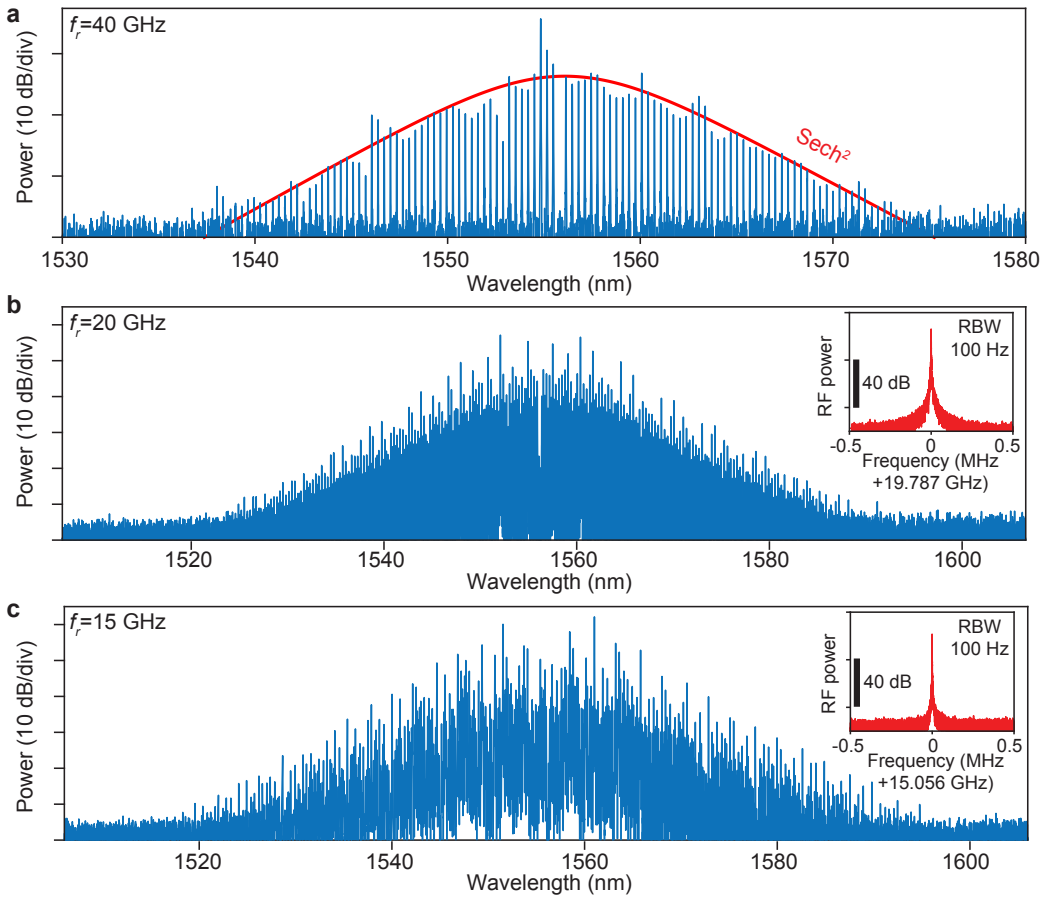

Figure 7.3: **Optical and electrical spectra of solitons.** (**a**) The optical spectrum of a single soliton state with repetition rate f_r = 40 GHz. The red curve shows a sech^2 fitting to the soliton spectral envelope. (**b**) (**c**) Optical spectra of multi-soliton states at 20 GHz and 15 GHz repetition rates. Insets: Electrical beatnotes showing the repetition rates.

To demonstrate the repeatable turnkey operation, the laser current is modulated to a preset current by a square wave to simulate the turn-on process. Soliton microcomb operation is reliably achieved as confirmed by monitoring soliton power and the single-tone beating signal (Fig. 7.4(**a**)). More insight into the nature of the turnkey operation is provided by the phase diagram near the equilibrium point for different feedback phase and pump power (Fig. 7.4(**b**)). The turnkey regime occurs above a threshold power within a specific range of feedback phases. Moreover, the regime recurs at 2π increments of feedback phase, which is verified experimentally (Fig. 7.4(**c**)). Consistent with the phase diagram, a binary-like behavior of turn-on success is observed as the feedback phase is varied. In the measurement the feedback phase was adjusted by control of the gap between the facets of the laser and the microcomb bus waveguide. A narrowing of the turn-on success window with an increased feedback phase is believed to result from the reduction of the pump power in the bus waveguide with increasing tuning gap (consistent with Fig. 7.4(**b**)).

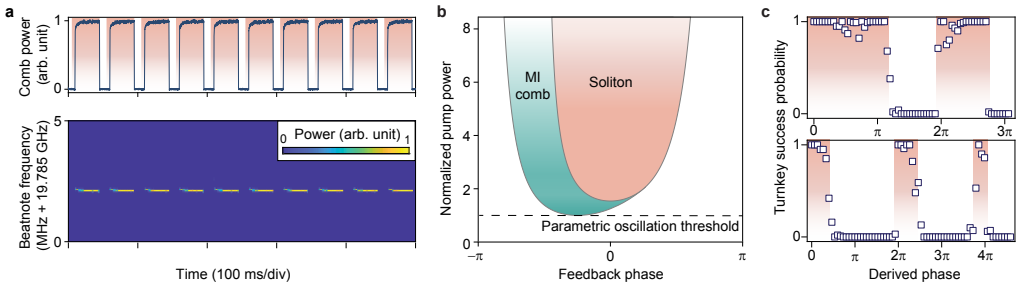

Figure 7.4: **Demonstration of turnkey soliton generation.** (**a**) 10 consecutive switching-on tests are shown. The upper panel gives the measured comb power versus time. The laser is switched on periodically as indicated by the shaded regions. The lower panel is a spectrogram of the soliton repetition rate signal measured during the switching process. (**b**) Phase diagram of the integrated soliton system with respect to feedback phase and pump power. The pump power is normalized to the parametric oscillation threshold. (**c**) Turnkey success probability versus relative feedback phase of 20 GHz (upper panel) and 15 GHz (lower panel) devices. Each data point is acquired from 100 switch-on attempts. See Methods for additional discussion.

7.5 Theory of turnkey soliton generation

Equations of motion

The injection locking system consists of three parts: the soliton optical field A_S, the backscattering field A_B, and the laser field A_L. The complete equations of motions are [117, 149]:

$$
\begin{aligned}
\frac{\partial A_{\mathrm{S}}}{\partial t} &= -\frac{\kappa}{2}A_{\mathrm{S}} - i\delta\omega A_{\mathrm{S}} + i\frac{D_2}{2}\frac{\partial^2 A_{\mathrm{S}}}{\partial\theta^2} + i\frac{\kappa}{2}\frac{|A_{\mathrm{S}}|^2 + 2|A_{\mathrm{B}}|^2}{E_{\mathrm{th}}}A_{\mathrm{S}} + i\beta\frac{\kappa}{2}A_{\mathrm{B}} - \sqrt{\kappa_{\mathrm{R}}\kappa_{\mathrm{L}}}e^{i\phi_{\mathrm{B}}}A_{\mathrm{L}} \\
\frac{dA_{\mathrm{B}}}{dt} &= -\frac{\kappa}{2}A_{\mathrm{B}} - i\delta\omega A_{\mathrm{B}} + i\frac{\kappa}{2}\frac{|A_{\mathrm{B}}|^2 + 2\int_0^{2\pi}|A_{\mathrm{S}}|^2 d\theta/(2\pi)}{E_{\mathrm{th}}}A_{\mathrm{B}} + i\beta\frac{\kappa}{2}\overline{A_{\mathrm{S}}} \\
\frac{dA_{\mathrm{L}}}{dt} &= i(\delta\omega_{\mathrm{L}} - \delta\omega)A_{\mathrm{L}} - \frac{\gamma}{2}A_{\mathrm{L}} + \frac{g(|A_{\mathrm{L}}|^2)}{2}(1 + i\alpha_g)A_{\mathrm{L}} - \sqrt{\kappa_{\mathrm{R}}\kappa_{\mathrm{L}}}e^{i\phi_{\mathrm{B}}}A_{\mathrm{B}}
\end{aligned}
\tag{7.2}
$$

where the field amplitudes are normalized so that $\int_0^{2\pi}|A_{\mathrm{S}}|^2 d\theta/(2\pi)$, $|A_{\mathrm{B}}|^2$ and $|A_{\mathrm{L}}|^2$ are the optical energies of their respective fields, t is the evolution time, θ is the resonator angular coordinate, κ is the resonator mode loss rate (assumed to be equal for A_{S} and A_{B}), $\delta\omega$ is the detuning of the cold-cavity resonance compared to injection-locked laser ($\delta\omega > 0$ indicates red detuning of the pump frequency relative to the cavity frequency), D_2 is the second-order dispersion parameter, E_{th} is the parametric oscillation threshold for intracavity energy, β is the dimensionless backscattering coefficient (normalized to $\kappa/2$), ϕ_{B} is the propagation phase delay between the resonator and the laser, κ_{R} and κ_{L} are the external coupling rates for the resonator and laser, respectively, $\delta\omega_{\mathrm{L}}$ is the detuning of the cold-cavity resonance relative to the cold laser frequency, γ is the laser mode loss rate, $g(|A_{\mathrm{L}}|^2) \equiv g_0/(1 + |A_{\mathrm{L}}|^2/|A_{\mathrm{L,sat}}|^2)$ is the intensity-dependent gain, g_0 is the gain coefficient, $|A_{\mathrm{L,sat}}|^2$ is the saturation energy level, and α_g is the amplitude-phase coupling factor. The average soliton field amplitude $\overline{A_{\mathrm{S}}} = \int_0^{2\pi} A_{\mathrm{S}} d\theta/(2\pi)$ is also the amplitude on the pumped mode, and by using $\overline{A_{\mathrm{S}}}$ in the equation for A_{B}, we have assumed that only the mode being pumped contributes significantly in the locking process, which can be justified if a single-frequency laser is used. We note that the equations are effectively referenced to the frequency of the injection-locked laser instead of the free-running laser, which will simplify the following discussions. The frequency difference between the cold laser and the injection-locked laser is given by $\delta\omega - \delta\omega_{\mathrm{L}}$.

We will introduce some other dimensionless quantities to facilitate the discussion. Define: normalized soliton field amplitude as $\psi = A_{\mathrm{S}}/\sqrt{E_{\mathrm{th}}}$, normalized total intracavity power as $P = \int_0^{2\pi}|A_{\mathrm{S}}|^2 d\theta/(2\pi E_{\mathrm{th}})$, normalized amplitude on the pump, backscattering and laser mode as $\rho = \overline{A_{\mathrm{S}}}/\sqrt{E_{\mathrm{th}}}$, $\rho_{\mathrm{B}} = A_{\mathrm{B}}/\sqrt{E_{\mathrm{th}}}$, $\rho_{\mathrm{L}} = A_{\mathrm{L}}/\sqrt{E_{\mathrm{th}}}$, respectively, normalized detuning of cavity as $\alpha = 2\delta\omega/\kappa$, and normalized evolution time as $\tau = \kappa t/2$. The equation for A_{S} and A_{B} can then be put into the dimensionless

form

$$\begin{aligned}\frac{\partial\psi}{\partial\tau} &= -(1+i\alpha)\psi + i\frac{D_2}{\kappa}\frac{\partial^2\psi}{\partial\theta^2} + i(|\psi|^2 + 2|\rho_\mathrm{B}|^2)\psi + i\beta\rho_\mathrm{B} - \frac{2\sqrt{\kappa_\mathrm{R}\kappa_\mathrm{L}}}{\kappa}e^{i\phi_\mathrm{B}}\rho_\mathrm{L} \\ \frac{d\rho_\mathrm{B}}{d\tau} &= -(1+i\alpha)\rho_\mathrm{B} + i(2P + |\rho_\mathrm{B}|^2)\rho_\mathrm{B} + i\beta\rho.\end{aligned} \tag{7.3}$$

The laser dynamics for A_L are split into amplitude and phase parts:

$$\begin{aligned}\frac{1}{|A_\mathrm{L}|}\frac{d|A_\mathrm{L}|}{dt} &= -\frac{\gamma}{2} + \frac{g(|A_\mathrm{L}|^2)}{2} - \mathrm{Re}\left[\sqrt{\kappa_\mathrm{R}\kappa_\mathrm{L}}e^{i\phi_\mathrm{B}}\frac{A_\mathrm{B}}{A_\mathrm{L}}\right] \\ \frac{d\phi_\mathrm{L}}{dt} &= \delta\omega_\mathrm{L} - \delta\omega + \frac{g(|A_\mathrm{L}|^2)}{2}\alpha_g - \mathrm{Im}\left[\sqrt{\kappa_\mathrm{R}\kappa_\mathrm{L}}e^{i\phi_\mathrm{B}}\frac{A_\mathrm{B}}{A_\mathrm{L}}\right]\end{aligned}$$

where $\mathrm{Re}[\cdot]$ and $\mathrm{Im}[\cdot]$ are the real and imaginary part functions, respectively. The laser power without backscatter feedback $|A_\mathrm{L}^{(0)}|$ satisfies $g(|A_\mathrm{L}^{(0)}|^2) = \gamma$. Expanding the gain around this point gives

$$\frac{1}{|A_\mathrm{L}|}\frac{d|A_\mathrm{L}|}{dt} = -g'\frac{|A_\mathrm{L}|^2 - |A_\mathrm{L}^{(0)}|^2}{|A_\mathrm{L,sat}|^2} - \mathrm{Re}\left[\sqrt{\kappa_\mathrm{R}\kappa_\mathrm{L}}e^{i\phi_\mathrm{B}}\frac{A_\mathrm{B}}{A_\mathrm{L}}\right]$$

where $g' = g_0/(1 + |A_\mathrm{L}^{(0)}|^2/|A_\mathrm{L,sat}|^2)^2$ is the gain derivative that represents the relaxation rate of the gain dynamics. Typical values for g' are on the order of several GHz for III-V semiconductor lasers, which is much faster compared to the resonator dynamics. Accordingly, the laser amplitude can be adiabatically eliminated (i.e., assume $d|A_\mathrm{L}|/dt = 0$) so that the laser power adiabatically tracks the feedback. The gain can be solved as,

$$\frac{g(|A_\mathrm{L}|^2)}{2} = \frac{\gamma}{2} + \mathrm{Re}\left[\sqrt{\kappa_\mathrm{R}\kappa_\mathrm{L}}e^{i\phi_\mathrm{B}}\frac{A_\mathrm{B}}{A_\mathrm{L}}\right]$$

which, under the assumption of fast relaxation rates, becomes independent of the specific details of gain. Substituting this equation into the phase equation and normalizing results in an Adler-like equation:

$$\frac{d\phi_\mathrm{L}}{d\tau} = \alpha_\mathrm{L} - \alpha - \mathrm{Im}\left[\frac{2\sqrt{\kappa_\mathrm{R}\kappa_\mathrm{L}}}{\kappa}(1 - i\alpha_g)e^{i\phi_\mathrm{B}}\frac{\rho_\mathrm{B}}{\rho_\mathrm{L}}\right] \tag{7.4}$$

where $\alpha_\mathrm{L} = (2\delta\omega_\mathrm{L} + \alpha_g\gamma)/\kappa$ is the normalized detuning of the cold-cavity resonance compared to the free-running hot laser.

To simplify the equations further, we also consider the following approximation for the propagation phase ϕ_B, which depends on the precise frequency of the locked laser

and material dispersion. We assume that the feedback length is short ($L \ll c/(n\kappa)$, where c is the speed of light in vacuum and n is the refractive index of the material) so that ϕ_B can be treated as constant. This approximation is equivalent to assuming that the FSR of a cavity equal in length to the feedback path is much larger than the linewidth of the high-Q resonator. By defining a pump phase variable $z = -e^{i\phi_\mathrm{B}} e^{i\phi_\mathrm{L}}$, the equations can be written as

$$\begin{aligned}
\frac{\partial \psi}{\partial \tau} &= -(1+i\alpha)\psi + i\frac{D_2}{\kappa}\frac{\partial^2 \psi}{\partial \theta^2} + i(|\psi|^2 + 2|\rho_\mathrm{B}|^2)\psi + i\beta\rho_\mathrm{B} + zF \\
\frac{d\rho_\mathrm{B}}{d\tau} &= -(1+i\alpha - 2iP - i|\rho_\mathrm{B}|^2)\rho_\mathrm{B} + i\beta\rho \\
\frac{1}{iz}\frac{dz}{d\tau} &= \alpha_\mathrm{L} - \alpha + K\mathrm{Im}\left[e^{i\phi}\frac{\rho_\mathrm{B}}{i\beta z F}\right], \quad |z| = 1
\end{aligned} \tag{7.5}$$

where we defined: the normalized pump,

$$F = \frac{2\sqrt{\kappa_\mathrm{R}\kappa_\mathrm{L}}}{\kappa}|\rho_\mathrm{L}| \tag{7.6}$$

the locking bandwidth,

$$K = \frac{4\kappa_\mathrm{R}\kappa_\mathrm{L}}{\kappa^2}|\beta|\sqrt{1+\alpha_g^2} \tag{7.7}$$

and the feedback phase,

$$\phi = 2\phi_\mathrm{B} - \arctan(\alpha_g) + \mathrm{Arg}[\beta] + \frac{\pi}{2} \tag{7.8}$$

where $\mathrm{Arg}[\cdot]$ is the argument function. The feedback phase ϕ contains phase contributions from the propagation length, the amplitude-phase coupling, the backscattering, as well as an extra $\pi/2$ added to the definition of ϕ such that the mode is locked to the center at $\phi = 0$ (as discussed below).

We note that the feedback fields considered in Eq. (7.5) come entirely from inside the resonator. In experiments, defects and facets of the coupling waveguide can also induce reflections. However, these are neglected in the injection locking dynamics by the following arguments. Multiple reflection sources can be incorporated into Eq. (7.5) by adding a feedback term corresponding to each source. However, the cumulative effect of such reflections will be to produce a wavelength dependence that is weak compared to the resonator mode, which is spectrally very narrow on account of its high optical Q. Such a weak wavelength dependence means that these fields do not contribute to the locking (i.e., a constant term is added to the phasor equation in Eq. (7.5) , which can then be absorbed into the free-running laser

frequency). As a specific illustration of this idea, consider that the facet reflections at the end of the waveguide form a kind of Fabry-Perot resonator. However, the Q of its resonances will be quite low and, accordingly, the linewidth will be of order the FSR associated with the waveguide length. Moreover, this FSR is also comparable in scale to the FSR of the high-Q resonator, the resonances of which are many orders narrower than the resonator FSR. As a result, any wavelength dependence introduced by reflections in the waveguide will be spectrally slow in comparison to those introduced by the resonator.

For stationary solutions (e.g. a stable soliton), when backscattering is weak ($\beta \ll 1$) so that nonlinearities caused by $|\rho_{\mathrm{B}}|^2$ in Eq. (7.3) are negligible in comparison to the soliton driven nonlinear terms, ρ_{B} can be found as

$$\rho_{\mathrm{B}} = \frac{i\beta\rho}{1 + i(\alpha - 2P)} \tag{7.9}$$

and the laser phasor equation reduces to an algebraic equation for the detuning α,

$$\alpha = \alpha_{\mathrm{L}} + K\mathrm{Im}\left[e^{i\phi}\frac{1}{1 + i(\alpha - 2P)}\frac{\rho}{zF}\right]. \tag{7.10}$$

Finally, neglecting the small coupled amplitude from ρ_{B} to ψ, the equation for the soliton field reads

$$-(1 + i\alpha)\psi + i\frac{D_2}{\kappa}\frac{\partial^2\psi}{\partial\theta^2} + i|\psi|^2\psi + zF = 0. \tag{7.11}$$

We have therefore recovered a conventional Lugiato-Lefever equation, with an additional equation that describes the detuning determined by injection locking. This shows that the spectral properties of the injection-locked solitons are not much different from a conventional soliton. The main difference is the comb formation dynamics.

Continuous-wave excitation and equilibrium of locking

It is known that combs and solitons will emerge from a continuous-wave (CW) background when the input power exceeds the parametric oscillation threshold ($|\rho| > 1$), and it is desirable to first study the CW excitation of the system by setting $D_2 = 0$. In this case, the Lugiato-Lefever partial differential equation reduces to an ordinary differential equation with $\psi = \rho$ and $P = |\rho|^2$. The steady state solution can be found from

$$zF = [1 + i(\alpha - |\rho|^2)]\rho \tag{7.12}$$

and the locking equilibrium reduces to

$$\alpha = \alpha_{\mathrm{L}} + K\mathrm{Im}\left[e^{i\phi}\frac{1}{1+i(\alpha-2P)}\frac{1}{1+i(\alpha-P)}\right] = \alpha_{\mathrm{L}} + K\chi(P,\alpha,\phi) \tag{7.13}$$

where we have defined the CW locking response function:

$$\chi(P,\alpha,\phi) = \frac{(3P-2\alpha)\cos\phi + (1-2P^2+3P\alpha-\alpha^2)\sin\phi}{[1+(\alpha-P)^2][1+(\alpha-2P)^2].} \tag{7.14}$$

To obtain analytical results, we will also make the approximation of infinite locking bandwidth limit (i.e. $K \to \infty$), which makes the detuning independent of the free-running laser frequency. The locking condition is then equivalent to setting the locking response function to zero:

$$(3P-2\alpha)\cos\phi + (1-2P^2+3P\alpha-\alpha^2)\sin\phi = 0 \tag{7.15}$$

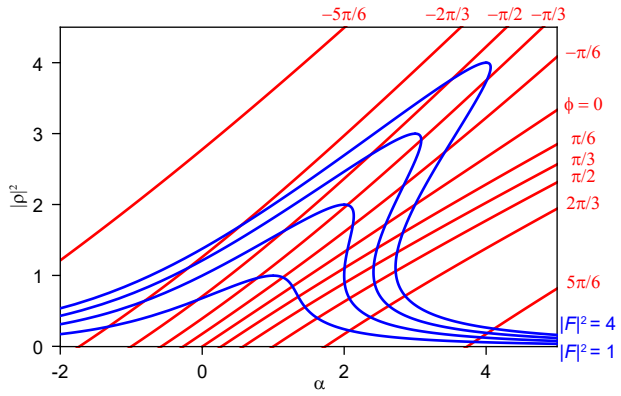

Figure 7.5: **Continuous-wave states of the injection-locked nonlinear resonator.** Horizontal axis is the normalized detuning α, and vertical axis is the normalized optical energy on the pump mode $|\rho|^2$. Resonator characteristics are shown as the blue curves, with $|F|^2 = 1$ (lower) to 4 (upper). Laser locking characteristics are shown as the red curves, with $\phi = -5\pi/6$ (upper left) to $5\pi/6$ (lower right).

Fig. 7.5 shows a plot for Eq. (7.12) with different pumping powers $|F|^2$ and Eq. (7.15) with different feedback phases ϕ. The intersecting point of the two curves gives the CW steady state of the cavity. Note that there are two solutions to the quadratic equation Eq. (7.15). Only the solution branch that satisfies $\partial\chi/\partial\alpha < 0$ is plotted, which are the stable locking solutions (stable in the sense of CW excitations; the instability arising from modulations are considered below). The opposite case $\partial\chi/\partial\alpha > 0$ drives the frequency away from the equilibrium.

When a resonator is pumped conventionally, the intracavity power P will approach its equilibrium given by Eq. (7.12). In the case of feedback-locked pumping, such power changes will also have an effect on the locking response function χ, pulling the detuning to the new locking equilibrium as well (Fig. 7.2(**b**) and 7.2(**e**)). A special case is $\phi = 0$, where the locking equilibrium can be simply described as

$$\alpha = \frac{3}{2}P \tag{7.16}$$

i.e. the detuning is pulled away from the cold cavity resonance, and the effect is exactly $3/2$ times what is expected from the self phase modulation. This is an averaged effect of the self phase modulation on the soliton mode and the cross phase modulation of the backscattered mode from the soliton mode. More generally, the detuning can be solved in terms of P as

$$\alpha = \frac{3}{2}P - \cot\phi + \frac{\sqrt{4 + P^2\sin^2\phi}}{2\sin\phi} \tag{7.17}$$

where again only the solution satisfying $\partial\chi/\partial\alpha < 0$ is given. Neglecting the higher-order $P^2\sin^2\phi$ term inside the square root results in a lowest order approximation:

$$\alpha = \tan\frac{\phi}{2} + \frac{3}{2}P \tag{7.18}$$

which splits into two additive contributions: one from the feedback phase and the other from the averaged nonlinear shift. This is Eq. (7.1) when written using dimensional quantities. We note that Eq. (7.1) uses power normalized to threshold power, while in the above analysis we used energy normalized to threshold energy. The intracavity power and energy only differ by a factor of round-trip time, and the normalized quantity is essentially the same.

Soliton formation

When the dispersion term is considered, the CW solution is no longer stable, which leads to the formation of modulational instability (MI) combs. These combs will evolve into solitons if the CW state is also inside the multistability region of the resonator dynamics. By adjusting the pump power $|F|^2$ and feedback phase ϕ, we can change the operating point of the cavity, and map the possible comb states to a phase diagram with $|F|^2$ and ϕ as parameters (Fig. 7.4(**b**)). It should be noted that as soon as combs start to form inside the resonator, the CW results after Eq. (7.12) becomes invalid (i.e., due to power appearing in the sidebands, we have $P > |\rho|^2$ when combs are formed instead of $P = |\rho|^2$ in the CW case), and such

comb formation will slightly shift the operating point of the system. However, the CW results still indicate whether and how such combs can be started. Contrary to conventional pumping phase diagrams (with $|F|^2$ and α as parameters), where soliton existence regions only imply the possible formation of solitons due to multistability, the soliton existence region here guarantees the generation of solitons as the system bypasses the chaotic comb region before the onset of MI.

Numerical simulations

We have also performed numerical simulations to verify the above analyses (Fig. 7.6). The simulation numerically integrates Eq. 7.5 with a split-step Fourier method. Noise equivalent to about one-half photon per mode is injected into ψ to provide seeding for comb generation. Parameters common to all simulation cases are $D_2/\kappa = 0.015$ and $|\beta| = 0.5$, while others are varied across different cases and can be found in the caption of 7.6. As an aside, the magnitude of β was estimated from the resonant backscatter reflectivity. The resonant reflection (measured to be in the range of 4% - 20%) was measured by detecting the reflected optical power from the resonator while scanning a laser across the resonances. In the first case (Fig. 7.6(**a**)), conventional soliton generation by sweeping the laser frequency is presented, showing the dynamics of a random noisy comb waveform collapsing into soliton pulses. This is in contrast to the turnkey soliton generation in the second case (Fig. 7.6(**b**)), where solitons directly "grow up" from ripples in the background. Such ripples are generated by MI in those sections of the resonator with local intracavity power above the threshold. Each peak in the ripples corresponds to one soliton if collisions and other events are not considered. The process of growing solitons out of the background will continue until there is no space for new solitons or when the background falls below the MI threshold, and such dynamics explain the tendency of the turnkey soliton state to consist of multiple solitons. By carefully tuning the phase and controlling the MI gain, it is still possible to obtain a turnkey single soliton state, as shown in the third case (Fig. 7.6(**c**)).

7.6 Additional measurements

Different types of microcombs in the injection locking system

There are several interesting solutions other than stable solitons that can be derived from the regular Lugiato-Lefever equation (LLE) [117]. One is the breather soliton, which is the type of soliton whose shape oscillates in time. Another example is the chaotic comb, which corresponds to the unstable Turing patterns or soliton state as

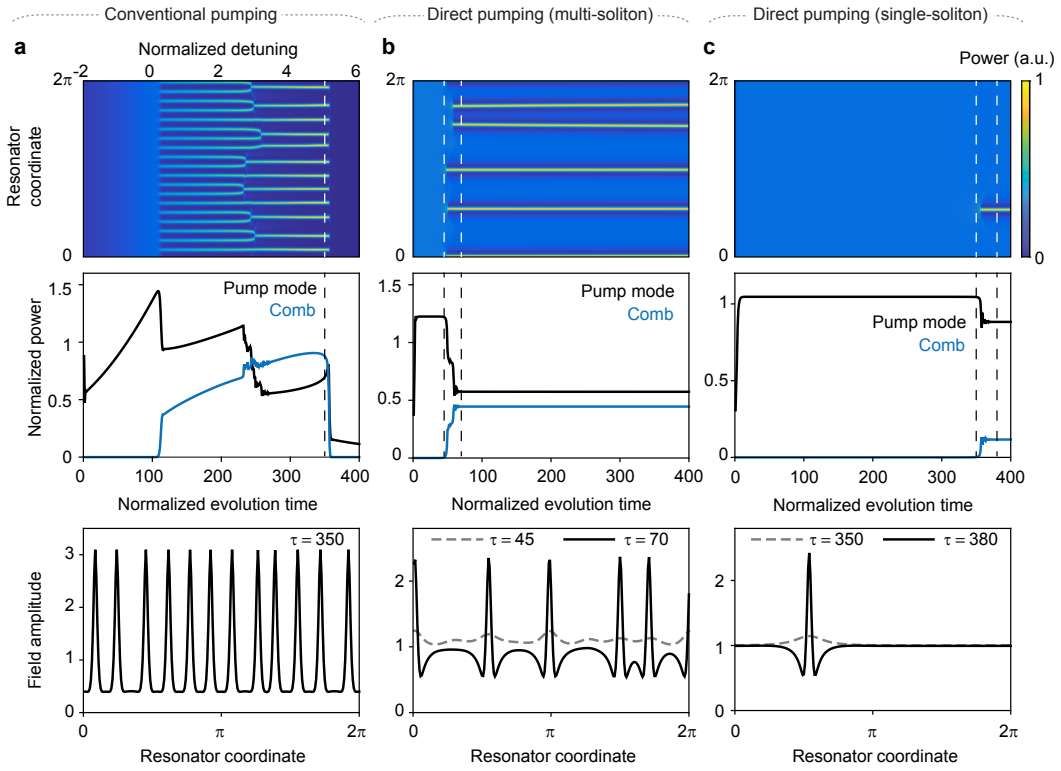

Figure 7.6: **Numerical simulations of turnkey soliton generation.** (**a**) Conventional solitons are generated by sweeping the laser frequency. Parameters are $K = 0$ (no feedback) and $|F|^2 = 4$. The normalized laser frequency is swept from $\alpha_L = -2$ to $\alpha_L = 6$ within a normalized time interval of 400. Upper panel: soliton field power distribution as a function of evolution time and coordinates. Middle panel: dynamics of the pump mode power (black) and comb power (blue). Lower panel: a snapshot of the soliton field at evolution time $\tau = 350$ ($\alpha_L = 5$), also marked as a white dashed line in the upper panel and a black dashed line in the middle panel. (**b**) Multiple solitons are generated under conditions of nonlinear feedback. Parameters are $K = 15$, $\phi = 0.15\pi$, $|F|^2 = 3$ and $\alpha_L = 5$. Upper and middle panels are the same as in (**a**). Lower panel: snapshots of the soliton field at evolution time $\tau = 45$ (gray dashed line) and $\tau = 70$ (black solid line), also marked as white dashed lines in the upper panel and black dashed lines in the middle panel. (**c**) A single soliton is generated under conditions of nonlinear feedback. Parameters are $K = 15$, $\phi = 0.3\pi$, $|F|^2 = 3$ and $\alpha_L = 5$. Upper and middle panels are the same as in (**a**). Lower panel: snapshots of the soliton field at evolution time $\tau = 350$ (gray dashed line) and $\tau = 380$ (black solid line), also marked as white dashed lines in the upper panel and black dashed lines in the middle panel.

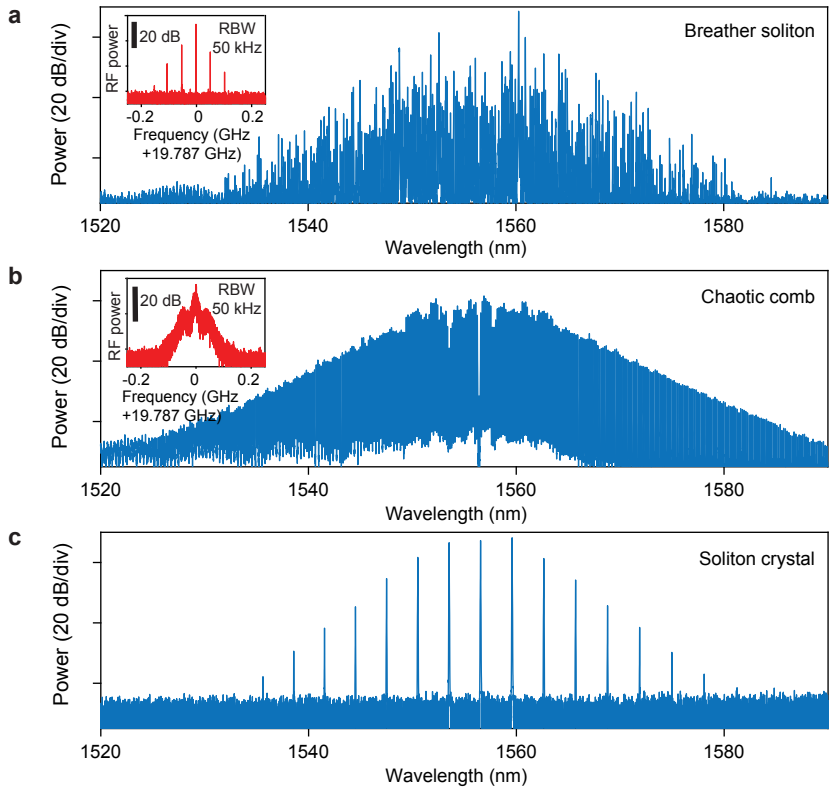

Figure 7.7: **Optical and electrical spectra of different microcomb types.** (**a**)(**b**) Optical spectra of breather solitons and a chaotic comb. Inset: Electrical beatnote signals. (**c**) Optical spectrum of a soliton crystal state.

the pump power is increased. In addition, solitons can be self-organized and form an equidistant pulse train in the microresonator, which is called a soliton crystal.

It is also possible to operate our system in different types of microcomb states under certain feedback phase and laser driving frequency. Fig. 7.7 shows the experimental spectra of breather solitons, a chaotic comb, and a soliton crystal state, respectively. The turnkey generation of the chaotic comb is further shown in Fig. 7.7(**a**). The broad and noisy RF spectrum indicates that it is not mode-locked.

Tuning of turnkey soliton microcomb system

To further explore the performance of the turnkey soliton microcomb system, the frequency of the pump laser is driven by a linear current scan (Fig. 7.8(**b**),(**c**)). The scan speed of the driving frequency is around 0.36 GHz/ms, estimated from the wavelength-current response when the laser is free running. When the laser is scanned across the resonance, feedback locking occurs and pulls the pump laser frequency towards the resonance until the driving frequency is out of the locking

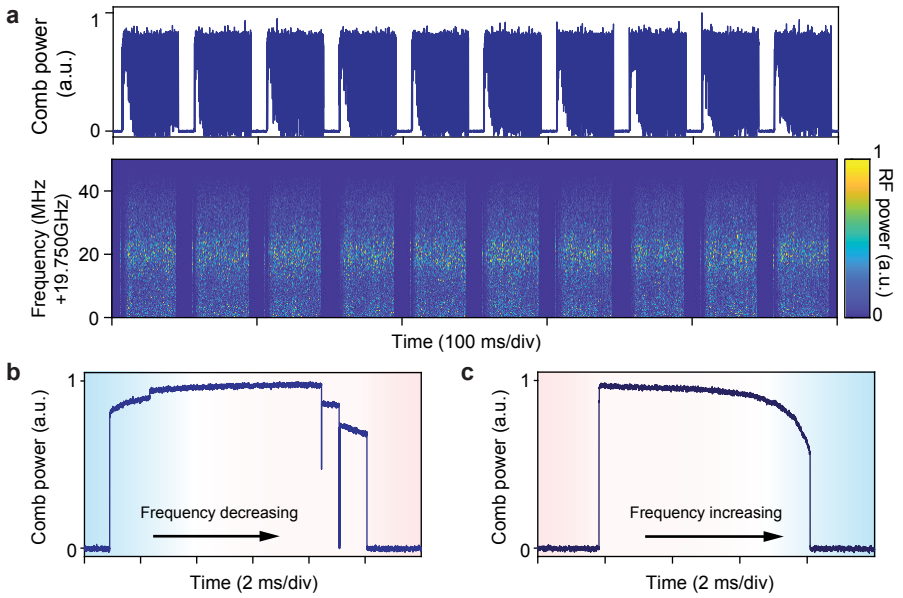

Figure 7.8: **Tuning of turnkey soliton microcomb system.** (**a**) Turnkey generation of a chaotic comb. Upper panel: Comb power evolution. Lower panel: Spectrograph of RF beatnote power. (**b**)(**c**) Comb power evolution when the pump laser frequency is driven from blue to red (**b**) and red to blue (**c**).

band. As shown in Fig. 7.8(**b**), the power steps indicate that soliton states with different soliton numbers can be accessed as we tune the driving current. It is worth noting that the soliton microcombs can be powered-on when the laser is scanned from red-detuned side (Fig. 7.8**c**), which seldom happens under conventional pumping, except in cases of an effectively negative thermo-optic response system [48]. The comb evolution during laser scanning is a useful tool to assess the robustness of the turnkey soliton generation.

7.7 Conclusion

Besides the physical significance and practical impact of the new operating point, our demonstration of a turnkey operating regime is an important simplification of soliton microcomb systems. Moreover, the application of this method in an integrated CMOS-compatible system represents a milestone towards mass production of optical frequency combs. The butterfly packaged devices will benefit several comb applications including miniaturized frequency synthesizers [9] and optical clocks [4]. In these applications, their CMOS rates, besides enabling integration of electrical control and processing functions, provide for simple detection and processing of the comb pulses (i.e., without the need for millimeter-wave-rate frequency mixers).

Moreover, the recent demonstration of low power comb formation in III-V microresonators [49] suggests that monolithic integration of pumps and soliton microcombs is feasible using the methods developed here. A phase section could be included therein or in advanced versions of the current approach to electronically control the feedback phase. The ability to create a complete system including pump laser without optical isolation is also significant. Even in cases where solitons are pumped using amplification such as with laser cavity solitons [150], full integration would require difficult-to-integrate optical isolators. It is also important to note that the current turnkey approach is a soliton forming comb while other recent work reports on non-soliton Kerr combs [151]. Finally, due to its simplicity, this approach could be applied in other integrated high-Q microresonator platforms [47, 48, 87] to attain soliton microcombs across a wide range of wavelengths.

Chapter 8

DARK SOLITON MICROCOMBS IN CMOS-READY ULTRA-HIGH-Q MICRORESONATORS

[1]Driven by narrow-linewidth bench-top lasers, coherent optical systems spanning optical communications, metrology, and sensing provide unrivalled performance. To transfer these capabilities from the laboratory to the real world, a key missing ingredient is a mass-produced integrated laser with superior coherence. Here, we bridge conventional semiconductor lasers and coherent optical systems using CMOS-foundry-fabricated microresonators with record high Q factor over 260 million and finesse over 42,000. Five orders-of-magnitude noise reduction in the pump laser is demonstrated, enabling frequency noise of 0.2 Hz^2 Hz^{-1} to be achieved in an electrically-pumped integrated laser, with corresponding short-term linewidth of 1.2 Hz. Moreover, the same configuration is shown to relieve dispersion requirements for microcomb generation that have handicapped certain nonlinear platforms. The simultaneous realization of record-high Q factor, highly coherent lasers, and frequency combs using foundry-based technologies paves the way for volume manufacturing of a wide range of coherent optical systems.

8.1 Introduction

The benefits of high coherence lasers extend to many applications. Hertz-level linewidth is required to interrogate and manipulate atomic transitions with long coherence times, which form the basis of optical atomic clocks [4, 73]. Furthermore, linewidth directly impacts performance in optical sensing and signal generation applications, such as laser gyroscopes [31, 153], light detection and ranging (LIDAR) systems [16, 17], spectroscopy [11], optical frequency synthesis [9], microwave photonics [27, 143, 147, 154, 155], and coherent optical communications[156, 157]. In considering the future transfer of such high coherence technologies to a mass manufacturable form, semiconductor laser sources represent the most compelling choice. They are directly electrically pumped, wafer-scale manufacturable and capable of complex integration with other photonic devices. Indeed, their considerable advan-

[1]Work presented in this chapter has been published in [152] "Hertz-linewidth semiconductor lasers using CMOS-ready ultra-high-Q microresonators", *Nature Photonics* 15, 346-353 (2021). Boqiang Shen conducted the photonic alignment and linewidth measurements, prepared the data, and participated in the writing of the manuscript.

tages have made them into a kind of 'photonic engine' for nearly all modern day optical source technology, including commercial benchtop laser sources. Nonetheless, mass manufacturable semiconductor lasers, such as used in communications systems, have linewidths ranging from 100 kHz to a few MHz [156], which is many orders of magnitude too large for the above mentioned applications.

A powerful method to narrow the linewidth of a laser is to apply optical feedback through an external reflector, for which the degree of noise suppression scales with the square of the quality (Q) factor of the reflector [149, 158–163]. Ultra-high-Q microresonators are excellent candidates to achieve substantial linewidth narrowing and have been demonstrated across a wide range of materials as discrete [86, 163] or integrated components [31, 87, 140, 164–171]. To compare laser linewidth between different works, the short-term linewidth – indicated by the level of the high-offset frequency white-noise floor – is a useful metric. Hereafter throughout the manuscript 'linewidth' will refer to the short-term linewidth. While sub-Hertz linewidth has been realized in semiconductor lasers that are self-injection-locked to discrete crystalline microresonators [163], retaining ultra-high Q factor when moving to higher levels of integration is both of paramount importance and challenging. As a measure of the level of difficulty, current demonstrations of narrow-linewidth integrated lasers, despite many years of effort, feature linewidths of 40 Hz to 1 kHz, as limited by their Q factors [139, 141, 172–174].

In this work, we present critical advances in silicon nitride waveguides, fabricated in a high-volume complementary metal-oxide-semiconductor (CMOS) foundry. We achieve a Q factor over 260 million, which is a record among all integrated resonators. By self-injection locking a conventional semiconductor distributed-feedback (DFB) laser to these ultra-high-Q microresonators, we reduce noise by five orders of magnitude, yielding frequency noise of 0.2 Hz^2 Hz^{-1} at high offset frequency, with corresponding short-term linewidth of 1.2 Hz – a previously unattainable level for integrated lasers. Within the same configuration, a new regime of Kerr comb operation in microresonators is supported. Specifically, the comb both operates turnkey [139] and attains coherent comb operation under conditions of normal dispersion without any special dispersion engineering. The comb's line spacing is suitable for dense wavelength division multiplexed (DWDM) communications systems. Moreover, each comb line benefits from the exceptional frequency noise performance of the disciplined pump, representing a significant advance for DWDM source technology. The microwave phase noise performance of the comb

is also comparable to that of existing commercial microwave oscillators. Overall, experiment and theory reveal an ultra-low-noise regime in integrated photonics.

8.2 CMOS-ready ultra-high-Q microresonators

The ultra-high Q factor resonators use high-aspect-ratio Si_3N_4 waveguides as shown in Fig. 8.1a. The samples are fabricated in a high-volume CMOS foundry on 200 mm wafers (Fig. 8.1b) following the process of Bauters et al. [175], but we increase the thickness of the Si_3N_4 core from 40 nm to 100 nm. Thicker Si_3N_4 enables a bending radius below 1 mm, allowing higher integration density than the centimeter-sized resonators demonstrated previously [31, 140, 164]. Furthermore, a top cladding thickness of 2 μm is sufficient, which obviates the need for complex chemical-mechanical polishing and bonding of additional thermal SiO_2 on top [140, 175]. To minimize the residual hydrogen content of the deposited Si_3N_4 and SiO_2 films, we also employ extended thermal treatment totaling over 20 hours of annealing at 1150 °C. Microresonators having three different free spectral ranges (FSR) were fabricated. Those resonators having 30 GHz FSR were in a whispering-gallery-mode ring geometry while single-mode racetrack resonators with 5 GHz and 10 GHz FSR were fabricated to reduce footprint (Fig. 8.1b).

The capability of CMOS-foundry fabrication to produce ultra-high Q factor at the wafer scale is exhibited in Fig 8.1c, wherein the intrinsic Q factors of 30 GHz FSR ring resonators measured throughout the wafer were observed to be clustered in the 170 M to 270 M range. Moreover, a die map (Fig 8.1c) reveals that an intrinsic Q factor in the vicinity of 200 M is observed on each die, with the exception of a single die at the center subjected to handling error during fabrication. These Q factors were measured by transmission spectra scans using a tunable external cavity laser (calibrated by a separate interferometer) to extract resonator linewidth and to infer loaded, coupled, and intrinsic optical Q factors. Cavity ring down was also performed as a separate check of these Q measurements. Spectra were observed to occur in doublets on account of both the ultra-high-Q and the presence of waveguide backscattering (Fig. 8.1d) [176]. By fitting the doublet line shape of the 30 GHz ring resonator, intrinsic Q of 220 M and loaded Q of 150 M are extracted at 1560 nm, which are further confirmed by measuring the ring-down trace of the resonance as shown in Fig. 8.1d. The spectral dependences of Q-factors in ring- and racetrack-resonators (Fig. 8.1e) provide insight into the origins of loss. A reduction in the value of Q around 1510 nm is due to absorptive N-H bonds in the Si_3N_4 core. Beyond this wavelength, the intrinsic Q factor increases monotonically versus wavelength, likely

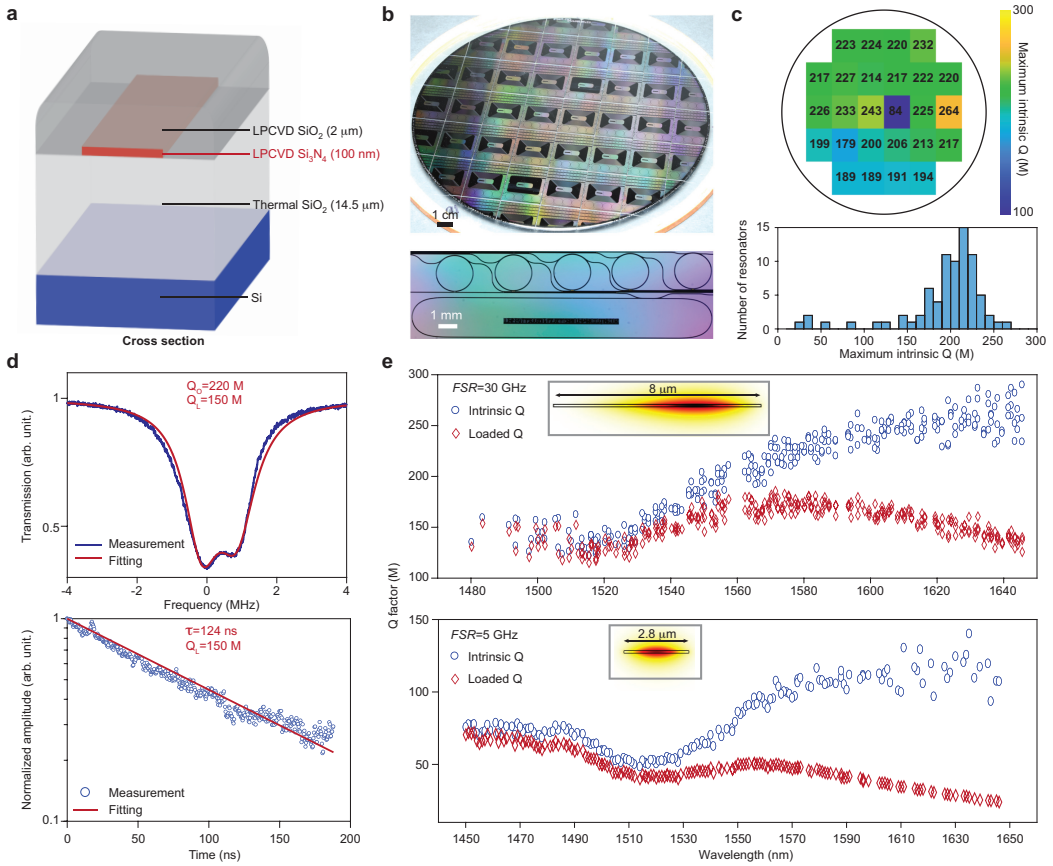

Figure 8.1: **CMOS-ready ultra-high-Q Si_3N_4 microresonators.** (**a**) Cross sectional diagram of the ultra-low loss waveguide, consisting of Si_3N_4 as the core material, silica as the cladding, and silicon as the substrate (not to scale). (**b**) Photograph of a CMOS-foundry-fabricated 200 mm diameter wafer after dicing (upper panel), and top view showing 30 GHz FSR Si_3N_4 ring resonators and a 5 GHz FSR racetrack resonator from a different reticle (lower panel). (**c**) The Q factor for each of three 30 GHZ FSR ring resonators on each of the 26 dies of the wafer shown in **b** was calculated as the average Q factor in the 1620 nm to 1650 nm range. A wafer map of the highest Q factor on each die (upper panel) and histogram of Q factors of those 78 resonators (lower panel) demonstrate that ultra-high Q is achieved across the wafer. (**d**) Transmission spectrum (upper panel) of a high-Q mode at 1560 nm in a 30 GHz ring resonator. Interfacial and volumetric inhomogeneities induce Rayleigh scattering, causing resonances to appear as doublets due to coupling between counter-propagating modes. Intrinsic Q of 220 M and loaded Q of 150 M are extracted by fitting the asymmetric mode doublet. The ring-down trace of the mode (lower panel) shows 124 ns photon lifetime, corresponding to a 150 M loaded Q. (**e**) Measured intrinsic Q factors plotted versus wavelength in a 30 GHz ring resonator with 8 μm wide Si_3N_4 core (upper panel) and a 5 GHz racetrack resonator with 2.8 μm wide Si_3N_4 core (lower panel). Insets: simulated optical mode profile.

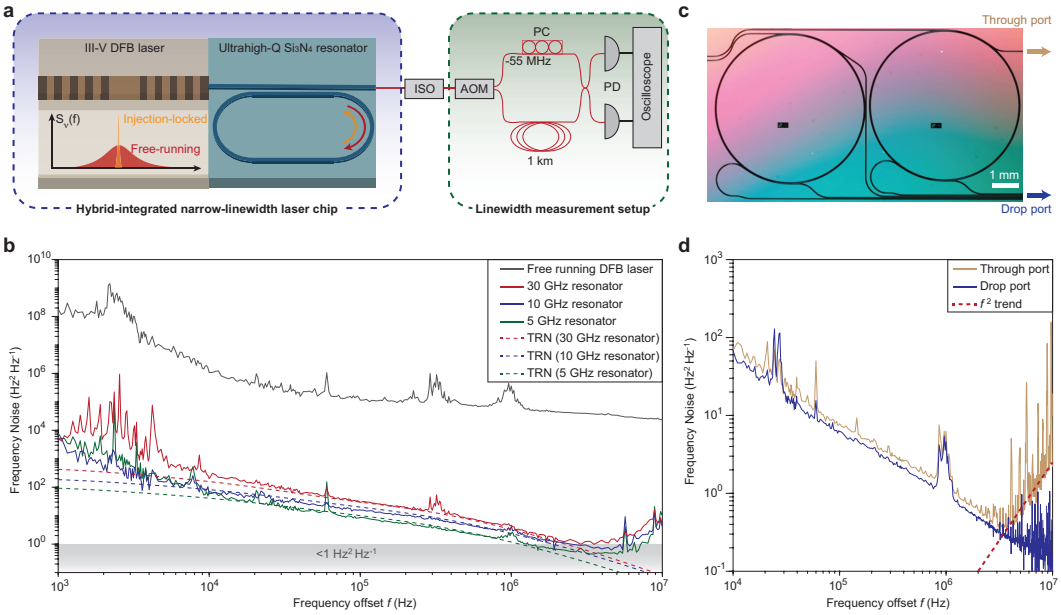

Figure 8.2: **Hybrid-integrated narrow-linewidth laser based on ultra-high-Q Si_3N_4 microresonator.** (**a**) Schematic of the hybrid laser design (not to scale) and frequency noise test setup. The red (yellow) arrow denotes the forward (backscattered) light field. ISO: optical isolator; AOM: acousto-optic modulator; PC: polarization controller; PD: photodetector. (**b**) Measurement of single-sideband frequency noise of the free-running and self-injection locked DFB laser. The minimum frequency-noise levels are 1 $Hz^2\ Hz^{-1}$, 0.8 $Hz^2\ Hz^{-1}$, 0.5 $Hz^2\ Hz^{-1}$ for resonators with 30 GHz, 10 GHz and 5 GHz FSR, respectively. The dashed lines give the simulated thermorefractive noise (TRN). (**c**) Photograph of a 10.8 GHz FSR ring resonator fabricated with a drop port. (**d**) A comparison of single sideband frequency noise measured from the through port and drop port of the same device. The drop port enables the resonator itself to act as a low-pass filter, yielding a white-noise floor of 0.2 $Hz^2\ Hz^{-1}$.

limited by Rayleigh scattering. The highest Q factor is obtained using a 30 GHz FSR resonator (mean value of 260 M and standard deviation of 13.5 M over 34 modes), and observed in the 1630 nm to 1650 nm wavelength range. The overall lower Q factor of the 5 GHz racetrack resonator suggests excess propagation loss in its single mode waveguides. This is possibly caused by higher scattering loss from increased modal overlap with the waveguide sidewall as compared to the whispering-gallery mode waveguide.

8.3 Hertz-linewidth integrated laser

The hybrid-integrated laser comprises a commercial DFB laser butt-coupled to the bus waveguide of the Si_3N_4 resonator chip (Fig. 8.2a). The laser chip, which is

mounted on a thermoelectric cooler to avoid long-term drift, is able to deliver power up to 30 mW at 1556 nm into the Si_3N_4 bus waveguide. Optical feedback is provided to the laser by backward Rayleigh scattering in the microresonator, which spontaneously aligns the laser frequency to the nearest resonator mode. As the phase accumulated in the feedback is critical to determining the stability of injection-locking [139, 149, 177], we precisely control the feedback phase by adjusting the air gap between the chips. In the case of a rigidly co-packaged laser and resonator, feedback phase control may instead be achieved by the addition of a resistive heater to the waveguide linking the laser and resonator. The laser output is taken through the bus waveguide of the microresonator, and directed to a self-heterodyne setup for frequency noise characterization. Two photodetectors and a cross-correlation technique are used to improve detection sensitivity [178] (see Methods).

The frequency noise spectra of the self-injection locked laser system using the 30 GHz ring and the 10 GHz and 5 GHz racetrack resonators (respective intrinsic Q factors of 250 M, 56 M, and 100 M) are compared in Fig. 8.2b. The ultra-high-Q factors enable the frequency noise of the free-running DFB laser to, in principle, be suppressed by up to 80 dB (see Methods). In practice, however, the noise suppression over a broad range of offset frequencies (10 kHz to 2 MHz) is limited to 50 dB by the presence of thermorefractive noise [179–181] in the microresonator. Consistent with theory, microresonators with larger mode volume, i.e. smaller FSR, experience a lower thermorefractive fluctuation and exhibit reduced frequency noise (Fig. 8.2b). At low frequency offset (below 10 kHz), frequency noise is primarily limited by temperature drift and coupling stability between chips. This can be suppressed by improved device packaging. At high offset frequencies (above 5 MHz), frequency noise rises with the square of offset frequency, as the maximum noise suppression bandwidth of injection locking is limited to the bandwidth of the resonator [152, 161, 162]. Thus, minimum frequency noise below 1 Hz^2 Hz^{-1} is observed at about 5 MHz offset frequency, where the contributions of rising laser noise and falling thermorefractive noise are approximately equal. To achieve an ultra-low white frequency noise floor at high offset frequencies, the laser output is taken from a resonator featuring a drop-port [182] (Fig. 8.2c). The drop port provides low-pass filtering action and is studied further [152]. This configuration yields of a white-noise floor of 0.2 Hz^2 Hz^{-1}, corresponding to a short-term linewidth of 1.2 Hz (Fig 8.2d).

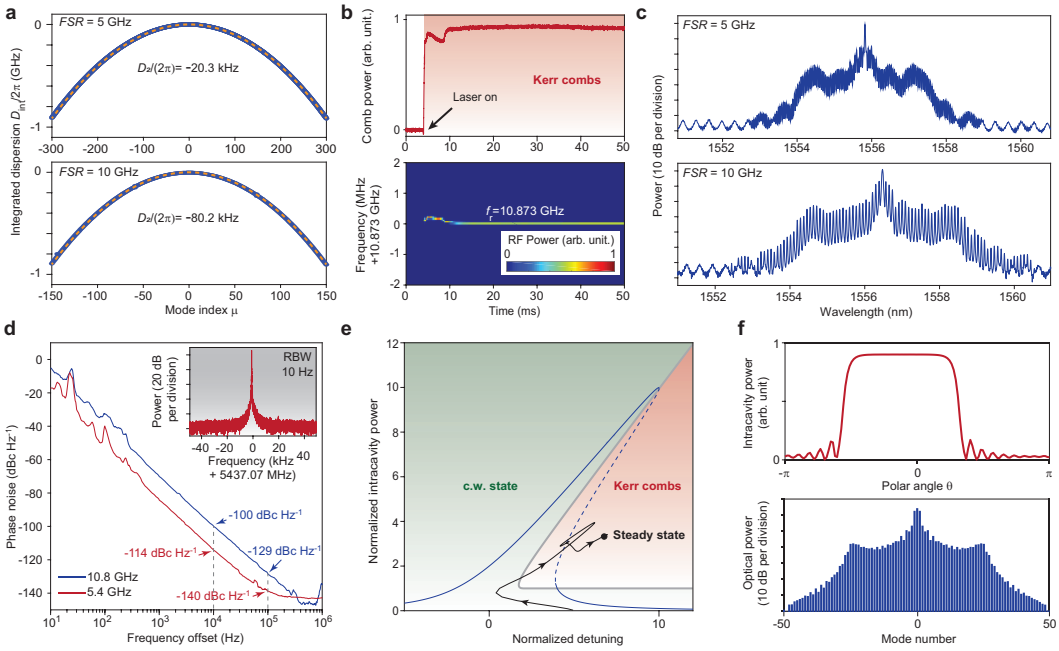

Figure 8.3: **Formation of mode-locked Kerr combs.** (**a**) Measured mode family dispersion is normal. The plot shows the integrated dispersion defined as $D_{\text{int}} = \omega_\mu - \omega_o - D_1\mu$ where ω_μ is the resonant frequency of a mode with index μ and D_1 is the FSR at $\mu = 0$. The wavelength of the central mode ($\mu = 0$) is around 1550 nm. The dashed lines are parabolic fits ($D_{\text{int}} = D_2\mu^2/2$) with $D_2/2\pi$ equal to -20.3 kHz and -80.2 kHz corresponding to 5 GHz and 10 GHz FSR, respectively. Note: $D_2 = -cD_1^2\beta_2/n_{\text{eff}}$ where β_2 is the group velocity dispersion, c the speed of light and n_{eff} the effective index of the mode. (**b**) Experimental comb power (upper panel) and detected comb repetition rate signal (lower panel) with laser turn-on indicated at 5 ms. (**c**) Measured optical spectra of mode-locked Kerr combs with 5 GHz (upper panel) and 10 GHz (lower panel) repetition rates. The background fringes are attributed to the DFB laser. (**d**) Single-sideband phase noise of dark pulse repetition rates. Dark pulses with repetition rate 10.8 GHz and 5.4 GHz are characterized. Inset: electrical beatnote showing 5.4 GHz repetition rate. (**e**) Phase diagram of microresonator pumped by an isolated laser. The backscattering is assumed weak enough to not cause mode-splittings. The detuning is normalized to one half of microresonator linewidth, while the intracavity power is normalized to parametric oscillation threshold. Green and red shaded areas indicate regimes corresponding to the c.w. state and Kerr combs. The blue curve is the c.w. intracavity power, where stable (unstable) branches are indicated by solid (dashed) lines. Simulated evolution of the unisolated laser is plotted as the solid black curve, which first evolves towards the middle unstable branch of the c.w. intracavity power curve, and then converges to the comb steady state (average normalized power shown) as marked by the black dot. The initial condition is set within the self-injection locking bandwidth, while feedback phase is set to 0. **f,** Simulated intracavity field (upper panel) and optical spectrum (lower panel) of the unisolated laser steady state in panel (**e**).

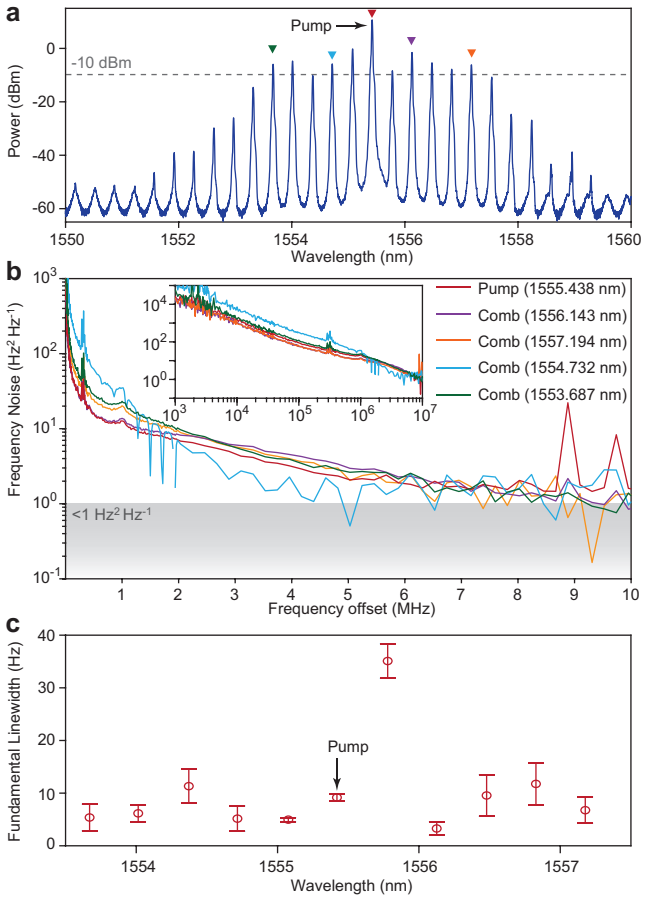

Figure 8.4: **Coherence of integrated mode-locked Kerr combs.** (**a**) Optical spectrum of a mode-locked comb with 43.2 GHz repetition rate generated in a microresonator with 10.8 GHz FSR. (**b**) Single-sideband optical frequency noise of the pump and comb lines as indicated in panel **a**, selected using a tunable fiber-Bragg-grating (FBG) filter. (Inset: the same data in log-log format) (**c**) Wavelength dependence of white frequency noise linewidth of comb lines in panel **a**.

8.4 Mode-locked dark soliton microcomb

The ultra-high Q of the microresonators enables strong resonant build-up of the circulating intensity, providing access to nonlinear optical phenomena at low input power levels [183]. As an example, optical frequency combs have been realized in continuously pumped high-Q optical microresonators due to the Kerr nonlinearity, and they are finding a wide range of applications [41]. To explore the nonlinear operating regime of the hybrid-integrated laser in pursuit of highly-coherent Kerr combs, the mode dispersion of racetrack resonators with 5 GHz and 10 GHz FSR was characterized. Their mode families are measured to have normal dispersion across the telecommunication C-band (Fig. 8.3a). Also, the dispersion curves ex-

hibit no avoided-mode-crossings, which is consistent with the single-mode nature of the waveguides. As distinct from microresonators with anomalous dispersion wherein bright soliton pulses are readily generated, comb formation is forbidden in microresonators with normal dispersion, unless avoided-mode-crossings are introduced to alter mode family dispersion so as to allow formation of dark pulses [81]. Surprisingly, however, it was nonetheless possible to readily form coherent combs in these devices without either of the aforementioned conditions being satisfied.

Indeed, deterministic, turnkey comb formation was experimentally observed when the DFB laser was switched-on to a preset driving current (see Fig. 8.3b). A clean and stable beatnote of the comb is established 5 ms after turning on the laser, indicating that mode-locking has been achieved (see Fig. 8.3b). Plotted in Fig. 8.3c are optical spectra of the mode-locked Kerr combs in racetrack resonators with 5 GHz and 10 GHz FSR, where the typical spectral shape of dark pulses is observed [41, 81, 184, 185]. The stability of mode-locking is characterized by measurement of the comb beat note phase noise (Fig. 8.3d). For Kerr combs with 10.8 (5.4) GHz FSR, the phase noise reaches -100 (-114) dBc Hz^{-1} at 10 kHz and -129 (-140) dBc Hz^{-1} at 100 kHz offset frequencies. We note that in order to suppress noise at high-offset frequencies, the pump is excluded in the photodetection using a fiber Bragg grating filter, as suggested by previous works [147].

This unexpected result is studied theoretically in the Supplement of Jin et al. [152]. Here, results from that study are briefly summarized. A phase diagram of the microcomb system is given in Fig. 8.3e, and separates resonator operation into continuous-wave (c.w.) and Kerr comb regimes based on the viability of parametric oscillation [117]. The intracavity power exhibits a typical bi-stable behavior as a function of cavity-pump frequency detuning when pumped by a laser with optical isolation [41]. In contrast, a recent study shows that the feedback from a nonlinear microresonator to a non-isolated laser creates an operating point for the compound laser-resonator system in the middle branch [139]. The operating point is induced through a combination of self- and cross-phase modulation, and is associated with turnkey operation of soliton combs operating under conditions of anomalous dispersion [139]. Here, we have validated through simulation that a similar operating point allows access to dark pulses (normal dispersion) without the requirement for extra dispersion engineering provided by avoided mode crossings. As has been previously shown for bright solitons, the phase of the feedback path plays a major role. Indeed, control of this phase through precision control of the coupling gap

between and laser and resonator chips enabled suppression of comb formation for frequency noise measurements reported in Fig. 8.2 b,d. The black curve in Fig. 8.3e gives the dynamics of the compound laser-resonator system when initialized at a point that is within the locking bandwidth of the system. It first evolves towards the operating point located on the middle branch of the c.w. power bi-stability curve, where comb formation can be initiated, and then converges to a steady Kerr comb state (average normalized power shown). The spectral and temporal profile of the steady state solutions show that flat-top pulses are formed in the microresonator with normal dispersion (Fig. 8.3f). Though the possible presence of dark pulse formation in microresonators pumped by a self-injection locked laser has been previously observed [184–186], the theory of the mutually coupled system has only recently been clarified [139, 152, 187, 188].

The combs generated in these devices exhibit several important properties. In Fig. 8.4a, the spectrum of a 43.2 GHz repetition rate comb is presented. Curiously, this spectrum was generated in a microresonator having a 10.8 GHz FSR. The appearance of rates that are different from the FSR rate has been observed for dark pulses [81]. This line spacing is compatible with DWDM channel spacings and 10 comb teeth feature on-chip optical power over -10 dBm, which is a per channel power that is readily usable in DWDM communication systems [189]. However, most significant is that the white-frequency-noise-level floor for each of these optical lines (Fig. 8.4b) is measured to be on the order of 1 Hz^2 Hz^{-1}. We note that these spectra are white at higher offset frequency, i.e., not rising for higher offset as discussed above for the laser source. The corresponding linewidths of the comb teeth are plotted in Fig. 8.4c. One of the lines exhibits degraded linewidth of approximately 30 Hz, which is suspected to be due to its coincidence with a sub-lasing-threshold side-mode of the DFB laser. Notably, certain comb teeth are quieter than the pump due to the filtering of pump noise by the ultra-high-Q modes. These results represent a two order-of-magnitude improvement as compared to previously demonstrated integrated microcombs [137, 139, 141, 186].

8.5 Performance comparison

For devices with both integrated waveguide coupler and resonator, a few platforms have emerged as able to provide ultra-high Q ($Q > 10$ M). In silica ridge resonators, a Q factor of 205 M has been demonstrated [87], while in low-confinement silicon nitride, a Q factor of 216 M has been demonstrated [164]. However, these platforms pose challenges to photonic integration with large scale and high density, e.g. the

Table 1 | Current integrated ultra-high-*Q* microresonators and narrow-linewidth lasers

Microresonators

Material	Cladding	*Q* (M)	*FSR* (GHz)	Finesse	Ref #
Si_3N_4 (this work)	Oxide	260	30	42,600	
Si_3N_4 (low confinement)	Oxide	81	3.3	1,400	24
	Oxide	65	2.7	910	3
	Oxide	216	2.7	3,000	25
Si_3N_4 (high confinement)	Oxide	37	200	38,400	26
	Oxide	67	63	21,700	26
	Oxide	30	40	6,200	27
	Oxide	14	100	7,200	28
	Air	20	100	10,340	29
SiO_2	Air	205	15.2	15,800	30
Si	Oxide	22	5.4	630	31
$LiNbO_3$	Oxide	10	4	210	32
Phosphorous-doped silica	Doped-oxide	31	1	170	33

Lasers

Operation principle	Configuration	Linewidth (Hz)	Ref #
Self-injection locking (this work)	Hybrid III-V/Si_3N_4	1.2	
External cavity	Hybrid III-V/Si_3N_4	40	34
External cavity	Heterogeneous III-V/Si	140	35
External cavity	Heterogeneous III-V/Si_3N_4	4,000	36
External cavity	Monolithic III-V	50,000	59

Figure 8.5: **Performance comparison of integrated microresonators and lasers. Upper**: Best-to-date integrated ultra-high-Q (> 10 M) microresonators with integrated waveguides. **Lower**: Linewidth of best-to-date integrated narrow-linewidth lasers.

use of suspended structures [87] or the requirement for centimeter-level bending radius [164]. While these limitations are not present in high-confinement silicon nitride resonators, the highest demonstrated Q factor is lower, 67 M [165]. In Fig. 8.5, we list key figures of merit for integrated microresonators with ultra-high-Q factors. In addition to the record-high Q factor, owing to their compact footprint, the current resonators stand out among ultra-high Q resonators for having the highest finesse as well. Fig. 8.6 provides a comparison as a plot of the Q and finesse of the current work with the state-of-the-art.

We further compare the current hybrid-integrated laser linewidth to state-of-the-art results in Fig.8.5. The linewidth of monolithic III-V lasers is generally limited to the 100 kHz to 1 MHz range by passive waveguide losses well above 1 dB cm^{-1}, with best demonstrated linewidth below 100 kHz [190]. Phase and amplitude noise scale according to the square of cavity losses [149, 162]. Thus, hybrid

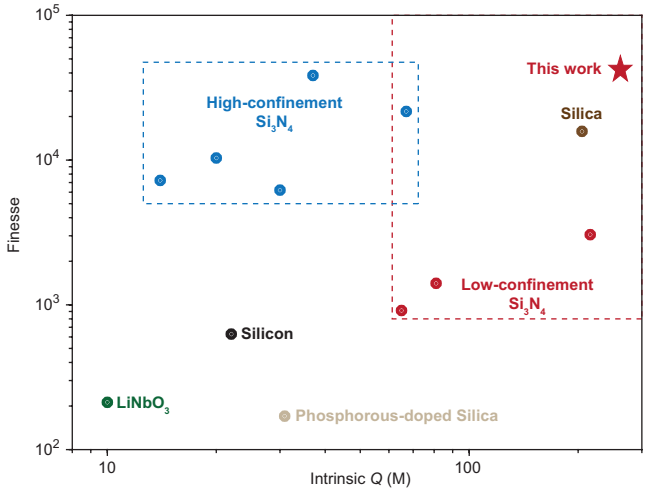

Figure 8.6: **Comparison of finesse and intrinsic Q factors of state-of-the-art integrated microresonators.**

integration, where the active III-V and passive photonic chips are assembled post-fabrication, and heterogeneous integration [191], where III-V material is directly bonded to the passive chip during fabrication, have emerged as primary technologies to create narrow-linewidth integrated lasers. As shown in Fig. 8.5, hybrid and heterogeneous integration can produce linewidth well below 1 kHz. In this work, high-offset frequency noise is suppressed to a white noise floor of 0.2 Hz^2 Hz^{-1}, or equivalently, a 1.2 Hz short-term linewidth, which is more than an order of magnitude improvement over the best results to date [172].

8.6 Discussion

As single-frequency or mode-locked lasers, these hybrid-integrated devices are readily applicable to many coherent optical systems. For example, while laboratory communication experiments pursuing spectral efficiency approaching 20 bit s^{-1} Hz^{-1} rely on high performance single-frequency fiber lasers [157], narrow-linewidth integrated photonic comb lasers could accelerate the adoption of similar schemes in practical data-center and metro links [113, 137, 139, 141, 189, 192]. Microwave photonics [27, 143, 147, 154, 155], atomic clocks [4, 73], and quantum information [193] will also benefit greatly from the reduced size, weight, power, and cost provided by the combination of ultra-high Q and photonic integration.

Many improvements beyond the results presented here are feasible. We infer propagation loss of 0.1 dB m^{-1}, however, lower loss of 0.045 dB m^{-1} is feasible in thinner cores [175], suggesting that the limits of Q for this platform have not been fully

explored. Spiral resonators with increased modal volume can suppress low-offset frequency noise induced by thermodynamic fluctuations [194]. Finally, heterogeneous integration of III-V lasers and ultra-high-Q microresonators may eventually unite the device onto a single chip [173, 174, 191], leading to scalable production with high yield using foundry-based technologies.

BIBLIOGRAPHY

[1] Scott A. Diddams. The evolving optical frequency comb. *Journal of the Optical Society of America A*, 27(11):B51–B62, 2010.

[2] Scott A. Diddams, Kerry Vahala, and Thomas Udem. Optical frequency combs: Coherently uniting the electromagnetic spectrum. *Science*, 369 (6501), 2020.

[3] Scott B. Papp, Katja Beha, Pascal Del'Haye, Franklyn Quinlan, Hansuek Lee, Kerry J. Vahala, and Scott A. Diddams. Microresonator frequency comb optical clock. *Optica*, 1(1):10–14, 2014.

[4] Zachary L. Newman, Vincent Maurice, Tara Drake, Jordan R. Stone, Travis C. Briles, Daryl T. Spencer, Connor Fredrick, Qing Li, Daron Westly, B. R. Ilic, et al. Architecture for the photonic integration of an optical atomic clock. *Optica*, 6(5):680–685, 2019.

[5] J. Reichert, R. Holzwarth, Th. Udem, and T. W. Haensch. Measuring the frequency of light with mode-locked lasers. *Optics Communications*, 172 (1-6):59–68, 1999.

[6] David J. Jones, Scott A. Diddams, Jinendra K. Ranka, Andrew Stentz, Robert S. Windeler, John L. Hall, and Steven T. Cundiff. Carrier-envelope phase control of femtosecond mode-locked lasers and direct optical frequency synthesis. *Science*, 288(5466):635–639, 2000.

[7] Scott A. Diddams, David J. Jones, Jun Ye, Steven T. Cundiff, John L. Hall, Jinendra K. Ranka, Robert S. Windeler, Ronald Holzwarth, Thomas Udem, and Theodor W. Hänsch. Direct link between microwave and optical frequencies with a 300 thz femtosecond laser comb. *Physical Review Letters*, 84(22): 5102, 2000.

[8] R. Holzwarth, Th. Udem, T. W. Hänsch, J. C. Knight, W. J. Wadsworth, and P. St. J. Russell. Optical frequency synthesizer for precision spectroscopy. *Physical Review Letters*, 85(11):2264, 2000.

[9] Daryl T. Spencer, Tara Drake, Travis C. Briles, Jordan Stone, Laura C. Sinclair, Connor Fredrick, Qing Li, Daron Westly, B. Robert Ilic, Aaron Bluestone, et al. An optical-frequency synthesizer using integrated photonics. *Nature*, 557(7703):81–85, 2018.

[10] Ian Coddington, Nathan Newbury, and William Swann. Dual-comb spectroscopy. *Optica*, 3(4):414–426, 2016.

[11] Myoung-Gyun Suh, Qi-Fan Yang, Ki Youl Yang, Xu Yi, and Kerry J. Vahala. Microresonator soliton dual-comb spectroscopy. *Science*, 354(6312):600–603, 2016.

[12] N. G. Pavlov, G. Lihachev, S. Koptyaev, E. Lucas, M. Karpov, N. M. Kondratiev, I. A. Bilenko, T. J. Kippenberg, and M. L. Gorodetsky. Soliton dual frequency combs in crystalline microresonators. *Optics Letters*, 42(3): 514–517, 2017.

[13] Mengjie Yu, Yoshitomo Okawachi, Austin G. Griffith, Nathalie Picqué, Michal Lipson, and Alexander L. Gaeta. Silicon-chip-based mid-infrared dual-comb spectroscopy. *Nature Communications*, 9(1):1–6, 2018.

[14] Qi-Fan Yang, Boqiang Shen, Heming Wang, Minh Tran, Zhewei Zhang, Ki Youl Yang, Lue Wu, Chengying Bao, John Bowers, Amnon Yariv, et al. Vernier spectrometer using counterpropagating soliton microcombs. *Science*, 363(6430):965–968, 2019.

[15] I. Coddington, W. C. Swann, L. Nenadovic, and N. R. Newbury. Rapid and precise absolute distance measurements at long range. *Nature Photonics*, 3 (6):351–356, 2009.

[16] Myoung-Gyun Suh and Kerry J. Vahala. Soliton microcomb range measurement. *Science*, 359(6378):884–887, 2018.

[17] Philipp Trocha, M. Karpov, D. Ganin, Martin H. P. Pfeiffer, Arne Kordts, S. Wolf, J. Krockenberger, Pablo Marin-Palomo, Claudius Weimann, Sebastian Randel, et al. Ultrafast optical ranging using microresonator soliton frequency combs. *Science*, 359(6378):887–891, 2018.

[18] Johann Riemensberger, Anton Lukashchuk, Maxim Karpov, Wenle Weng, Erwan Lucas, Junqiu Liu, and Tobias J. Kippenberg. Massively parallel coherent laser ranging using a soliton microcomb. *Nature*, 581(7807):164–170, 2020.

[19] Tilo Steinmetz, Tobias Wilken, Constanza Araujo-Hauck, Ronald Holzwarth, Theodor W Hänsch, Luca Pasquini, Antonio Manescau, Sandro D'odorico, Michael T Murphy, Thomas Kentischer, et al. Laser frequency combs for astronomical observations. *Science*, 321(5894):1335–1337, 2008.

[20] Xu Yi, K. Vahala, J. Li, S. Diddams, G. Ycas, P. Plavchan, S. Leifer, J. Sandhu, G. Vasisht, P. Chen, et al. Demonstration of a near-IR line-referenced electro-optical laser frequency comb for precision radial velocity measurements in astronomy. *Nature Communications*, 7(1):1–9, 2016.

[21] Takayuki Kotani, Motohide Tamura, Jun Nishikawa, Akitoshi Ueda, Masayuki Kuzuhara, Masashi Omiya, Jun Hashimoto, Masato Ishizuka, Teruyuki Hirano, Hiroshi Suto, et al. The infrared doppler (ird) instrument

for the subaru telescope: instrument description and commissioning results. In *Ground-based and Airborne Instrumentation for Astronomy VII*, volume 10702, page 1070211. International Society for Optics and Photonics, 2018.

[22] Andrew J. Metcalf, Tyler Anderson, Chad F. Bender, Scott Blakeslee, Wesley Brand, David R. Carlson, William D. Cochran, Scott A. Diddams, Michael Endl, Connor Fredrick, et al. Stellar spectroscopy in the near-infrared with a laser frequency comb. *Optica*, 6(2):233–239, 2019.

[23] Myoung-Gyun Suh, Xu Yi, Yu-Hung Lai, S. Leifer, Ivan S. Grudinin, G. Vasisht, Emily C. Martin, Michael P. Fitzgerald, G Doppmann, J. Wang, et al. Searching for exoplanets using a microresonator astrocomb. *Nature Photonics*, 13(1):25–30, 2019.

[24] Ewelina Obrzud, Monica Rainer, Avet Harutyunyan, Miles H Anderson, Junqiu Liu, Michael Geiselmann, Bruno Chazelas, Stefan Kundermann, Steve Lecomte, Massimo Cecconi, et al. A microphotonic astrocomb. *Nature Photonics*, 13(1):31–35, 2019.

[25] Rafael A. Probst, Dinko Milaković, Borja Toledo-Padrón, Gaspare Lo Curto, Gerardo Avila, Anna Brucalassi, Bruno L. Canto Martins, Izan de Castro Leão, Massimiliano Esposito, Jonay I. González Hernández, et al. A crucial test for astronomical spectrograph calibration with frequency combs. *Nature Astronomy*, 4(6):603–608, 2020.

[26] Tara M. Fortier, Matthew S. Kirchner, F. Quinlan, J. Taylor, J. C. Bergquist, T. Rosenband, N. Lemke, A. Ludlow, Y. Jiang, C. W. Oates, et al. Generation of ultrastable microwaves via optical frequency division. *Nature Photonics*, 5(7):425–429, 2011.

[27] Jiang Li, Hansuek Lee, and Kerry J. Vahala. Microwave synthesizer using an on-chip Brillouin oscillator. *Nature Communications*, 4(1):2041–1723, Oct 2013. doi: 10.1038/ncomms3097.

[28] Xiaopeng Xie, Romain Bouchand, Daniele Nicolodi, Michele Giunta, Wolfgang Hänsel, Matthias Lezius, Abhay Joshi, Shubhashish Datta, Christophe Alexandre, Michel Lours, et al. Photonic microwave signals with zeptosecond-level absolute timing noise. *Nature Photonics*, 11(1):44–47, 2017.

[29] Phuong T. Do, Carlos Alonso-Ramos, Xavier Le Roux, Isabelle Ledoux, Bernard Journet, and Eric Cassan. Wideband tunable microwave signal generation in a silicon-micro-ring-based optoelectronic oscillator. *Scientific Reports*, 10(1):1–9, 2020.

[30] Jian Tang, Tengfei Hao, Wei Li, David Domenech, Rocio Baños, Pascual Muñoz, Ninghua Zhu, José Capmany, and Ming Li. Integrated optoelectronic oscillator. *Optics Express*, 26(9):12257–12265, 2018.

[31] Sarat Gundavarapu, Grant M. Brodnik, Matthew Puckett, Taran Huffman, Debapam Bose, Ryan Behunin, Jianfeng Wu, Tiequn Qiu, Cátia Pinho, Nitesh Chauhan, et al. Sub-hertz fundamental linewidth photonic integrated Brillouin laser. *Nature Photonics*, 13(1):60–67, 2019.

[32] T. J. Kippenberg, S. M. Spillane, and K. J. Vahala. Kerr-nonlinearity optical parametric oscillation in an ultrahigh-Q toroid microcavity. *Physical Review Letters*, 93(8):083904, 2004.

[33] Anatoliy A. Savchenkov, Andrey B. Matsko, Dmitry Strekalov, Makan Mohageg, Vladimir S. Ilchenko, and Lute Maleki. Low threshold optical oscillations in a whispering gallery mode c a f 2 resonator. *Physical Review Letters*, 93(24):243905, 2004.

[34] P. Del'Haye, A. Schliesser, O. Arcizet, T. Wilken, R. Holzwarth, and T. J. Kippenberg. Optical frequency comb generation from a monolithic microresonator. *Nature*, 450(7173):1214–1217, 2007.

[35] Stefan Wabnitz. Suppression of interactions in a phase-locked soliton optical memory. *Optics Letters*, 18(8):601–603, 1993.

[36] François Leo, Stéphane Coen, Pascal Kockaert, Simon-Pierre Gorza, Philippe Emplit, and Marc Haelterman. Temporal cavity solitons in one-dimensional Kerr media as bits in an all-optical buffer. *Nature Photonics*, 4(7):471–476, 2010.

[37] T. Herr, V. Brasch, J. D. Jost, C. Y. Wang, N. M. Kondratiev, M. L. Gorodetsky, and T. J. Kippenberg. Temporal solitons in optical microresonators. *Nature Photonics*, 8(2):145–152, 2014.

[38] Xu Yi, Qi-Fan Yang, Ki Youl Yang, Myoung-Gyun Suh, and Kerry Vahala. Soliton frequency comb at microwave rates in a high-Q silica microresonator. *Optica*, 2(12):1078–1085, 2015.

[39] Chaitanya Joshi, Jae K. Jang, Kevin Luke, Xingchen Ji, Steven A. Miller, Alexander Klenner, Yoshitomo Okawachi, Michal Lipson, and Alexander L. Gaeta. Thermally controlled comb generation and soliton modelocking in microresonators. *Optics Letters*, 41(11):2565–2568, 2016.

[40] Pei-Hsun Wang, Jose A. Jaramillo-Villegas, Yi Xuan, Xiaoxiao Xue, Chengying Bao, Daniel E. Leaird, Minghao Qi, and Andrew M. Weiner. Intracavity characterization of micro-comb generation in the single-soliton regime. *Optics Express*, 24(10):10890–10897, 2016.

[41] Tobias J. Kippenberg, Alexander L. Gaeta, Michal Lipson, and Michael L. Gorodetsky. Dissipative Kerr solitons in optical microresonators. *Science*, 361(6402), 2018. ISSN 0036-8075. doi: 10.1126/science.aan8083.

[42] B. J. M. Hausmann, I. Bulu, V. Venkataraman, P. Deotare, and Marko Lončar. Diamond nonlinear photonics. *Nature Photonics*, 8(5):369–374, 2014.

[43] V. Brasch, M. Geiselmann, T. Herr, G. Lihachev, M. H. P. Pfeiffer, M. L. Gorodetsky, and T. J. Kippenberg. Photonic chip–based optical frequency comb using soliton Cherenkov radiation. *Science*, 351(6271):357–360, 2016.

[44] Qing Li, Travis C. Briles, Daron A. Westly, Tara E. Drake, Jordan R. Stone, B. Robert Ilic, Scott A. Diddams, Scott B. Papp, and Kartik Srinivasan. Stably accessing octave-spanning microresonator frequency combs in the soliton regime. *Optica*, 4(2):193–203, 2017.

[45] Martin H. P. Pfeiffer, Clemens Herkommer, Junqiu Liu, Hairun Guo, Maxim Karpov, Erwan Lucas, Michael Zervas, and Tobias J Kippenberg. Octave-spanning dissipative Kerr soliton frequency combs in Si_3N_4 microresonators. *Optica*, 4(7):684–691, 2017.

[46] Scott B. Papp and Scott A. Diddams. Spectral and temporal characterization of a fused-quartz-microresonator optical frequency comb. *Physical Review A*, 84(5):053833, 2011.

[47] Zheng Gong, Alexander Bruch, Mohan Shen, Xiang Guo, Hojoong Jung, Linran Fan, Xianwen Liu, Liang Zhang, Junxi Wang, Jinmin Li, et al. High-fidelity cavity soliton generation in crystalline AlN micro-ring resonators. *Optics Letters*, 43(18):4366–4369, 2018.

[48] Yang He, Qi-Fan Yang, Jingwei Ling, Rui Luo, Hanxiao Liang, Mingxiao Li, Boqiang Shen, Heming Wang, Kerry Vahala, and Qiang Lin. Self-starting bi-chromatic $LiNbO_3$ soliton microcomb. *Optica*, 6(9):1138–1144, 2019.

[49] Lin Chang, Weiqiang Xie, Haowen Shu, Qi-Fan Yang, Boqiang Shen, Andreas Boes, Jon D. Peters, Warren Jin, Chao Xiang, Songtao Liu, et al. Ultra-efficient frequency comb generation in AlGaAs-on-insulator microresonators. *Nature Communications*, 11(1331), 2020.

[50] Seung Hoon Lee, Dong Yoon Oh, Qi-Fan Yang, Boqiang Shen, Heming Wang, Ki Youl Yang, Yu-Hung Lai, Xu Yi, Xinbai Li, and Kerry Vahala. Towards visible soliton microcomb generation. *Nature Communications*, 8 (1):1295, 2017.

[51] Heming Wang, Yu-Kun Lu, Lue Wu, Dong Yoon Oh, Boqiang Shen, Seung Hoon Lee, and Kerry Vahala. Dirac solitons in optical microresonators. *Light: Science & Applications*, 9(205), 2020. doi: 10.1038/s41377-020-00438-w.

[52] T. Kobayashi, T. Sueta, Y. Cho, and Y. Matsuo. High-repetition-rate optical pulse generator using a Fabry-Perot electro-optic modulator. *Applied Physics Letters*, 21(8):341–343, 1972.

[53] Motonobu Kourogi, Ken'ichi Nakagawa, and Motoichi Ohtsu. Wide-span optical frequency comb generator for accurate optical frequency difference measurement. *IEEE Journal of Quantum Electronics*, 29(10):2693–2701, 1993.

[54] Isao Morohashi, Takahide Sakamoto, Hideyuki Sotobayashi, Tetsuya Kawanishi, Iwao Hosako, and Masahiro Tsuchiya. Widely repetition-tunable 200 fs pulse source using a Mach–Zehnder-modulator-based flat comb generator and dispersion-flattened dispersion-decreasing fiber. *Optics Letters*, 33(11): 1192–1194, 2008.

[55] Atsushi Ishizawa, Tadashi Nishikawa, Akira Mizutori, Hidehiko Takara, Hidetoshi Nakano, Tetsuomi Sogawa, Atsushi Takada, and Masafumi Koga. Generation of 120-fs laser pulses at 1-GHz repetition rate derived from continuous wave laser diode. *Optics Express*, 19(23):22402–22409, 2011.

[56] Andrew J. Metcalf, Victor Torres-Company, Daniel E. Leaird, and Andrew M Weiner. High-power broadly tunable electrooptic frequency comb generator. *IEEE Journal of Selected Topics in Quantum Electronics*, 19(6):231–236, 2013.

[57] Masamichi Fujiwara, Mitsuhiro Teshima, Jun-ichi Kani, Hiro Suzuki, Noboru Takachio, and Katsumi Iwatsuki. Optical carrier supply module using flattened optical multicarrier generation based on sinusoidal amplitude and phase hybrid modulation. *Journal of lightwave technology*, 21(11):2705–2714, 2003.

[58] Yujie Dou, Hongming Zhang, and Minyu Yao. Improvement of flatness of optical frequency comb based on nonlinear effect of intensity modulator. *Optics Letters*, 36(14):2749–2751, 2011.

[59] Michel Mayor and Didier Queloz. A Jupiter-mass companion to a solar-type star. *Nature*, 378(6555):355–359, 1995.

[60] F. Pepe, Paolo Molaro, Stefano Cristiani, R. Rebolo, N. C. Santos, H. Dekker, D. Mégevand, FM Zerbi, A. Cabral, Paolo Di Marcantonio, et al. Espresso: The next european exoplanet hunter, 2014.

[61] Ryan R. Petersburg, JM Joel Ong, Lily L. Zhao, Ryan T. Blackman, John M. Brewer, Lars A. Buchhave, Samuel H. C. Cabot, Allen B. Davis, Colby A. Jurgenson, Christopher Leet, et al. An extreme-precision radial-velocity pipeline: First radial velocities from expres. *The Astronomical Journal*, 159 (5):187, 2020.

[62] C. Schwab, A. Rakich, Q. Gong, S. Mahadevan, SP Halverson, A. Roy, RC Terrien, P. M. Robertson, F. R. Hearty, EI Levi, et al. Design of neid, an extreme precision doppler spectrograph for wiyn. In *Ground-based and Airborne Instrumentation for Astronomy VI*, volume 9908, page 99087H. International Society for Optics and Photonics, 2016.

[63] Tobias Wilken, Gaspare Lo Curto, Rafael A. Probst, Tilo Steinmetz, Antonio Manescau, Luca Pasquini, Jonay I. González Hernández, Rafael Rebolo, Theodor W Hänsch, Thomas Udem, et al. A spectrograph for exoplanet observations calibrated at the centimetre-per-second level. *Nature*, 485(7400): 611–614, 2012.

[64] Ewelina Obrzud, Monica Rainer, Avet Harutyunyan, Bruno Chazelas, Massimo Cecconi, Adriano Ghedina, Emilio Molinari, Stefan Kundermann, Steve Lecomte, Francesco Pepe, et al. Broadband near-infrared astronomical spectrometer calibration and on-sky validation with an electro-optic laser frequency comb. *Nature Photonics*, 26(26):34830–34841, 2018.

[65] A. J. Metcalf, C. Bender, S. Blakeslee, W. Brand, D. Carlson, S. A. Diddams, C. Fredrick, S. Halverson, F. Hearty, D. Hickstein, et al. Infrared astronomical spectroscopy for radial velocity measurements with 10 cm/s precision. In *Conference on Lasers and Electro-Optics 2018*, pages JTh5A–1. Optical Society of America, 2018.

[66] Rafael A. Probst, Gaspare Lo. Curto, Gerardo Avila, Bruno L. Canto Martins, José Renan de Medeiros, Massimiliano Esposito, Jonay I. González Hernández, Theodor W Hänsch, Ronald Holzwarth, Florian Kerber, et al. A laser frequency comb featuring sub-cm/s precision for routine operation on harps. In *Ground-based and Airborne Instrumentation for Astronomy V*, volume 9147, page 91471C. International Society for Optics and Photonics, 2014.

[67] Tobias J. Kippenberg, Ronald Holzwarth, and S. A. Diddams. Microresonator-based optical frequency combs. *Science*, 332(6029):555–559, 2011.

[68] Qi-Fan Yang, Xu Yi, Ki Youl Yang, and Kerry Vahala. Stokes solitons in optical microcavities. *Nature Physics*, 13:53–57, 2017.

[69] Kevin Luke, Yoshitomo Okawachi, Michael R. E. Lamont, Alexander L. Gaeta, and Michal Lipson. Broadband mid-infrared frequency comb generation in a Si_3N_4 microresonator. *Optics Letters*, 40(21):4823–4826, 2015.

[70] Anatoliy A. Savchenkov, Vladimir S. Ilchenko, Fabio Di Teodoro, Paul M. Belden, William T. Lotshaw, Andrey B. Matsko, and Lute Maleki. Generation of Kerr combs centered at 4.5 μm in crystalline microresonators pumped with quantum-cascade lasers. *Optics Letters*, 40(15):3468–3471, 2015.

[71] Mengjie Yu, Yoshitomo Okawachi, Austin G. Griffith, Michal Lipson, and Alexander L. Gaeta. Mode-locked mid-infrared frequency combs in a silicon microresonator. *Optica*, 3(8):854–860, 2016.

[72] Andreas Hugi, Gustavo Villares, Stéphane Blaser, H. C. Liu, and Jérôme Faist. Mid-infrared frequency comb based on a quantum cascade laser. *Nature*, 492 (7428):229–233, 2012.

[73] Andrew D. Ludlow, Martin M. Boyd, Jun Ye, Ekkehard Peik, and Piet O. Schmidt. Optical atomic clocks. *Reviews of Modern Physics*, 87(2):637, 2015.

[74] Stefan Kray, Felix Spöler, Michael Först, and Heinrich Kurz. Dual femtosecond laser multiheterodyne optical coherence tomography. *Optics Letters*, 33 (18):2092–2094, 2008.

[75] Tomasz Bajraszewski, Maciej Wojtkowski, Maciej Szkulmowski, Anna Szkulmowska, Robert Huber, and Andrzej Kowalczyk. Improved spectral optical coherence tomography using optical frequency comb. *Optics Express*, 16(6):4163–4176, 2008.

[76] Kasturi Saha, Yoshitomo Okawachi, Jacob S. Levy, Ryan K. W. Lau, Kevin Luke, Mark A. Foster, Michal Lipson, and Alexander L. Gaeta. Broadband parametric frequency comb generation with a 1-μm pump source. *Optics Express*, 20(24):26935–26941, 2012.

[77] Hojoong Jung, Rebecca Stoll, Xiang Guo, Debra Fischer, and Hong X. Tang. Green, red, and IR frequency comb line generation from single IR pump in AlN microring resonator. *Optica*, 1(6):396–399, 2014.

[78] Leiran Wang, Lin Chang, Nicolas Volet, Martin H. P. Pfeiffer, Michael Zervas, Hairun Guo, Tobias J. Kippenberg, and John E. Bowers. Frequency comb generation in the green using silicon nitride microresonators. *Laser & Photonics Reviews*, 10(4):631–638, 2016.

[79] A. A. Savchenkov, A. B. Matsko, W. Liang, V. S. Ilchenko, D. Seidel, and L. Maleki. Kerr combs with selectable central frequency. *Nature Photonics*, 5(5):293–296, 2011.

[80] Yong Yang, Xuefeng Jiang, Sho Kasumie, Guangming Zhao, Linhua Xu, Jonathan M. Ward, Lan Yang, and Síle Nic Chormaic. Four-wave mixing parametric oscillation and frequency comb generation at visible wavelengths in a silica microbubble resonator. *Optics Letters*, 41(22):5266–5269, 2016.

[81] Xiaoxiao Xue, Yi Xuan, Yang Liu, Pei-Hsun Wang, Steven Chen, Jian Wang, Dan E. Leaird, Minghao Qi, and Andrew M. Weiner. Mode-locked dark pulse Kerr combs in normal-dispersion microresonators. *Nature Photonics*, 9(9): 594–600, 2015.

[82] Ki Youl Yang, Katja Beha, Daniel C. Cole, Xu Yi, Pascal Del'Haye, Hansuek Lee, Jiang Li, Dong Yoon Oh, Scott A. Diddams, Scott B. Papp, et al. Broadband dispersion-engineered microresonator on a chip. *Nature Photonics*, 10 (5):316–320, 2016.

[83] Dong Yoon Oh, Ki Youl Yang, Connor Fredrick, Gabriel Ycas, Scott A. Diddams, and Kerry J. Vahala. Coherent ultra-violet to near-infrared generation in silica ridge waveguides. *Nature Communications*, 8(1):1–7, 2017.

[84] David J. Moss, Roberto Morandotti, Alexander L. Gaeta, and Michal Lipson. New CMOS-compatible platforms based on silicon nitride and Hydex for nonlinear optics. *Nature Photonics*, 7(8):597–607, 2013.

[85] Chi Xiong, Wolfram H. P. Pernice, Xiankai Sun, Carsten Schuck, King Y. Fong, and Hong X. Tang. Aluminum nitride as a new material for chip-scale optomechanics and nonlinear optics. *New Journal of Physics*, 14(9):095014, 2012.

[86] Hansuek Lee, Tong Chen, Jiang Li, Ki Youl Yang, Seokmin Jeon, Oskar Painter, and Kerry J. Vahala. Chemically etched ultrahigh-Q wedge-resonator on a silicon chip. *Nature Photonics*, 6(6):369–373, 2012.

[87] Ki Youl Yang, Dong Yoon Oh, Seung Hoon Lee, Qi-Fan Yang, Xu Yi, Boqiang Shen, Heming Wang, and Kerry Vahala. Bridging ultrahigh-Q devices and photonic circuits. *Nature Photonics*, 12(5):297–302, 2018.

[88] Carles Milián, Andrey V. Gorbach, Majid Taki, Alexey V. Yulin, and Dmitry V. Skryabin. Solitons and frequency combs in silica microring resonators: Interplay of the raman and higher-order dispersion effects. *Physical Review A*, 92(3):033851, 2015.

[89] Maxim Karpov, Hairun Guo, Arne Kordts, Victor Brasch, Martin H. P. Pfeiffer, Michail Zervas, Michael Geiselmann, and Tobias J. Kippenberg. Raman self-frequency shift of dissipative Kerr solitons in an optical microresonator. *Physical Review Letters*, 116(10):103902, 2016.

[90] Xu Yi, Qi-Fan Yang, Ki Youl Yang, and Kerry Vahala. Theory and measurement of the soliton self-frequency shift and efficiency in optical microcavities. *Optics Letters*, 41(15):3419–3422, 2016.

[91] Xu Yi, Qi-Fan Yang, Ki Youl, and Kerry Vahala. Active capture and stabilization of temporal solitons in microresonators. *Optics Letters*, 41(9): 2037–2040, 2016.

[92] Daoxin Dai and John E. Bowers. Novel concept for ultracompact polarization splitter-rotator based on silicon nanowires. *Optics Express*, 19(11):10940–10949, 2011.

[93] Tong Chen, Hansuek Lee, and Kerry J. Vahala. Thermal stress in silica-on-silicon disk resonators. *Applied Physics Letters*, 102(3):031113, 2013.

[94] Stéphane Coen and Miro Erkintalo. Universal scaling laws of Kerr frequency combs. *Optics Letters*, 38(11):1790–1792, 2013.

[95] Xinbai Li, Boqiang Shen, Heming Wang, Ki Youl Yang, Xu Yi, Qi-Fan Yang, Zhiping Zhou, and Kerry Vahala. Universal isocontours for dissipative Kerr solitons. *Optics Letters*, 43(11):2567–2570, 2018. doi: 10.1364/OL.43.002567.

[96] Yuri S. Kivshar and Govind Agrawal. *Optical solitons: From fibers to photonic crystals*. Academic Press, 2003.

[97] Govind P. Agrawal. *Nonlinear fiber optics*. Academic Press, 2007.

[98] S. T. Cundiff. Soliton dynamics in mode-locked lasers. In *Dissipative Solitons*, pages 183–206. Springer, 2005.

[99] John M. Dudley, Goëry Genty, and Stéphane Coen. Supercontinuum generation in photonic crystal fiber. *Reviews of Modern Physics*, 78(4):1135, 2006.

[100] Akira Hasegawa and Yuji Kodama. Signal transmission by optical solitons in monomode fiber. *Proceedings of the IEEE*, 69(9):1145–1150, 1981.

[101] Hermann A. Haus and William S. Wong. Solitons in optical communications. *Reviews of Modern Physics*, 68(2):423, 1996.

[102] N. Akhmediev and A. Ankiewicz. *Dissipative Solitons: From Optics to Biology and Medicine*. Berlin: Springer, 2008.

[103] Jae K. Jang, Miro Erkintalo, Stuart G. Murdoch, and Stéphane Coen. Observation of dispersive wave emission by temporal cavity solitons. *Optics Letters*, 39(19):5503–5506, 2014.

[104] Miles Anderson, François Leo, Stéphane Coen, Miro Erkintalo, and Stuart G. Murdoch. Observations of spatiotemporal instabilities of temporal cavity solitons. *Optica*, 3(10):1071–1074, 2016.

[105] Yadong Wang, Miles Anderson, Stéphane Coen, Stuart G. Murdoch, and Miro Erkintalo. Stimulated raman scattering imposes fundamental limits to the duration and bandwidth of temporal cavity solitons. *Physical Review Letters*, 120(5):053902, 2018.

[106] Xu Yi, Qi-Fan Yang, Xueyue Zhang, Ki Youl Yang, Xinbai Li, and Kerry Vahala. Single-mode dispersive waves and soliton microcomb dynamics. *Nature Communications*, 8(14869):14869, 2016.

[107] Nail Akhmediev and Magnus Karlsson. Cherenkov radiation emitted by solitons in optical fibers. *Physical Review A*, 51(3):2602, 1995.

[108] Chengying Bao, Yi Xuan, Daniel E. Leaird, Stefan Wabnitz, Minghao Qi, and Andrew M. Weiner. Spatial mode-interaction induced single soliton generation in microresonators. *Optica*, 4(9):1011–1015, 2017.

[109] A. V. Cherenkov, V. E. Lobanov, and M. L. Gorodetsky. Dissipative Kerr solitons and Cherenkov radiation in optical microresonators with third-order dispersion. *Physical Review A*, 95(3):033810, 2017.

[110] Qi-Fan Yang, Xu Yi, Ki Youl Yang, and Kerry Vahala. Counter-propagating solitons in microresonators. *Nature Photonics*, 11(9):560–564, 2017.

[111] Chaitanya Joshi, Alexander Klenner, Yoshitomo Okawachi, Mengjie Yu, Kevin Luke, Xingchen Ji, Michal Lipson, and Alexander L. Gaeta. Counter-rotating cavity solitons in a silicon nitride microresonator. *arXiv preprint arXiv:1711.04849*, 2017.

[112] Daniel C. Cole, Erin S. Lamb, Pascal Del¡¯Haye, Scott A. Diddams, and Scott B. Papp. Soliton crystals in Kerr resonators. *Nature Photonics*, 11(10): 671, 2017.

[113] Pablo Marin-Palomo, Juned N. Kemal, Maxim Karpov, Arne Kordts, Joerg Pfeifle, Martin H. P. Pfeiffer, Philipp Trocha, Stefan Wolf, Victor Brasch, Miles H. Anderson, et al. Microresonator-based solitons for massively parallel coherent optical communications. *Nature*, 546(7657):274, 2017.

[114] I.V. Barashenkov and Yu S. Smirnov. Existence and stability chart for the ac-driven, damped nonlinear Schrödinger solitons. *Physical Review E*, 54(5): 5707, 1996.

[115] Luigi A. Lugiato and René Lefever. Spatial dissipative structures in passive optical systems. *Physical Review Letters*, 58(21):2209, 1987.

[116] François Leo, Lendert Gelens, Philippe Emplit, Marc Haelterman, and Stéphane Coen. Dynamics of one-dimensional Kerr cavity solitons. *Optics Express*, 21(7):9180–9191, 2013.

[117] Cyril Godey, Irina V Balakireva, Aurélien Coillet, and Yanne K. Chembo. Stability analysis of the spatiotemporal Lugiato-Lefever model for Kerr optical frequency combs in the anomalous and normal dispersion regimes. *Physical Review A*, 89(6):063814, 2014.

[118] H. Guo, M. Karpov, E. Lucas, A. Kordts, M. H. P. Pfeiffer, V. Brasch, G. Lihachev, V. E. Lobanov, M. L. Gorodetsky, and T. J. Kippenberg. Universal dynamics and deterministic switching of dissipative Kerr solitons in optical microresonators. *Nature Physics*, 13(1):94–102, 2017.

[119] Chengying Bao, Jose A. Jaramillo-Villegas, Yi Xuan, Daniel E. Leaird, Minghao Qi, and Andrew M. Weiner. Observation of fermi-pasta-ulam recurrence induced by breather solitons in an optical microresonator. *Physical Review Letters*, 117(16):163901, 2016.

[120] Erwan Lucas, Maxim Karpov, Hairun Guo, M. L. Gorodetsky, and T. J. Kippenberg. Breathing dissipative solitons in optical microresonators. *Nature Communications*, 8(736):736, 2017.

[121] Mengjie Yu, Jae K. Jang, Yoshitomo Okawachi, Austin G. Griffith, Kevin Luke, Steven A. Miller, Xingchen Ji, Michal Lipson, and Alexander L. Gaeta. Breather soliton dynamics in microresonators. *Nature Communications*, 8 (736):736, 2017.

[122] Miro Erkintalo, Goëry Genty, Benjamin Wetzel, and John M. Dudley. Limitations of the linear raman gain approximation in modeling broadband nonlinear propagation in optical fibers. *Optics Express*, 18(24):25449–25460, 2010.

[123] Erwan Lucas, Hairun Guo, John D. Jost, Maxim Karpov, and Tobias J. Kippenberg. Detuning-dependent properties and dispersion-induced instabilities of temporal dissipative Kerr solitons in optical microresonators. *Physical Review A*, 95(4):043822, 2017.

[124] Alan Willner, Changyuan Yu, and Zhongqi Pan. *Optical Fiber Telecommunications VB (Fifth Edition): Chapter 7*. Academic Press, 2008.

[125] Mark G. Allen. Diode laser absorption sensors for gas-dynamic and combustion flows. *Measurement Science and Technology*, 9(4):545–562, 1998.

[126] Michael A. Choma, Marinko V. Sarunic, Changhuei Yang, and Joseph A. Izatt. Sensitivity advantage of swept source and fourier domain optical coherence tomography. *Optics Express*, 11(18):2183–2189, 2003.

[127] Pascal Del'Haye, Olivier Arcizet, Michael L. Gorodetsky, Ronald Holzwarth, and Tobias J. Kippenberg. Frequency comb assisted diode laser spectroscopy for measurement of microcavity dispersion. *Nature Photonics*, 3(9):529, 2009.

[128] Ian Coddington, Fabrizio R. Giorgetta, Esther Baumann, William C. Swann, and Nathan R. Newbury. Characterizing fast arbitrary cw waveforms with 1500 thz/s instantaneous chirps. *IEEE Journal of Selected Topics in Quantum Electronics*, 18(1):228–238, 2012.

[129] Long-Sheng Ma, Massimo Zucco, Susanne Picard, Lennart Robertsson, and Robert S. Windeler. A new method to determine the absolute mode number of a mode-locked femtosecond-laser comb used for absolute optical frequency measurements. *IEEE Journal of Selected Topics in Quantum Electronics*, 9 (4):1066–1071, 2003.

[130] J.-L. Peng, T.-A. Liu, and R.-H. Shu. Optical frequency counter based on two mode-locked fiber laser combs. *Applied Physics B*, 92(4):513–518, 2008.

[131] F. R. Giorgetta, I. Coddington, E. Baumann, W. C. Swann, and N. R. Newbury. Fast high-resolution spectroscopy of dynamic continuous-wave laser sources. *Nature Photonics*, 4(12):853–857, 2010.

[132] Qi-Fan Yang, Xu Yi, Ki Youl Yang, and Kerry Vahala. Spatial-mode-interaction-induced dispersive-waves and their active tuning in microresonators. *Optica*, 3:1132–1135, 2016.

[133] M. A. Tran, D. Huang, T. Komljenovic, J. Peters, and J. E. Bowers. A 2.5 kHz linewidth widely tunable laser with booster soa integrated on silicon. *Proceedings of the 2018 IEEE International Semiconductor Laser Conference, Santa Fe*, pages 1–2, 2018.

[134] Iouli E. Gordon, Laurence S. Rothman, Christian Hill, Roman V. Kochanov, Y Tan, Peter F. Bernath, Manfred Birk, V. Boudon, Alain Campargue, KV Chance, et al. The HITRAN2016 molecular spectroscopic database. *Journal of Quantitative Spectroscopy and Radiative Transfer*, 203:3–69, 2017.

[135] Erwan Lucas, Grigori Lihachev, Romain Bouchand, Nikolay G. Pavlov, Arslan S. Raja, Maxim Karpov, Michael L. Gorodetsky, and Tobias J. Kippenberg. Spatial multiplexing of soliton microcombs. *Nature Photonics*, 12: 699–705, 2018.

[136] Erin S. Lamb, David R. Carlson, Daniel D. Hickstein, Jordan R. Stone, Scott A. Diddams, and Scott B. Papp. Optical-frequency measurements with a Kerr microcomb and photonic-chip supercontinuum. *Physical Review Applied*, 9(2):024030, 2018.

[137] Brian Stern, Xingchen Ji, Yoshitomo Okawachi, Alexander L. Gaeta, and Michal Lipson. Battery-operated integrated frequency comb generator. *Nature*, 562(7727):401–405, 2018.

[138] Junqiu Liu, Arslan S. Raja, Maxim Karpov, Bahareh Ghadiani, Martin HP Pfeiffer, Botao Du, Nils J. Engelsen, Hairun Guo, Michael Zervas, and Tobias J. Kippenberg. Ultralow-power chip-based soliton microcombs for photonic integration. *Optica*, 5(10):1347–1353, 2018.

[139] Boqiang Shen, Lin Chang, Junqiu Liu, Heming Wang, Qi-Fan Yang, Chao Xiang, Rui Ning Wang, Jijun He, Tianyi Liu, Weiqiang Xie, et al. Integrated turnkey soliton microcombs. *Nature*, 582(7812):365–369, 2020.

[140] Daryl T. Spencer, Jared F. Bauters, Martijn J. R. Heck, and John E. Bowers. Integrated waveguide coupled Si_3N_4 resonators in the ultrahigh-Q regime. *Optica*, 1(3):153–157, 2014.

[141] Arslan S. Raja, Andrey S. Voloshin, Hairun Guo, Sofya E. Agafonova, Junqiu Liu, Alexander S. Gorodnitskiy, Maxim Karpov, Nikolay G. Pavlov, Erwan Lucas, Ramzil R. Galiev, et al. Electrically pumped photonic integrated soliton microcomb. *Nature Communications*, 10(1):680, 2019.

[142] Asad A. Abidi. CMOS microwave and millimeter-wave ICs: The historical background. In *2014 IEEE International Symposium on Radio-Frequency Integration Technology*, pages 1–5. IEEE, 2014.

[143] Junqiu Liu, Erwan Lucas, Arslan S. Raja, Jijun He, Johann Riemensberger, Rui Ning Wang, Maxim Karpov, Hairun Guo, Romain Bouchand, and Tobias J. Kippenberg. Photonic microwave generation in the X-and K-band using integrated soliton microcombs. *Nature Photonics*, 14(8):523–523, 2020.

[144] Duanni Huang, Minh A. Tran, Joel Guo, Jonathan Peters, Tin Komljenovic, Aditya Malik, Paul A. Morton, and John E. Bowers. High-power sub-kHz linewidth lasers fully integrated on silicon. *Optica*, 6(6):745–752, 2019.

[145] Tal Carmon, Lan Yang, and Kerry Vahala. Dynamical thermal behavior and thermal self-stability of microcavities. *Optics Express*, 12(20):4742–4750, 2004.

[146] W. Liang, V. S. Ilchenko, A. A. Savchenkov, A. B. Matsko, D. Seidel, and L. Maleki. Whispering-gallery-mode-resonator-based ultranarrow linewidth external-cavity semiconductor laser. *Optics Letters*, 35(16):2822–2824, 2010.

[147] W. Liang, D. Eliyahu, V. S. Ilchenko, A. A. Savchenkov, A. B. Matsko, D. Seidel, and L. Maleki. High spectral purity Kerr frequency comb radio frequency photonic oscillator. *Nature Communications*, 6:7957, 2015.

[148] N. G. Pavlov, S. Koptyaev, G. V. Lihachev, A. S. Voloshin, A. S. Gorodnitskiy, M. V. Ryabko, S. V. Polonsky, and M. L. Gorodetsky. Narrow-linewidth lasing and soliton Kerr microcombs with ordinary laser diodes. *Nature Photonics*, 12(11):694, 2018.

[149] N. M. Kondratiev, V. E. Lobanov, A. V. Cherenkov, A. S. Voloshin, N. G. Pavlov, S. Koptyaev, and M. L. Gorodetsky. Self-injection locking of a laser diode to a high-Q WGM microresonator. *Optics Express*, 25(23):28167–28178, 2017.

[150] Hualong Bao, Andrew Cooper, Maxwell Rowley, Luigi Di Lauro, Juan Sebastian Totero Gongora, Sai T. Chu, Brent E. Little, Gian-Luca Oppo, Roberto Morandotti, David J. Moss, et al. Laser cavity-soliton microcombs. *Nature Photonics*, 13(6):384, 2019.

[151] Bok Young Kim, Yoshitomo Okawachi, Jae K. Jang, Mengjie Yu, Xingchen Ji, Yun Zhao, Chaitanya Joshi, Michal Lipson, and Alexander L. Gaeta. Turnkey, high-efficiency Kerr comb source. *Optics Letters*, 44(18):4475–4478, 2019.

[152] Warren Jin, Qi-Fan Yang, Lin Chang, Boqiang Shen, Heming Wang, Mark A. Leal, Lue Wu, Maodong Gao, Avi Feshali, Mario Paniccia, et al. Hertz-linewidth semiconductor lasers using cmos-ready ultra-high-q microresonators. *Nature Photonics*, pages 1–8, 2021.

[153] Yu-Hung Lai, Myoung-Gyun Suh, Yu-Kun Lu, Boqiang Shen, Qi-Fan Yang, Heming Wang, Jiang Li, Seung Hoon Lee, Ki Youl Yang, and Kerry Vahala. Earth rotation measured by a chip-scale ring laser gyroscope. *Nature Photonics*, 14(6):345–349, 2020.

[154] Tengfei Hao, Jian Tang, David Domenech, Wei Li, Ninghua Zhu, José Capmany, and Ming Li. Toward monolithic integration of OEOs: From systems to chips. *Journal of Lightwave Technology*, 36(19):4565–4582, 2018.

[155] David Marpaung, Jianping Yao, and José Capmany. Integrated microwave photonics. *Nature Photonics*, 13(2):80–90, 2019.

[156] Kazuro Kikuchi. Fundamentals of coherent optical fiber communications. *Journal of Lightwave Technology*, 34(1):157–179, 2015.

[157] Samuel L. I. Olsson, Junho Cho, Sethumadhavan Chandrasekhar, Xi Chen, Peter J. Winzer, and Sergejs Makovejs. Probabilistically shaped PDM 4096-QAM transmission over up to 200 km of fiber using standard intradyne detection. *Optics Express*, 26(4):4522–4530, 2018.

[158] B. Dahmani, L. Hollberg, and R. Drullinger. Frequency stabilization of semiconductor lasers by resonant optical feedback. *Optics Letters*, 12(11): 876–878, 1987.

[159] L. Hollberg and M. Ohtsu. Modulatable narrow-linewidth semiconductor lasers. *Applied Physics Letters*, 53(11):944–946, 1988.

[160] A. Hemmerich, D. H. McIntyre, D. Schropp Jr, D. Meschede, and T. W. Hänsch. Optically stabilized narrow linewidth semiconductor laser for high resolution spectroscopy. *Optical Communications*, 75(2):118–122, 1990.

[161] H. Li and N. B. Abraham. Analysis of the noise spectra of a laser diode with optical feedback from a high-finesse resonator. *IEEE Journal of Quantum Electronics*, 25(8):1782–1793, 1989.

[162] Dag Roar Hjelme, Alan Rolf Mickelson, and Raymond G. Beausoleil. Semiconductor laser stabilization by external optical feedback. *IEEE Journal of Quantum Electronics*, 27(3):352–372, 1991.

[163] W. Liang, V. S. Ilchenko, D. Eliyahu, A. A. Savchenkov, A. B. Matsko, D. Seidel, and L. Maleki. Ultralow noise miniature external cavity semiconductor laser. *Nature Communications*, 6(1):1–6, 2015.

[164] Matthew W Puckett, Jiawei Wang, Debapam Bose, Grant M. Brodnik, Jianfeng Wu, Karl Nelson, and Daniel J. Blumenthal. Silicon nitride ring resonators with 0.123 dB/m loss and Q-factors of 216 million for nonlinear optical applications. In *Conference on Lasers and Electro-Optics Europe 2019*, page ce_11_3. OSA, 2019.

[165] Xingchen Ji, Felippe A. S. Barbosa, Samantha P. Roberts, Avik Dutt, Jaime Cardenas, Yoshitomo Okawachi, Alex Bryant, Alexander L. Gaeta, and Michal Lipson. Ultra-low-loss on-chip resonators with sub-milliwatt parametric oscillation threshold. *Optica*, 4(6):619–624, 2017.

[166] Junqiu Liu, Guanhao Huang, Rui Ning Wang, Jijun He, Arslan S. Raja, Tianyi Liu, Nils J. Engelsen, and Tobias J. Kippenberg. High-yield, wafer-scale fabrication of ultralow-loss, dispersion-engineered silicon nitride photonic circuits. *Nature Communications*, 12(1):1–9, 2021.

[167] Zhichao Ye, Krishna Twayana, Peter A. Andrekson, and Victor Torres-Company. High-Q Si_3N_4 microresonators based on a subtractive processing for Kerr nonlinear optics. *Optics Express*, 27(24):35719–35727, 2019.

[168] Qing Li, Ali A. Eftekhar, Majid Sodagar, Zhixuan Xia, Amir H. Atabaki, and Ali Adibi. Vertical integration of high-Q silicon nitride microresonators into silicon-on-insulator platform. *Optics Express*, 21(15):18236–18248, 2013.

[169] Aleksandr Biberman, Michael J. Shaw, Erman Timurdogan, Jeremy B. Wright, and Michael R. Watts. Ultralow-loss silicon ring resonators. *Optics Letters*, 37(20):4236–4238, 2012.

[170] Mian Zhang, Cheng Wang, Rebecca Cheng, Amirhassan Shams-Ansari, and Marko Lončar. Monolithic ultra-high-Q lithium niobate microring resonator. *Optica*, 4(12):1536–1537, 2017.

[171] R. Adar, M. R. Serbin, and Victor Mizrahi. Less than 1 dB per meter propagation loss of silica waveguides measured using a ring resonator. *Journal of Lightwave Technology*, 12(8):1369–1372, 1994.

[172] Youwen Fan, Albert van Rees, Peter J. M. Van der Slot, Jesse Mak, Ruud M. Oldenbeuving, Marcel Hoekman, Dimitri Geskus, Chris G. H. Roeloffzen, and Klaus-J. Boller. Hybrid integrated InP-Si_3N_4 diode laser with a 40-Hz intrinsic linewidth. *Optics Express*, 28(15):21713–21728, 2020.

[173] Minh A. Tran, Duanni Huang, and John E. Bowers. Tutorial on narrow linewidth tunable semiconductor lasers using Si/III-V heterogeneous integration. *APL Photonics*, 4(11):111101, 2019.

[174] Chao Xiang, Warren Jin, Joel Guo, Jonathan D. Peters, M. J. Kennedy, Jennifer Selvidge, Paul A.. Morton, and John E. Bowers. Narrow-linewidth III-V/Si/Si_3N_4 laser using multilayer heterogeneous integration. *Optica*, 7 (1):20–21, 2020.

[175] Jared F. Bauters, Martijn JR Heck, Demis D. John, Jonathon S. Barton, Christiaan M. Bruinink, Arne Leinse, René G. Heideman, Daniel J. Blumenthal, and John E. Bowers. Planar waveguides with less than 0.1 dB/m propagation loss fabricated with wafer bonding. *Optics Express*, 19(24):24090–24101, 2011.

[176] T. J. Kippenberg, S. M. Spillane, and K. J. Vahala. Modal coupling in traveling-wave resonators. *Optics Letters*, 27(19):1669–1671, Oct 2002. doi: 10.1364/OL.27.001669.

[177] Anatoliy Savchenkov, Skip Williams, and Andrey Matsko. On stiffness of optical self-injection locking. *Photonics*, 5(4):43, 2018.

[178] Heming Wang, Lue Wu, Zhiquan Yuan, and Kerry Vahala. Towards millihertz laser frequency noise on a chip. *arXiv preprint arXiv:2010.09248*, 2020.

[179] N. M. Kondratiev and M. L. Gorodetsky. Thermorefractive noise in whispering gallery mode microresonators: Analytical results and numerical simulation. *Physics Letters A*, 382(33):2265–2268, 2018.

[180] Guanhao Huang, Erwan Lucas, Junqiu Liu, Arslan S. Raja, Grigory Lihachev, Michael L. Gorodetsky, Nils J. Engelsen, and Tobias J. Kippenberg. Thermorefractive noise in silicon-nitride microresonators. *Physical Review A*, 99 (6):061801, 2019.

[181] Jinkang Lim, Anatoliy A. Savchenkov, Elijah Dale, Wei Liang, Danny Eliyahu, Vladimir Ilchenko, Andrey B. Matsko, Lute Maleki, and Chee Wei Wong. Chasing the thermodynamical noise limit in whispering-gallery-mode resonators for ultrastable laser frequency stabilization. *Nature Communications*, 8(1):1–7, 2017.

[182] Pei-Hsun Wang, Yi Xuan, Li Fan, Leo Tom Varghese, Jian Wang, Yang Liu, Xiaoxiao Xue, Daniel E Leaird, Minghao Qi, and Andrew M. Weiner. Drop-port study of microresonator frequency combs: Power transfer, spectra and time-domain characterization. *Optics Express*, 21(19):22441–22452, 2013.

[183] Kerry J. Vahala. Optical microcavities. *Nature*, 424(6950):839, 2003.

[184] Wei Liang, Anatoliy A. Savchenkov, Vladimir S. Ilchenko, Danny Eliyahu, David Seidel, Andrey B. Matsko, and Lute Maleki. Generation of a coherent near-infrared Kerr frequency comb in a monolithic microresonator with normal GVD. *Optics Letters*, 39(10):2920–2923, 2014.

[185] V. E. Lobanov, G. Lihachev, T. J. Kippenberg, and M. L. Gorodetsky. Frequency combs and platicons in optical microresonators with normal GVD. *Optics Express*, 23(6):7713–7721, 2015.

[186] Grigory V. Lihachev, Junqiu Liu, Lin Chang, Jijun He, Rui Ning Wang, Joel Guo, Arslan S. Raja, Erwan Lucas, Nikolay G. Pavlov, John D. Jost, Dave Kinghorn, John E. Bowers, and Tobias J. Kippenberg. Laser self-injection locked frequency combs in a normal GVD integrated microresonator. In *Conference on Lasers and Electro-Optics 2020*, pages STh1O–3. Optical Society of America, 2020.

[187] Nikita M. Kondratiev and Valery E. Lobanov. Modulational instability and frequency combs in whispering-gallery-mode microresonators with backscattering. *Physical Review A*, 101(1):013816, 2020.

[188] Nikita M. Kondratiev, Andrey S. Voloshin, Valery E. Lobanov, and Igor A. Bilenko. Numerical modelling of WGM microresonator Kerr frequency combs in self-injection locking regime. In *Nonlinear Optics and its Applications 2020*, volume 11358, page 113580O. International Society for Optics and Photonics, 2020.

[189] Attila Fülöp, Mikael Mazur, Abel Lorences-Riesgo, Óskar B. Helgason, Pei-Hsun Wang, Yi Xuan, Dan E. Leaird, Minghao Qi, Peter A. Andrekson, Andrew M. Weiner, et al. High-order coherent communications using mode-locked dark-pulse Kerr combs from microresonators. *Nature Communications*, 9(1):1–8, 2018.

[190] M. C. Larson, A. Bhardwaj, W. Xiong, Y. Feng, X. D. Huang, K. P. Petrov, M. Moewe, H. Y. Ji, A. Semakov, C. W. Lv, et al. Narrow linewidth sampled-grating distributed Bragg reflector laser with enhanced side-mode suppression. In *Optical Fiber Communication Conference 2015*, pages 1–3. IEEE, 2015.

[191] Tin Komljenovic, Michael Davenport, Jared Hulme, Alan Y. Liu, Christos T. Santis, Alexander Spott, Sudharsanan Srinivasan, Eric J. Stanton, Chong Zhang, and John E. Bowers. Heterogeneous silicon photonic integrated circuits. *Journal of Lightwave Technology*, 34(1):20–35, 2016.

[192] Bill Corcoran, Mengxi Tan, Xingyuan Xu, Andreas Boes, Jiayang Wu, Thach G. Nguyen, Sai T. Chu, Brent E. Little, Roberto Morandotti, Arnan Mitchell, et al. Ultra-dense optical data transmission over standard fibre with a single chip source. *Nature Communications*, 11(1):1–7, 2020.

[193] Sébastien Tanzilli, Anthony Martin, Florian Kaiser, Marc P. De Micheli, Olivier Alibart, and Daniel B. Ostrowsky. On the genesis and evolution of integrated quantum optics. *Laser & Photonics Review*, 6(1):115–143, 2012.

[194] Hansuek Lee, Myoung-Gyun Suh, Tong Chen, Jiang Li, Scott A. Diddams, and Kerry J. Vahala. Spiral resonators for on-chip laser frequency stabilization. *Nature Communications*, 4:2468, 2013.